

---

# Analyzation of radiation resistance of carbon-based materials for accelerator components

---

Zur Erlangung des Grades eines Doktors der Naturwissenschaften  
(Dr. rer. nat.)

genehmigte Dissertation von **M.Sc. Philipp Bolz** aus Flörsheim

Erstgutachterin: Prof. Dr. Christina Trautmann

Zweitgutachter: Prof. Dr. Gerhard Wilde

März 22 – Darmstadt – D17



TECHNISCHE  
UNIVERSITÄT  
DARMSTADT

Fachbereich Material- und Geowissenschaften

Ionenstrahlmodifizierte Materialien



---

Analyzation of radiation resistance of carbon-based materials for accelerator components

Darmstadt, Technische Universität Darmstadt

Jahr der Veröffentlichung der Dissertation auf TUprints: 2023

Genehmigte Dissertation von M.Sc. Philipp Bolz aus Flörsheim

1. Gutachten: Prof. Dr. Christina Trautmann

2. Gutachten: Prof. Dr. Gerhard Wilde

Tag der Einreichung: 22.03.2022

Tag der Prüfung: 19.07.2022

Darmstadt 2022 – D 17

Bitte zitieren Sie dieses Dokument als:

URN: urn:nbn:de:tuda-tuprints-231136

URI: <https://tuprints.ulb.tu-darmstadt.de/id/eprint/23113>

Dieses Dokument wird bereitgestellt von tuprints,

E-Publishing-Service der TU Darmstadt

<http://tuprints.ulb.tu-darmstadt.de>

[tuprints@ulb.tu-darmstadt.de](mailto:tuprints@ulb.tu-darmstadt.de)

Veröffentlicht unter CC BY-SA 4.0 International

---

# Erklärung zur Dissertation

Hiermit versichere ich, die vorliegende Dissertation ohne Hilfe Dritter nur mit den angegebenen Quellen und Hilfsmitteln angefertigt zu haben. Alle Stellen, die aus Quellen entnommen wurden, sind als solche kenntlich gemacht. Diese Arbeit hat in gleicher oder ähnlicher Form noch keiner Prüfungsbehörde vorgelegen.

Darmstadt, 22. März 2022

(Philipp Bolz)

---

# Abstrakt

Funktionale Materialien, die hohen Strahlungsdosen ausgesetzt werden, müssen gegen extreme Bedingungen resistent sein. Faktoren, die ihre Strahlungshärte limitieren, sind allerdings wenig erforscht. Beispiele sind Materialien, die in Teilchenbeschleunigern als Strahlblocker, Target oder Kollimator eingesetzt werden. Durch die steigende Energie und Pulsintensität zukünftiger Beschleunigeranlagen werden diese Bauteile Belastungen mit sehr hohen Dehnungsraten ausgesetzt. Um die sichere Operation von zukünftigen Anlagen zu gewährleisten, muss die Eignung von Materialien in extremen gepulsten Bedingungen getestet werden.

In dieser Arbeit werden hauptsächlich die graphitischen Materialien isotroper Graphit, kohlenstofffaserverstärkter Kohlenstoff, hochorientierter pyrolytischer Graphit und flexibler Graphit untersucht. Die mechanischen Eigenschaften und Materialveränderungen mit steigender Ionenfluenz wurden mit Nano- und Mikroindentation sowie Nanoimpaktmessungen untersucht. Die Proben wurden am UNILAC (Universal Linear Accelerator) des GSI Helmholtzzentrum für Schwerionenforschung bestrahlt. Verschiedene Arten von Ionen mit MeV bis GeV Energien wurden verwendet und Fluenzen bis zu  $2 \times 10^{14}$  Ionen/cm<sup>2</sup> erreicht. Isotroper Graphit und kohlenstofffaserverstärktem Kohlenstoff weisen große Veränderungen des Elastizitätsmoduls um 300 % und der Härte um 1000 % im Vergleich zur unbestrahlten Probe auf. Diese ausgeprägten Materialmodifikationen treten bei Bestrahlung mit Ionen mit Energieverlusten über 18 keV/nm auf. Nanoimpaktmessungen zeigen eine Erhärtung des Materials, die zu Versprödung bei Fluenzen über  $3 \times 10^{13}$  Ionen/cm<sup>2</sup> führt. Ramanspektroskopie zeigt, dass diese starken Veränderungen der mechanischen Eigenschaften durch eine allotropische Transformation der Graphitstruktur in eine fehlgeordnete Struktur, die glasartigem Kohlenstoff ähnelt, verursacht wird.

Um weitere Informationen über die dynamische Materialreaktion, verursacht durch Ionenpulse, zu bekommen, werden Messungen während der Bestrahlung benötigt. Dafür wurden scheibenförmige Proben kurzen Uranionenpulsen mit einer Leistungsdichte von  $\sim 3$  MW/cm<sup>3</sup> ausgesetzt. Die resultierende thermische Spannung

---

produziert Druckwellen in den Proben. Die resultierende Geschwindigkeit dieser Bewegung kann an der Probenoberfläche mittels eines Laser-Doppler-Vibrometers gemessen werden. Das Geschwindigkeitssignal offenbart die Biegemoden der Proben als dominante Komponenten. Mit steigendem Strahlungsschaden verschiebt sich die Frequenz der Biegemoden zu höheren Werten. Durch diese Verschiebung und mittels Vergleiches mit ANSYS Simulationen kann das Elastizitätsmodul von isotropem Graphit und kohlenstofffaserverstärktem Kohlenstoff bestimmt werden. Der Vergleich mit den Elastizitätsmodulen, die durch Mikroindentation erhalten wurden, zeigt eine gute Übereinstimmung, was die Aussagekraft der Methode bestätigt. Stresswellen verursacht durch die Bestrahlung bleiben im elastischen Bereich und keine großräumigen Defekte werden in Graphit beobachtet. Wolfram und Kupfer zeigen keine strahlungsbedingten Veränderungen. Glasartiger Kohlenstoff und hexagonales Bornitrid dagegen haben eine geringe Strahlenresistenz, was durch Abplatzen und Rissbildung verdeutlicht wird. Materialversagen wird beim Einsatz dieser Materialien in Hochdosisumgebungen riskiert.

## Abstract

Functional materials in high-dose environments have to withstand extreme radiation conditions but factors that limit their radiation hardness are poorly understood. An example are materials for components in particle accelerators such as beam dumps, targets and collimators. With increasing energy and pulse intensities of new accelerator facilities, these beam intercepting devices are exposed to loads with high strain rates. To secure the safe operation of future facilities, the suitability of materials exposed to extreme pulsed beam conditions need to be tested.

This work mainly concentrates on graphitic materials including isotropic graphite, carbon fibre reinforced carbon, highly oriented pyrolytic graphite and flexible graphite. The mechanical properties and material changes with increasing ion fluence are investigated using nano- and microindentation and nanoimpact measurements. Samples are irradiated at the universal linear accelerator UNILAC of the GSI Helmholtz Centre for Heavy Ion Research. The experiments are performed with various types of

---

ions of MeV to GeV energies achieving fluences up to  $2 \times 10^{14}$  ions/cm<sup>2</sup>. In isotropic graphite and carbon fibre reinforced carbon, large changes in Young's modulus of up to 300 % and in hardness by more than 1000 % compared to the pristine values are observed. These pronounced material modifications occur if the energy loss of the ions surpasses approximately 18 keV/nm. By nanoimpact measurements hardening is revealed, leading to embrittlement at fluences above  $3 \times 10^{13}$  ions/cm<sup>2</sup>. Raman spectroscopy indicates that these severe changes of mechanical properties are related to beam-induced allotropic transformation of the graphite structure into a disordered structure similar to glassy carbon.

To obtain further information about the dynamic response of the materials to ion impacts, in-situ measurements during the irradiation are required. Disc-shaped samples are exposed to short pulses of uranium ions corresponding to a deposited power density of  $\sim 3$  MW/cm<sup>3</sup>. The resulting thermal stress produces pressure waves in the samples. The velocity of the respective motion of the target surface is monitored by laser Doppler vibrometry. The velocity signal recorded as a function of time reveals bending modes as the dominant components. With accumulated radiation damage, the bending mode frequency shifts toward higher values. Based on this shift, the Young's modulus of irradiated isotropic graphite and carbon fibre reinforced carbon are determined by comparison with FEM simulations. Young's modulus values deduced from microindentation measurements are similar confirming the validity of the method. Beam-induced stress waves remain in the elastic regime and no large-scale damage effects are observed in graphite. Tungsten and copper show no beam-induced changes while glassy carbon and hexagonal boron nitride have lower radiation resistance evident by chipping and cracks risking material failure when applied in high dose environment.

---

# Table of content

1	Introduction and motivation	1
2	Theoretical background	4
2.1	Graphite	4
2.1.1	Isotropic graphite	5
2.1.2	Carbon fibre reinforced carbon	6
2.1.3	Glassy carbon	7
2.1.4	Well-oriented graphite	8
2.2	Other materials	9
2.2.1	Tungsten	10
2.2.2	Copper	11
2.2.3	Hexagonal boron nitride	11
2.3	Ion matter interaction	12
2.4	Irradiation damage in graphite	14
3	Experimental	16
3.1	Sample preparation	16
3.2	Ion beam irradiation	16
3.3	Post irradiation characterization	21
3.3.1	Raman spectroscopy	21
3.3.2	Micro- and nanoindentation	26
3.3.3	Nanoimpact	30
3.3.4	Multiple impulse	34
3.4	In situ measurements	35
3.4.1	Measurement of beam-induced vibrations and stress waves by laser Doppler vibrometry	35
3.4.2	Numerical calculation of bending and stress wave frequencies of a circular disc	38
3.4.3	Analyzation of the velocity signal	40
3.4.4	Finite element method simulations of ion beam impacted discs	43
4	Post-irradiation analysis of structural and mechanical properties	45
4.1	Beam-induced structural modifications studied by Raman spectroscopy	45

---

4.2	Beam-induced changes of quasi-static mechanical properties	49
4.2.1	Pristine materials	50
4.2.2	Isotropic polycrystalline graphite	51
4.2.3	Carbon fibre reinforced carbon	55
4.2.4	Well-oriented graphite	60
4.2.5	Material comparison	62
4.2.6	Estimation of damage cross section	63
4.3	Investigation of dynamic mechanic properties of graphite by nanoimpact measurements	65
4.3.1	Influence of impact parameters on pristine samples	66
4.3.2	Beam-induced changes of dynamic properties of isotropic polycrystalline graphite	73
4.3.3	Beam-induced changes of dynamic properties of carbon fibre reinforced carbon	76
4.4	Observation of fatigue failure by multiple impact measurements	77
5	Online monitoring of beam-induced bending and stress waves	83
5.1	Temperature development during U ion beam impacts	83
5.2	Metals	85
5.3	Isotropic polycrystalline graphite	88
5.4	Carbon fibre reinforced carbon	92
5.5	Flexible graphite	96
5.6	Glassy carbon	98
5.7	Hexagonal boron nitride	100
6	Conclusions	104
7	References	108
	List of figures	122
	List of tables	134
	List of abbreviations	135
	Acknowledgements	137



---

# 1 Introduction and motivation

---

With a new generation of particle accelerators such as the Facility for Antiproton and Ion Research (FAIR) or the High-Luminosity Large Hadron Collider (HL-LHC) at the European Organization for Nuclear Research (CERN), unprecedented high beam intensities will be reached. For safe operation of these accelerators, materials capable to withstand extreme conditions induced by the high beam intensities need to be provided. Graphite is a natural choice because its low density means low stopping power. Due to its high thermal conductivity, combined with its low coefficient of thermal expansion and its high service temperature, graphite possesses high mechanical stability to beam-induced heating. Furthermore, the low atomic number of carbon results in a low activation and a quick decay of generated radioactive isotopes. Graphitic materials are used in high-energy accelerator applications mainly for beam intercepting devices such as production targets [1,2], collimators [3] or beam dumps as well as in nuclear reactors acting as structural materials and as moderator.

Graphite is characterized by a very high radiation hardness as its simple structure allows a quick recombination of generated defects. Nevertheless, it has been shown that irradiation of graphite results in structural defects or phase transformations leading to a change of mechanical, electrical and thermal properties [4–7]. Swelling, embrittlement and stress waves due to pulsed beam conditions can result in failure of the components. To provide safe operation conditions, it is necessary to investigate beam-induced property changes of the mechanical properties, especially under dynamic conditions.

In this work, several types of graphite are investigated. Isotropic polycrystalline graphite (PG) is used in many nuclear applications due to its simple production process and the easy machining. Several grades with different grain sizes are investigated to observe the influence of the microstructure. Carbon fibre reinforced carbon (CFC) has a similar matrix structure as PG, but additional carbon fibres improve the thermal and mechanical properties. CFC is currently utilized in primary and secondary collimators at CERN. Furthermore, flexible graphite (FG) and highly oriented pyrolytic graphite (HOPG) are investigated. Their well-oriented planes act as a model material for

---

graphite without the influence of grain boundaries. Glassy carbon (GC) is used as model material, for disordered graphite similar to the structure obtained after heavy ion irradiation up to very high doses [6,8].

Experiments at the GSI Helmholtz Centre for Heavy Ion Research allow irradiation with ions in the MeV-GeV energy range. In contrast to ion irradiation in the keV-MeV energy range achieved at smaller accelerators, most of the projectile energy is not directly transferred by elastic collisions with target atoms, but by electronic excitation and ionization processes. To achieve maximum energy losses and thus the largest changes, the experiments are conducted at the linear accelerator UNILAC, which provides ions of energies close to the Bragg peak [9,10]. The ion penetration at these energies is in the range of 10 to 100  $\mu\text{m}$ . Analysis techniques hence have to be sensitive to the surface of the investigated samples. For the investigation of structural changes in graphite Raman spectroscopy is used. Defects in the graphite structure activate the 'D band' allowing the determination of the defect concentration of the investigated material [11,12]. For the determination of mechanical properties of thin layers, nano- and microindentation is the method of choice. Important material parameters like the Young's modulus are obtained [13,14]. The ion beam-induced change of these material parameters can be applied to calculations and simulations during the design of beam intercepting devices. Nanoimpact measurements determine dynamical mechanical material parameters like the dynamic hardness or the fatigue failure probability during repeated impacts [15]. Finally, in situ measurements during ion beam irradiation are used to determine bending and stress waves. Comparison with FEM simulations allows the determination of beam-induced changes of mechanical properties. Crack formation can be observed during the measurements which could be used as indicator of material failure for early detection and avoidance of failures of beam intercepting devices in accelerators.

This work is divided in five parts. Chapter 2 summarizes essential information about the materials investigated and swift heavy ion beam interactions with matter in general and with graphite, specifically. Chapter 3 introduces the theoretical concepts of the applied methods and provides information about the specific devices and measurement parameters. Furthermore, the used ion beam parameters are described. Chapter 4 summarizes the results obtained during post-irradiation analysis. The results

---

of in-situ measurements are presented in chapter 5. Finally, a short conclusion and outlook is provided in chapter 6.

---

## 2 Theoretical background

---

This chapter shortly summarizes the background relevant to this work. Section 2.1 introduces graphite and the graphitic materials investigated. Important material parameters used for calculations and simulations in the result chapters are listed. Other materials investigated in this work are introduced in section 2.2. In section 2.3 fundamentals of ion matter interactions are presented. Section 2.4 summarizes the current knowledge about irradiation damage in graphite.

---

### 2.1 Graphite

---

Graphite consists of  $sp^2$  hybridized carbon atoms. For each carbon atom the  $sp^2$  hybrids form covalent bonds to 3 other carbon atoms. These  $\sigma$ -bonds have a length of 1.42 Å and are 120° apart from each other forming a honeycomb lattice (Figure 2.1).

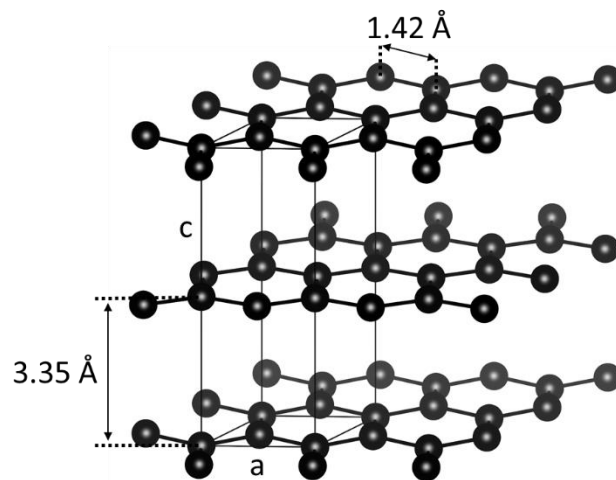


Figure 2.1: Structure of graphite with the marked unit cell and characteristic atomic distances, created with VESTA software [16].

The  $\pi$ -bonds connect graphite layers by weak van der Waals bonds. The layers are stacked in hexagonal order with an interlayer distance of 3.35 Å. Ideal graphite has a density of 2.267 g/cm<sup>3</sup>. This structure results in highly anisotropic properties. While the  $\sigma$ -bonds within the basal planes are very stable, the basal planes can easily slide past

---

each other or be separated. Similarly, the electronic conductivity is about 1000 times higher within the planes compared to perpendicular to the planes.

The properties of graphitic materials heavily depend on the precursor materials and heat treatment used in the production process. During carbonization, organic precursors are heated to temperatures of 1000 to 1500 °C. Non-carbon atoms like hydrogen and oxygen are released yielding pure carbon that forms hexagonal rings. Depending on the precursor material, the nanotexture is either oriented or random. During graphitization, in a second heat treatment at temperatures between 2500 and 3000 °C, large graphitic structures can grow in oriented precursor materials. In random oriented precursor materials, graphitisation is inhibited at temperatures as high as 3000 °C. Instead, non-six-membered rings remain in the structure resulting in curved planes.

The main focus of this work lies on isotropic polycrystalline graphite, a material commonly used in nuclear and high dose environments. It contains randomly oriented grains of some micrometres in diameter. Also, carbon fibre reinforced carbon is investigated which contains additional fibres to improve the mechanical and thermal properties. As model systems for ideal graphite, flexible graphite and highly oriented pyrolytic graphite is used due to larger planes with known orientation, whereas glassy carbon produced from randomly oriented nanotextures serves as a model material for completely disordered graphite.

---

### **2.1.1 Isotropic graphite**

---

Isotropic graphite is produced by milling, e.g., a coal or pitch coke-based filler material to the desired grain size. Afterwards the milled particles are typically mixed with a binder pitch and are formed by isostatic pressing. They are carbonized at a temperature of approximately 1000 °C, optional with additional pitch impregnation steps. Finally, the blocks are heated to 2500-3000 °C for graphitization [17]. Cooling down after the final heating process results in the generation of micro-cracks and pores. The porosity of the final material is about 10 %. In this work three different isotropic graphite grades are investigated: (1) SGL R6300 [18] and (2) R6650 [19] with a respective average grain size of 20 and 7 µm and produced using a binder phase

and (3) POCO ZEE [20] with a smaller grain size of only 1  $\mu\text{m}$  and produced without using a binder. A summary of the material properties is listed in Table 2.1.

Table 2.1: Properties of the investigated isotropic polycrystalline graphite grades SGL R6300 and SGL R6650 and POCO ZEE according to the producers' data sheets.

	SGL R6300 [18]	SGL R6650 [19]	POCO ZEE [20]
Average grain size [ $\mu\text{m}$ ]	20	7	1
Density [ $\text{g}/\text{cm}^3$ ]	1.73	1.84	1.78
Young's modulus [GPa]	10	12.5	14.5
Poisson's ratio	0.28	0.19	0.30
Coefficient of thermal expansion [ $10^{-6}/\text{K}$ ]	2.7	4.1	8.1
Thermal conductivity [ $\text{W}/\text{m}\cdot\text{K}$ ]	70	95	70
Specific heat [ $\text{J}/\text{g}\cdot\text{K}$ ]	0.7	0.7	0.7

### 2.1.2 Carbon fibre reinforced carbon

Carbon fibre reinforced carbon (CFC) composites provide improved mechanical and thermal properties of isotropic graphite by addition of highly oriented carbon fibres. During the first production step, carbon fibres are placed in the desired shape within a carbonaceous matrix to form a skeleton. Afterwards the structure is densified by alternating impregnation and carbonisation steps until a desired density is reached. The composite is finally graphitized at temperatures between 1500 and 2750  $^{\circ}\text{C}$  [21]. In this work the two-dimensional CFC grades SGL Premium [22], SGL Experimental Premium [23] and Tatsuno AC150K [24] are studied. Two different orientations are investigated with the fibre planes either parallel to the sample surface named in-plane orientation or normal to the sample surface named transversal orientation. A scheme of the CFC fibre planes with the two orientations is shown in Figure 2.2

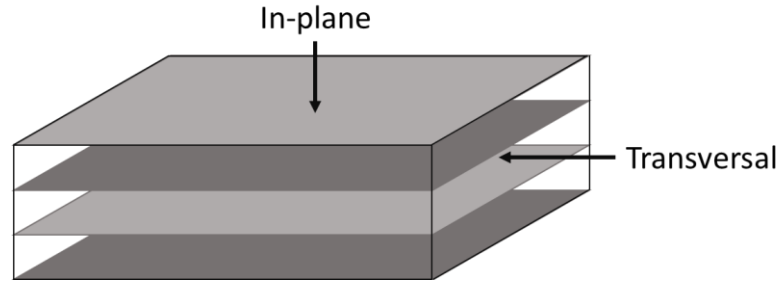


Figure 2.2: Scheme of fibre planes in CFC with marked directions of the surface of samples with in-plane and transversal orientation.

SGL Premium and Experimental Premium are based on a woven fibre structure. The production process is the same except that an additional heating process is applied for Experimental Premium. AC150K has more distributed fibres in the graphite matrix. The properties are summarized in Table 2.2.

Table 2.2: Properties of the investigated carbon fibre reinforced carbon grades SGL Premium, SGL Experimental Premium and Tatsuno AC150k according to the producers' data sheets. Due to the two-dimensional structure of the fibre planes, the properties are given for the directions parallel and normal to the fibre planes.

	Premium [22]		Experimental [23]		AC150k [24]	
	Parallel	Normal	Parallel	Normal	Parallel	Normal
Density [g/cm <sup>3</sup> ]	1.6		1.77		1.65	
Flexural strength [MPa]	230	-	200	-	106-155	10
Thermal conductivity [W/m·K]	40 [25]	5 [25]	195	30	220	55
Coefficient of thermal expansion [10 <sup>-6</sup> /K]	0	7.5	0.7	12	-1.3	9-10

### 2.1.3 Glassy carbon

Glassy carbon (GC) is produced from carbon-based polymers which do not graphitize at high temperatures [26]. With increasing temperature during the heat treatment the

stacking order of carbon layers increases, but even at temperatures near the sublimation point the structure remains turbostratic [17]. The curvature in the graphene planes and hence the inability to graphitize is caused by five and seven-membered rings [27–29]. This results in a fullerene like structure which cannot be transformed into graphite even at temperatures as high as 3000 °C.

The grades Sigradur K and G [30] are investigated. They are produced from phenolic resins by pyrolysis up to 1000 °C and 2800 °C for Sigradur K and G, respectively. According to the transmission electron microscopy investigation by Harris [29], Sigradur K has single carbon layers enclosing pores with diameters in the order of 1 nm. For Sigradur G the higher temperature during the production process leads to lamella with a thickness of 2 to 4 graphene layers enclosing pores of ~5 nm.

Table 2.3: Material properties of the glassy carbon grades Sigradur K and G according to the producers' data sheets.

	Sigradur K [30]	Sigradur G [30]
Density [g/cm <sup>3</sup> ]	1.54	1.42
Young's modulus [GPa]	35	35
Poisson's ratio	0.17 [31]	0.155 [31]
Coefficient of thermal expansion [10 <sup>-6</sup> /K]	3.5	2.6
Thermal conductivity [W/m·K]	4.6	6.3
Specific heat [J/g·K]	0.74 [25]	0.72 [25]

#### 2.1.4 Well-oriented graphite

In this work two kinds of well-oriented graphite are investigated. Pyrolytic graphite is produced by heat treatment of pyrolytic carbon or by chemical vapour deposition at temperatures above 2500 °C. Additional hot working with an applied compressive stress at temperatures above 3000 °C produces highly oriented pyrolytic graphite (HOPG) [32] with crystallite sizes of up to 10 µm. An angular spread of both the a- and

the c-axis of the graphite crystallites of less than 1° can be achieved. HOPG is used as substrate or as calibration material in scanning tunnelling microscopy. However, its brittleness and difficult machinability prohibit its use in applications with mechanical requirements.

Flexible graphite (FG) [33,34] is produced by mixing natural graphite flakes with a highly oxidizing acid to form graphite intercalation compounds. These are expanded by a sudden application of high temperature, followed by a rolling process generating mechanical connections between the sheets. The rolled expanded graphite particles finally form a continuous strip, without the addition of a binder. FG is well-oriented along the c-axis while the disorientation of the a-axis is much larger compared to HOPG. While still containing the high anisotropy of graphite it can also be easily formed and is hence used in thermal management applications.

Table 2.4: Material properties of the HOPG grade ZYB produced by Momentive and NT-MDT and the flexible graphite grade SIGRAFLEX produced by SGL.

	HOPG [32]		FG [33,34]	
	In-plane	Through plane	In-plane	Through plane
Density [g/cm <sup>3</sup> ]	2.26		1.0	
Young's modulus [GPa]	-	-	0.7	
Coefficient of thermal expansion [10 <sup>-6</sup> /K]	Slightly negative	20	~1	~50
Thermal conductivity [W/m·K]	1600-2000	~8	220	5
Specific heat [J/g·K]	-		0.7	

## 2.2 Other materials

In addition to graphite tungsten, copper and hexagonal boron nitride are investigated. While not the main focus of this work, these materials also have relevance in

accelerator environments due to their use in targets, accelerator components or beam dumps. Their most important properties are summarized in Table 2.5.

Table 2.5: Material properties of tungsten, copper and h-BN .

	Tungsten	Copper	h-BN [35]
Density [g/cm <sup>3</sup> ]	19.3	8.92	2
Young's modulus [GPa]	411	120	23
Poisson's ratio	0.28	0.35	0.22
Coefficient of thermal expansion [10 <sup>-6</sup> /K]	4.5	17	3
Thermal conductivity [W/m·K]	173	401	25
Specific heat [J/g·K]	0.13	0.39	0.6

### 2.2.1 Tungsten

Tungsten is a brittle metal with a very high hardness causing it to be very difficult to machine. In its most stable form, it has a body centred cubic structure with a lattice constant of 3.16 Å at room temperature. Tungsten has a very high density and the highest melting (3422°C) and boiling (5930°C) point of all pure metals. Its main industrial application is as tungsten carbide in cemented carbide tools. Pure tungsten is used in high temperature applications like the filaments of light bulbs or vacuum tubes or as heating elements. The high melting point combined with its high stability at high temperature makes tungsten interesting as shielding material in radiation environments. Tungsten is the main material in tertiary collimators at CERN to absorb beam showers or protect magnets [36]. Furthermore, it is used in targets such as the antiproton decelerator target [37] at CERN or as spallation target of the European spallation source [9,38].

---

## 2.2.2 Copper

---

Copper is a relatively soft metal which can be easily formed and worked. It has a face centred cubic structure with a lattice constant of 3.62 Å. Copper has one of the highest electrical and thermal conductivities of all metals and a melting point of 1083 °C. Most applications employ its high conductivities. It is used as conductor in wires, integrated circuits, heat sinks and heat exchangers. Many accelerator components like cavities or resonators are plated with copper. At the GSI facility an approximately 200 µm thick copper layer is deposited to improve the electrical conductivity and hence reduce energy losses within the cavities. At CERN copper is also employed in tertiary collimators [39]. The high thermal conductivity allows a rapid dissipation of the heat induced by ion impacts preventing melting of the beam-exposed components.

---

## 2.2.3 Hexagonal boron nitride

---

Boron nitride (BN) exists in three allotropes that can directly be compared to carbon allotropes. At room temperature the cubic  $\beta$ -BN is stable and has the same structure as diamond. The hexagonal  $\alpha$ -BN is stable above 1200 °C until the melting point of 2967 °C. Like graphite it has a planar hexagonal honeycomb structure. The wurtzite  $\gamma$ -BN is stable at pressures above 10 GPa and has the same structure as the hexagonal diamond lonsdaleite. Both  $\alpha$ -BN and  $\gamma$ -BN are metastable at room temperature. Due to its similar structure to graphite and almost identical densities and high melting points,  $\alpha$ -BN is included as material to be investigated in this work. However, due to the polar binding between the boron and the nitrogen atoms,  $\alpha$ -BN has properties that are typically ascribed to ceramics. At room temperature the electrons are constrained and  $\alpha$ -BN is an insulator. In accelerators,  $\alpha$ -BN is considered as candidate material for beam dumps [40] and luminescence screens. In this work, the isotropic grade HeBoSint D100 [35] produced by Henze Boron Nitride Products is investigated. As for the PG grades, grains with well-oriented planes are randomly connected leading to isotropic properties of boron nitride as listed in Table 2.5. Most h-BN properties are similar to PG; however, the Young's modulus is higher and the thermal conductivity is lower. It thus can be expected that the amplitudes of stress waves induced by pulsed beams are larger.

## 2.3 Ion matter interaction

During interaction of high-energy ions with matter, the projectiles lose their kinetic energy by different mechanisms depending on the ion energy (Figure 2.3 a)). For ions with energies in the keV-MeV range the nuclear energy loss dominates. Elastic collisions between the impacting ions and target atoms lead to displacements. If the knocked-out particle has enough energy, it may knock on further atoms resulting in an atomic collision cascade. This process ends when all involved particles come to rest. Vacancies, interstitials, defect clusters and dislocations are produced.

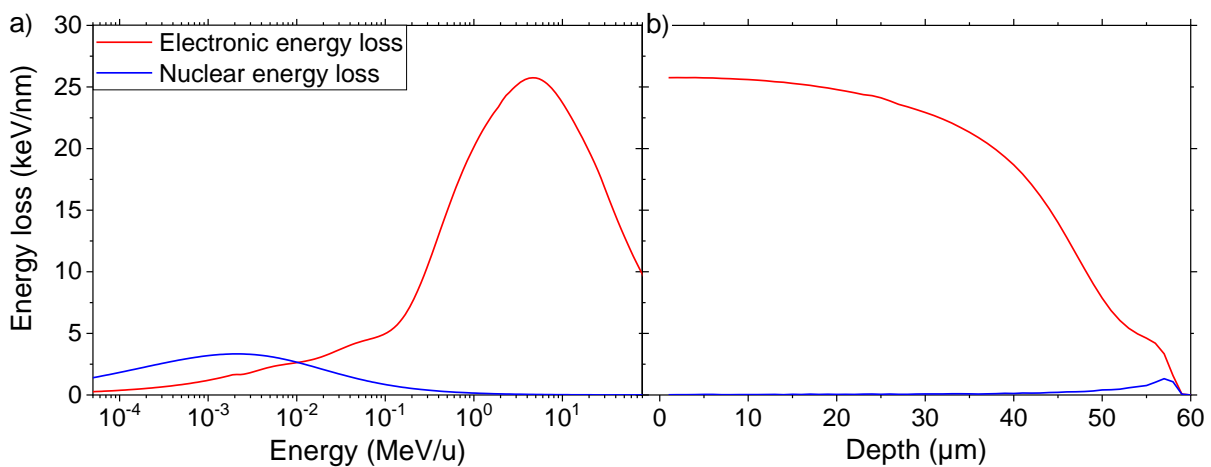


Figure 2.3: a) Electronic and nuclear energy loss as a function of the specific energy for uranium ions in a carbon target of a density of 1.84 g/cm<sup>3</sup> as calculated with the SRIM-2013 code [41]. b) Energy loss as a function of penetration depth of 4.8 MeV/u U ions in the same target.

For higher energies in the MeV-GeV range, the impacting ions mainly interact with the electrons of the target atoms leading to electronic excitation and ionization processes along the trajectory of the projectile [42]. Figure 2.3 a) shows a maximum of the electronic energy loss at about 4 MeV/u which is the so-called Bragg Peak. At energies below the Bragg peak the charge state of the impacting ions decreases leading to smaller Coulomb forces and hence a smaller electronic energy loss [43]. At energies above the Bragg Peak, the electronic energy loss decreases with increasing energy as the ionization cross-section is inversely dependent on the velocity of the ions [44]. The energy loss depends on the square of the atomic number  $Z$  of the projectile and on the density of the target material [45].

At even higher energies, leading to relativistic velocities of the particles, photons can be generated via Bremsstrahlung and Cherenkov radiation. Furthermore, for high energies nuclear reactions can occur. Electrostatic interaction between target nucleus and the projectile nucleus results in a repulsive force, the so-called Coulomb barrier. However, if this barrier can be overcome either due to a high enough kinetic energy of the projectile target or due to tunnelling through the barrier the short-range strong interaction dominates and the nuclei combine.

The dynamics of the energy deposition process can be separated into three stages. In the first stage at  $10^{-17}$  to  $10^{-16}$  s after the impact of an ion, free so-called  $\delta$ -electrons are generated. These electrons subsequently propagate in the target material after  $10^{-15}$  to  $10^{-14}$  s and cause new ionizations resulting in an electron cascade. This cascade of hot electrons occurs in a cold lattice. The energy transfer from the electrons to the atoms takes place in the third stage on a timescale of  $10^{-13}$  to  $10^{-10}$  s [46]. Depending on the target material a highly disordered track region can be left behind. In general, metals have a very low sensitivity requiring very high energy losses to generate tracks. High sensitivities for track formation are observed in insulators like polymers, oxides, and ionic crystals [46].

The formation of ion tracks can be described by the inelastic thermal spike model [47–49]. As electronic excitation and atomic movement occurs on different time scales, the thermal diffusions of the electronic and atomic subsystems are considered quasi-independent. The energy deposited by the projectile  $A(r,t)$  is transferred only to the electronic subsystem. The diffusion in the electronic subsystem is described by its temperature  $T_e$ , specific heat  $C_e$ , and thermal conductivity  $K_e$  at radius  $r$  and time  $t$  (Equation 2.1). The electronic subsystem is coupled to the atomic subsystem by electron-phonon coupling  $g(T_e - T_a)$ . Diffusion in the atomic subsystem is similarly described by its own set of temperature  $T_a$ , specific heat  $C_a$ , and thermal conductivity  $K_a$  (Equation 2.2).

$$C_e(T_e) \frac{\partial T_e}{\partial t} = \frac{1}{r} \frac{\partial}{\partial r} \left( r K_e(T_e) \frac{\partial T_e(r, t)}{\partial r} \right) - g(T_e - T_a) + A(r, t) \quad 2.1$$

$$C_a(T_a) \frac{\partial T_a}{\partial t} = \frac{1}{r} \frac{\partial}{\partial r} \left( r K_a(T_a) \frac{\partial T_a(r, t)}{\partial r} \right) + g(T_e - T_a) \quad 2.2$$

Once the energy is transferred to the lattice atoms, a thermal spike occurs. If the reached temperature is larger than the melting temperature of the material, local melting can occur in a cylindrical volume around the ion trajectory. This molten region is rapidly quenched due to the heat diffusion in the atomic subsystem.

In the MeV to GeV range investigated in this work, the contribution of photon generation and nuclear reactions to the energy loss can be neglected. The electronic energy loss is the dominating effect. The nuclear energy loss becomes relevant at the end of the ion range as can be seen in Figure 2.3 b).

---

## 2.4 Irradiation damage in graphite

---

Most literature available for the irradiation of graphite is of irradiation with neutrons due to its use as moderator in nuclear reactors. The most typical neutron radiation induced defect in graphite is the Frenkel pair defect. A carbon atom is knocked out of the basal plane, leaving a vacancy behind and occupying an interstitial position between the planes [50]. If a high density of defects is produced, adjacent vacancies go through a reconstruction process to reduce dangling bonds [51]. The formed di-vacancies can become the nucleus for dislocation dipoles resulting in contraction within the basal graphitic planes [52]. The dipoles can dissociate in two dislocations and form two incomplete planes. Interstitials can migrate and attach to the edges of the dislocations resulting in growth of the planes [53]. By this process new planes are formed resulting in growth perpendicular to the planes. During irradiation of isotropic graphite, at low and intermediate doses, this growth is accommodated by pores in the material. These pores stem from the thermal contraction during the cooling after the high temperature graphitization process [54,55]. At low fluences, the in-plane contraction dominates, leading to volume shrinkage. After the pores are closed, expansion perpendicular to the planes dominates the contraction within the planes resulting in an overall volume increase and generation of new pores [56,57].

---

For swift heavy ion irradiation, the electronic energy loss causes damage along the ion paths. It has been shown that ion tracks are observed in highly oriented pyrolytic graphite [58] which become continuous above a critical energy loss of 18 keV/nm [59]. Above this threshold a phase transformation towards a disordered structure similar to glassy carbon was observed by Raman analysis [8]. Large changes of the Young's modulus [5,60,61] and the thermal conductivity [8] were reported.

Due to the initial shrinkage and the pinning of slip planes by defects, the Young's modulus of graphite initially rises during irradiation. For neutron irradiation, the Young's modulus decreases after the pores existing in the pristine material are filled and graphite starts to expand [62]. The maximum increase of Young's modulus depends on the specific graphite material and irradiation parameters, varying between 250% and 500 % [57,63] for isotropic graphite irradiated with neutrons. For heavy ion irradiations, the hardness and Young's modulus rise with increasing fluence due to the accumulation of defects. A threshold surface energy loss of 18 keV/nm [60] is required for large changes of the Young's modulus of up to 280 % [61] or 500 % [60] and of the surface hardness up to 500 % [61] and 1500 % [60]. For carbon fibre composites, the increases of the Young's modulus are smaller as the larger pristine values result in smaller relative changes. They are reported to be between 14 % [64] and 40 % [65] for neutron irradiation and 130 % for 4.8 MeV/u Au ion irradiation [5].

---

## **3 Experimental**

---

This chapter describes details of sample preparation, ion irradiation as well as the characterization methods for both, in-situ methods and post-irradiation techniques.

---

### **3.1 Sample preparation**

---

PG, CFC and FG samples designated for post-irradiation experiments are cut to a diameter of 1 cm or square samples with a side length of 1 cm. The thickness of the samples is between 0.5 and 3 mm. The samples are lapped from the top resulting in an average surface roughness of less than 1  $\mu\text{m}$ . HOPG and GC samples are investigated as received from the producer. After irradiation the samples are glued on aluminium rings providing a stiff contact, which is a requirement for indentation and impact experiments.

PG, CFC, FG, and copper samples designated for in-situ methods are cut to discs with a diameter of either 1 or 2 cm. The thickness varies between 0.2 and 0.5 mm. Samples of PG, copper and CFC with in-plane fibre orientation are lapped from both sides achieving a roughness of less than 1  $\mu\text{m}$ . The transversal orientation of CFC is used as machined, because samples are rather thin and lapping results in visible gaps between the fibre planes. GC, tungsten and h-BN samples are used as received with similar dimensions. The thickness of all samples is measured with an accuracy better than 0.01 mm.

---

### **3.2 Ion beam irradiation**

---

The ion beam irradiations are conducted at the linear accelerator UNILAC at GSI Helmholtz Centre for Heavy Ion Irradiation which is schematically shown in Figure 3.1.

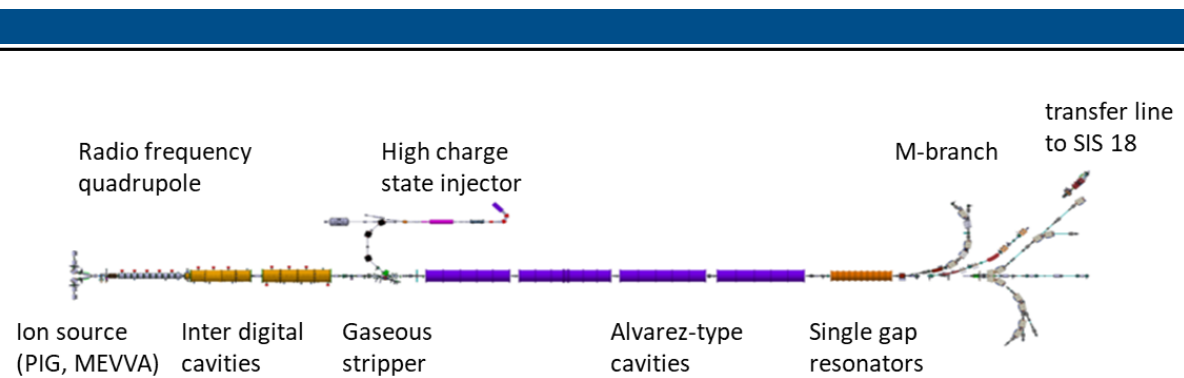


Figure 3.1: Schematic of the UNILAC linear accelerator of GSI adapted from [66].

Three ion source terminals are available: (1) Penning ionization gauge (PIG) which is the oldest still operated ion source. (2) A second terminal which can be equipped with four different ion sources and provides higher intensities. (3) High charge state injector which provides higher charge states. In this work C, Ca, Xe, Sm and Au beams are provided with the PIG source with a frequency of 3 to 50 Hz and a pulse length of up to 5 ms. U and Bi ions are generated from the second terminal with an equipped metal vapour vacuum arc (MEVVA) ion source resulting in a low duty cycle with a frequency of 0.5 to 2 Hz and a pulse length of 0.05 to 0.5 ms. The extracted beams from the PIG and MEVVA sources are bunched and pre-accelerated with a radio frequency quadrupole and further accelerated to 1.4 MeV/u in the inter digital cavities. To improve the efficiency of further acceleration, the outer electrons of the ions are stripped in a gas stripper. Five Alvarez-type cavities allow the acceleration of the ion beams to energies ranging from 3.6 and 11.6 MeV/u. Arbitrary energies in this range can be set by a section of single gap resonators. The obtained ion beam can be further accelerated in the ion synchrotron ring accelerator SIS 18

Most irradiation experiments in this work are performed at the M-Branch. The ions, directed by a kicker magnet from the UNILAC to the M-branch enter the cave with energies of 4.8 MeV/u close to the Bragg peak, providing maximum energy loss and thus fast dose accumulation. The low energy has also the advantage of rather limited sample activation. The M-branch has 3 beamlines (M1, M2, and M3) mainly for in-situ analysis. The M3-beamline used for the experiments houses several chambers (Figure 3.2).

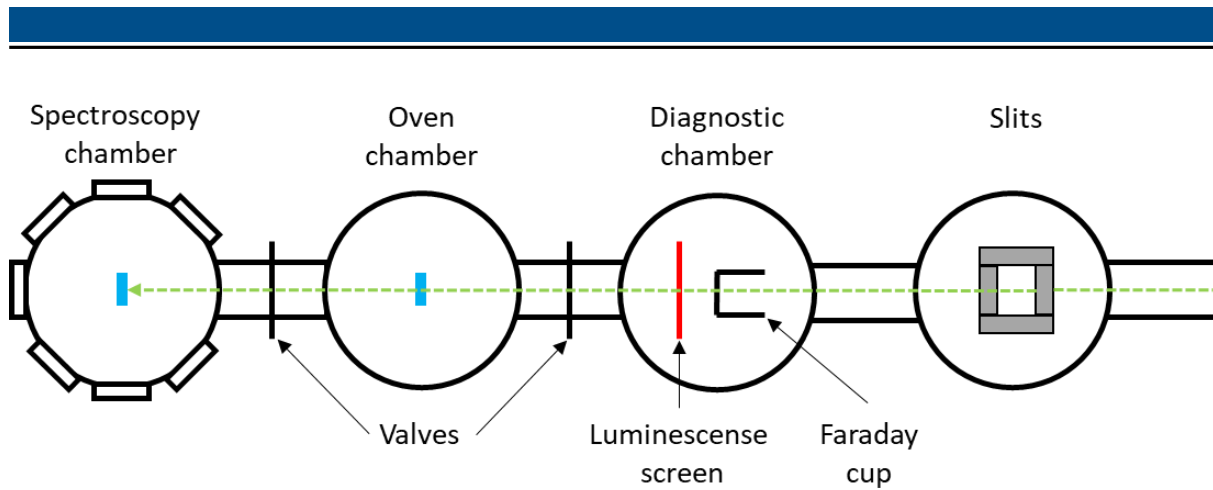


Figure 3.2: Schematic of the M3 branch of the UNILAC accelerator of GSI. The beam is marked by a green arrow and possible positions for sample irradiation are marked by blue squares.

Before reaching the irradiation chamber, the beam is shaped by horizontal and vertical slits into a square shape with lengths of few centimetres. In the diagnostic chamber the homogeneity and the size of the beam can be checked with a luminescence screen. Knowing the charge state of the ions, a Faraday cup measures the intensity of the beam and the slits are calibrated to measure the flux during the irradiation. The uncertainty of the accumulated fluences is estimated to be 20 %. During the sample irradiation, the luminescence screen and Faraday cup are moved out of the beam.

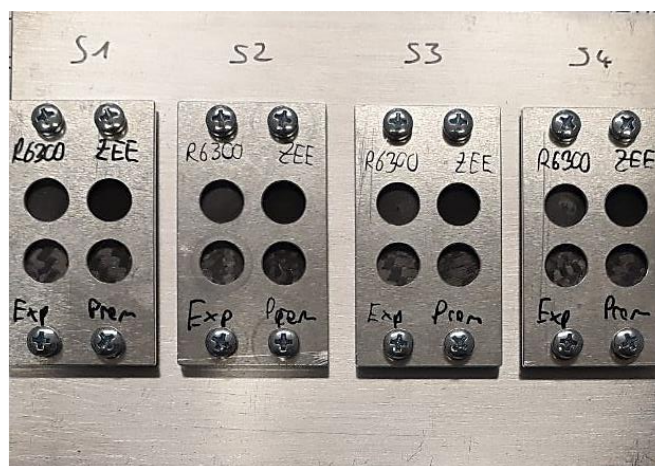


Figure 3.3: Sample holder with four graphitic samples on four positions (S1-S4) designated for experiments in the oven chamber. The holder can be moved in transversal direction to irradiate all four positions subsequently without opening the chamber.

The samples designated for post irradiation analysis are mounted in the oven chambers on holders as depicted in Figure 3.3 while samples for in situ analysis are placed in the spectroscopy chamber (more details in section 3.4.1). Additionally, some

samples are irradiated at the UNILAC beamline X0 with Au and Xe ions with an energy of 11.1 MeV/u.

The penetration depth and the energy loss of the ions in the materials are calculated using SRIM 2013 code [41] and are listed in Table 3.1 and Table 3.2 together with the accumulated fluences. In all cases the penetration depth is considerably lower than the sample thickness. This means that the ions are stopped in the samples and only the top layer of the samples is directly influenced by the beam.

Table 3.1: Irradiation parameters of the samples designated for post irradiation analysis.

Material	Ion	Energy [MeV/u]	Penetration depth [ $\mu\text{m}$ ]	Energy loss at surface [keV/nm]	Fluence range [ions/cm <sup>2</sup> ]
SGL R6650	C	5.9	108	0.4	$1 \times 10^{11}$ - $5 \times 10^{13}$
	Ca	4.8	44	3.7	$1 \times 10^{11}$ - $5 \times 10^{13}$
	Xe	4.8	50	14.8	$1 \times 10^{11}$ - $6.5 \times 10^{13}$
	Sm	4.8	59	15.7	$1 \times 10^{11}$ - $3 \times 10^{13}$
	Au	4.8	57	20.5	$5 \times 10^{12}$ - $7 \times 10^{13}$
	Au	11.1	122	17.7	$1 \times 10^{11}$ - $1.1 \times 10^{13}$
	U	4.8	58	25.7	$5 \times 10^{12}$ - $7 \times 10^{13}$
SGL R6300	Au	4.8	61	19.1	$1 \times 10^{11}$ - $5 \times 10^{13}$
POCO ZEE	Au	4.8	59	19.7	$1 \times 10^{11}$ - $5 \times 10^{13}$
Tatsuno AC150k	Xe	11.1	125	10.7	$1 \times 10^{11}$ - $1 \times 10^{13}$
	Au	3.6	51	18.5	$1 \times 10^{11}$ - $2 \times 10^{14}$
	Au	11.1	136	15.9	$5 \times 10^{12}$ - $5 \times 10^{13}$

Material	Ion	Energy [MeV/u]	Penetration depth [ $\mu\text{m}$ ]	Energy loss at surface [keV/nm]	Fluence range [ions/cm <sup>2</sup> ]
Tatsuno	Bi	4.8	63	19.3	$1 \times 10^{11}$ - $5 \times 10^{13}$
AC150k	U	4.8	64	23.1	$1 \times 10^{12}$ - $5 \times 10^{13}$
SGL Premium	Au	4.8	66	17.7	$1 \times 10^{12}$ - $5 \times 10^{13}$
SGL Experimental	Au	4.8	59	19.6	$1 \times 10^{12}$ - $5 \times 10^{13}$
HOPG	Au	4.8	47	24.9	$5 \times 10^{11}$ - $7 \times 10^{13}$
FG	Au	4.8	105	11.0	$5 \times 10^{12}$ - $7 \times 10^{13}$
	U	4.8	106	14.0	$1 \times 10^{11}$ - $5 \times 10^{13}$

Table 3.2: Irradiation parameters of samples designated for in situ experiments. All samples are exposed to 4.8 MeV/u U ions with a pulse length of 100 ms.

Material	Penetration depth [ $\mu\text{m}$ ]	Energy loss at surface [keV/nm]	Achieved maximum fluence [ions/cm <sup>2</sup> ]
SGL R6650	58	25.7	$3.5 \times 10^{13}$
SGL Premium	66	22.4	$2.2$ - $4.0 \times 10^{13}$
FG	106	14.0	$1.0 \times 10^{14}$
Sigradur G	75	19.9	$4.0 \times 10^{13}$
BN	56	26.8	$5.0 \times 10^{13}$
W	17	106.4	$6.3 \times 10^{12}$
Cu	23	76.6	$6.3 \times 10^{12}$

---

### 3.3 Post irradiation characterization

---

The following section summarizes the experiments conducted to characterize modified material properties after the samples are removed from the beamline. A short explanation of the working principle of Raman spectroscopy, nanoindentation and nanoimpact is given. The used instrumentation and measurement parameters are listed.

---

#### 3.3.1 Raman spectroscopy

---

Raman spectroscopy investigates the inelastic scattering of light to determine vibrational modes of investigated materials. Raman spectra and the specific vibration modes are influenced by material properties such as composition, crystallinity and crystal orientation.

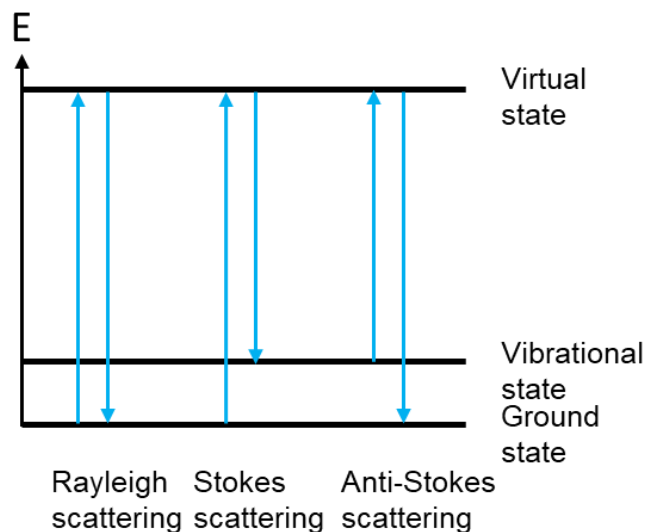


Figure 3.4: Energy levels of elastic (Rayleigh) and inelastic (Stokes and anti-Stokes) light scattering.

During interaction of photons with crystals or molecules most of the photons are scattered elastically which is called Rayleigh scattering. However, with a small probability, energy is transferred resulting in a change of the vibration energy of the crystal or the molecule. If the excited vibrational state has a higher energy, it is called Stokes scattering, if the final state is lower than the original state, it is called anti-Stokes

scattering (Figure 3.4). The energy difference between the incoming and the scattered photon of inelastic scattering is used in Raman spectroscopy to obtain information about the vibrational states of the investigated material. In practice, the monochromatic light of a laser is directed on the sample and the scattered light is recorded with a detector and compared to the initial wavelength of the laser.

Raman spectroscopy is frequently used for structural analysis of carbon materials [67,68]. Graphite and graphene belong to the  $P6_3/mmc$  ( $D_{6h}$ ) space group. According to group theory, graphene has only one Raman active mode which is doubly degenerate [69]. This  $E_{2g}$  mode corresponds to the in-plane vibration (Figure 3.5) and its Raman shift appears at a wavenumber of  $1582\text{ cm}^{-1}$ . By combining several graphene planes to form graphite, the graphene modes split. Two Raman active modes are obtained, one remaining at  $1582\text{ cm}^{-1}$ , the so-called G band, and one at  $42\text{ cm}^{-1}$  which cannot be detected with standard equipment due to its proximity to the Rayleigh scattering [69].

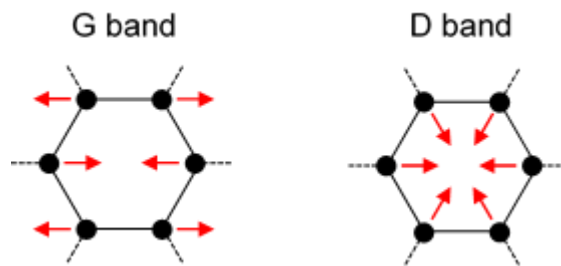


Figure 3.5: Schematic representation of the vibration modes responsible for the G and D band.

During Raman spectroscopy of isotropic graphite additional bands are observed (Figure 3.6 a)). Most prominent are the D band at  $\sim 1360\text{ cm}^{-1}$  [11], the D' band at  $1620\text{ cm}^{-1}$  and the 2D band at  $2720\text{ cm}^{-1}$  [70]. The D band appears only in defective graphite and is attributed to the  $A_{1g}$  breathing mode of six-atom rings [11,12,71]. It occurs due to double resonance involving two atoms [72] and is dispersive with the excitation energy [73]. The intensity ratio of the D band  $I_D$  and the G band  $I_G$  can be utilized to determine the crystallite size  $L_a$  (Equation 3.1) [11,74]. It has been shown that this relation depends on the fourth power of the used laser energy  $E_L$  [75].

$$L_a(\text{nm}) \approx \frac{(490 \pm 100)}{E_L^4} \left( \frac{I_D}{I_G} \right)^{-1} \quad 3.1$$

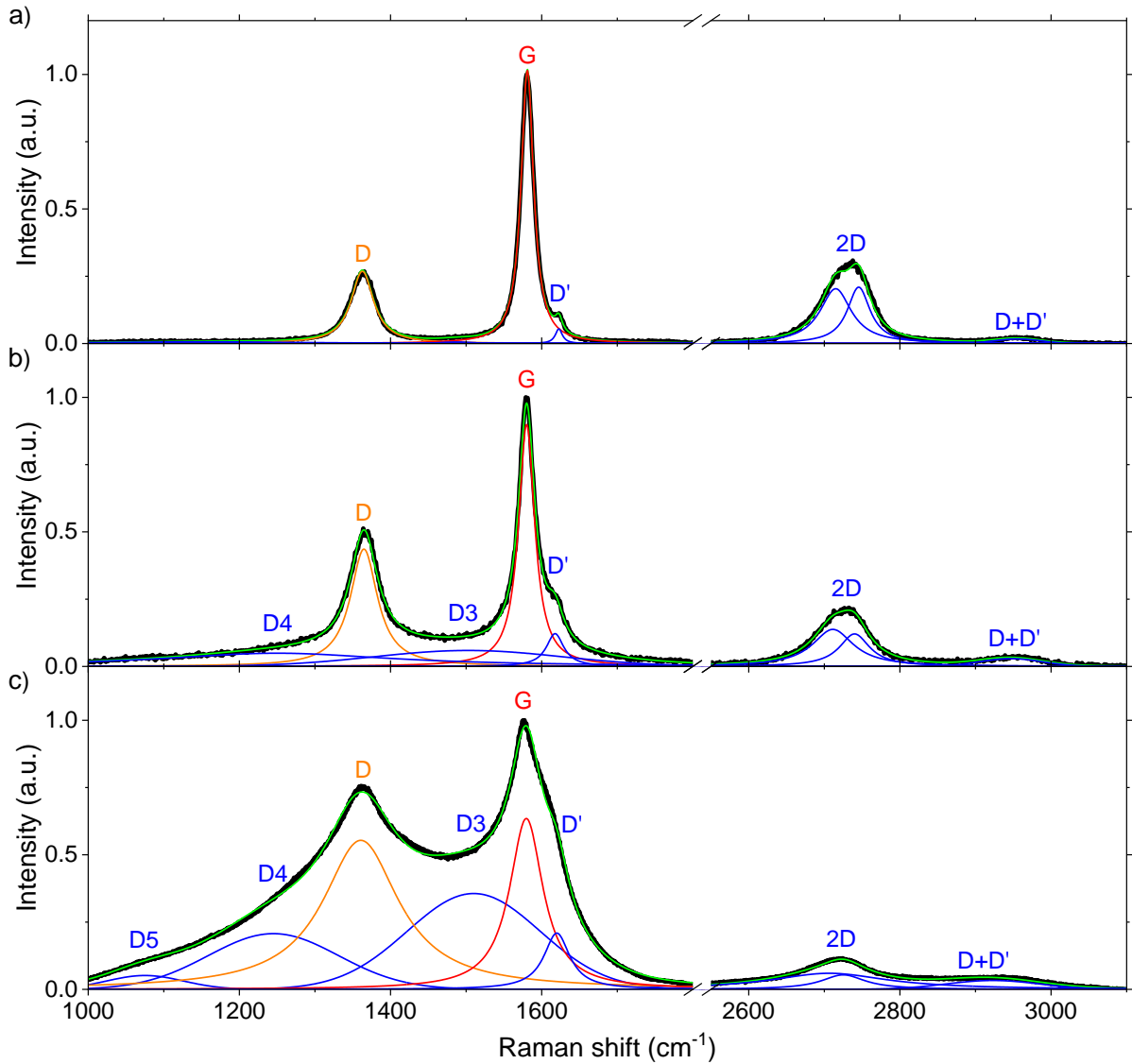


Figure 3.6: Background corrected Raman spectra (black) of isotropic graphite R6650. a) pristine b) irradiated with 4.8 MeV/u Au ions to a fluence of  $3 \times 10^{13}$  ions/cm<sup>2</sup> c) irradiated with 4.8 MeV/u U ions to a fluence of  $7 \times 10^{13}$  ions/cm<sup>2</sup>. Included are the deconvoluted Gaussian/Lorentzian peak fittings (G band in red, D band in orange, other bands in blue) and their sum in green.

This relation is however only valid for crystallite sizes larger than 2 nm [12]. Smaller crystallite sizes can be characterized using a local activation model [76–78] which is however not within the scope of this work. Cancado et al. proposed using the  $I_D/I_G$  ratio and the full width half maximum of the G band to distinguish between point and line

---

defects [79]. The D' band appears due to double resonance in an intra-valley process involving only one atom [67]. It was shown for graphene that the  $I_{D'}/I_D$  ratio can be used to classify the defect type [80,81].

The 2D band is the overtone of the D band and is hence dispersive as well [73]. However, it involves two photons with opposite wave vectors. Momentum conservation is satisfied without requiring defects and it thus also appears in perfect graphite or graphene [82]. It cannot be sufficiently fitted with one band and is fitted with 2 bands [82]. Larouche and Stansfield proposed using the 2D band to determine the average continuous graphene length [83]. It describes the total length of several crystallites connected to a curved graphene sheet. For amorphous carbon or carbon soot the broad D3 band occurs at  $\sim 1500\text{ cm}^{-1}$  [84]. In highly disordered graphite additionally the D4 band at  $\sim 1250\text{ cm}^{-1}$  and the D5 band at  $\sim 1100\text{ cm}^{-1}$  are detected [84,85]. Together with the overtone D+D' at  $\sim 2950\text{ cm}^{-1}$  they are required for a good fit, however detailed structural implications are not known to this day.

Based on the different bands above and summarized in Table 3.3 [6,83] deconvolution of Raman spectra yields converging fits of isotropic graphite samples, both pristine and irradiated with ions with an energy loss below  $18\text{ keV/nm}$  or a fluence below  $1 \times 10^{13}\text{ ions/cm}^2$  for ions with an energy loss above  $18\text{ keV/nm}$  (Figure 3.6 a) and b)). However, for irradiation at higher fluences of  $4.8\text{ MeV/u Au}$  and  $\text{U}$  ions the relative intensity of the first order D bands and the full width half maximum of all the bands become very large. If the bands are fitted without constraints, the D4 band shifts towards the D band and the D3 and D' band shift towards the G band resulting in unreasonable results. To prevent this, the bands are fixed for these samples at the respective positions observed at lower fluences where the fits converged in reasonable results. These are listed in Table 3.3 and a resulting fit is shown in Figure 3.6 c).

Table 3.3: List of bands included in the deconvolution of the Raman spectra using a laser of wavelength 473 nm. The Raman shift column show the ranges used for the deconvolution of the graphite samples. For cases of high disorder, where certain bands needed to be fixed the band position is noted in brackets.

Band	Raman shift [ $\text{cm}^{-1}$ ]	Band shape	Characterization
D5	1080-1150	Gaussian	-
D4	1200-1300 (1260)	Lorentzian	-
D	1355-1370	Lorentzian	Defective graphite [11,12,71]
D3	1480-1530 (1510)	Gaussian	Amorphous carbon [84]
G	1570-1590	Lorentzian	Ideal graphite [11]
D'	1610-1630 (1620)	Lorentzian	Classify defect type [80,81]
2D1	2700-2725	Lorentzian	Overtone of D band [82]
2D2	2725-2755	Lorentzian	Overtone of D band [82]
D+D'	2900-3000	Lorentzian	-

Raman spectroscopy measurements are conducted using a LabRAM HR 800 (Horiba Jobin Yvon) spectrometer. Blue light with a wavelength of 473 nm ( $E_L = 2.62$  eV) from a Cobolt Blues CW diode pumped laser is used. The probing depth for this wavelength is approximately 50 nm. The beam spot has a diameter of 2.5  $\mu\text{m}$  for the used x100 objective. The backscattered light is dispersed on a grating with 1800 grooves/ $\text{mm}^2$  and detected with a Peltier cooled CCD detector.

Before each measurement the spectrometer is calibrated to the 520  $\text{cm}^{-1}$  band of a silicon sample. For all samples the spectra from at least 25 positions are recorded and averaged. The spectra are measured in the wavenumber range from 800 to 3200  $\text{cm}^{-1}$ . The spectral windows are measured twice for a duration of 20 s. The intensity of the Raman spectra depends on the parameters of the set-up and the sample orientation. Hence, all the spectra are normalized to the intensity of G band and only the relative intensities and the full width at half maximum of the bands are considered. Background

---

correction and fitting of the recorded spectra are performed using Fityk 1.3.1 software [86] with the band shapes and Raman shift boundaries summarized in Table 3.3.

---

### 3.3.2 Micro- and nanoindentation

---

Traditional indentation experiments are conducted by pressing a hard tip of known material and geometry into a material with unknown properties. The hardness can be obtained from the ratio of the applied load and the area of the indent which can be measured using optical microscopy. However, in cases where the size of the indents needs to be scaled down like e.g., because of limited sample volume or limited layer thickness the indents are not visible by optical microscopy. To circumvent this, micro- and nanoindentation track the depth position of the indenter tip during the indentation. The obtained depth can be used to deduce the area of the indent if the shape of the indenter tip is known. This allows the determination of the hardness of indents with a size of several micrometres or tens to hundreds of nanometres for micro and nanoindentation, respectively.

A typical result of a load vs. depth curve is shown in Figure 3.7. The load is increasing until a predefined maximum depth is reached. For microindentation experiments a maximum depth of 10  $\mu\text{m}$  is selected. This depth is chosen since it is large enough to penetrate several grains of graphite and at the same time small enough to avoid the influence of the non-irradiated substrate below the irradiated layer. A depth of 10  $\mu\text{m}$  is also large enough to avoid depth dependence of the indents (cf. Figure 4.27). The loading rate is adapted to the different materials to obtain a total loading time of approximately 30 s. Loading results in a combination of plastic and elastic deformation. Once the maximum load  $P_{max}$  is reached, the load is held for 20 s allowing plastic creep to occur. Afterwards the load is linearly released until no force is applied anymore, only interrupted at 10 % of the maximum load, where the load is held for 60 s to correct the measured signal by the thermal drift of the system. The unloading should only recover the elastic deformation and result in no further plastic deformation.

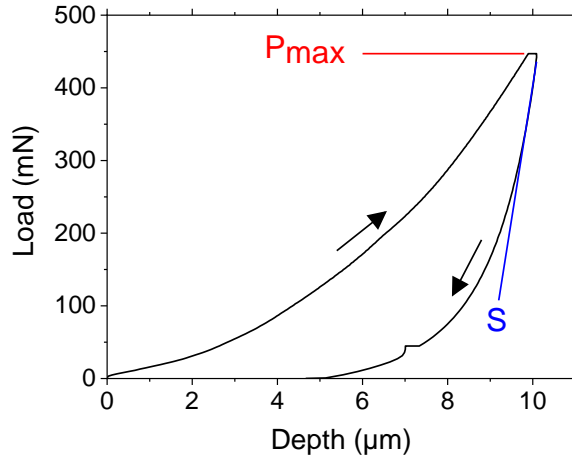


Figure 3.7: Load as a function of depth of an indentation experiment of isotropic R6650 graphite. Marked are the maximum load  $P_{max}$  and the initial unloading slope  $S$ .

The measurements are analysed by the Oliver-Pharr method [13,14]. A non-linear function is fitted to the unloading curve. This fit is used to determine the initial slope of the unloading curve  $S$ . An area function ( $F(h)$ ), describing the projected area of the indenter tip as a function of the depth (Equation 3.2).

$$A = F(h) \quad 3.2$$

To calculate the hardness, first the contact depth  $h_c$  needs to be calculated by subtracting from the maximum depth  $h_{max}$  the part that had no contact with the indenter tip due to sink-in of the material (Equation 3.3). As the unloading curve is almost completely elastic, the initial unloading slope  $S$  represents the elastic contribution.  $\varepsilon$  is a value that depends on the indenter geometry.

$$h_c = h_{max} - \varepsilon \cdot \left( \frac{P_{max}}{S} \right) \quad 3.3$$

By inserting the contact depth  $h_c$  in the diamond area function (Equation 3.2), the hardness  $H$  can be determined (Equation 3.4).

$$H = \frac{P_{max}}{A(h_c)} \quad 3.4$$

---

The completely elastic unloading curve can furthermore be used to deduce the Young's modulus  $E$ . First the reduced modulus  $E_r$  is calculated (Equation 3.5).

$$E_r = \frac{\sqrt{\pi} \cdot S}{2 \cdot \beta \cdot \sqrt{A(h_c)}} \quad 3.5$$

The  $\beta$ -factor depends on the indenter geometry and corresponds to  $\beta = 1.034$  for a Berkovich indenter. Since both the investigated material and the indenter tip deform during the indentation experiment, the influence of the tip needs to be subtracted. Knowing the Poisson's ratio  $\nu$  of the investigated material and of the properties of the diamond indenter tip (Young's modulus  $E_i = 1197$  GPa, Poisson's ratio  $\nu_i = 0.07$ ) the Young's modulus of the investigated material (Equation 3.6) can be determined.

$$\frac{1}{E_r} = \frac{1 - \nu^2}{E} + \frac{1 - \nu_i^2}{E_i} \quad 3.6$$

In this work, indentation experiments are performed with a NanoTest Vantage produced by Micro Materials. It contains a nano- and a microindentation platform both using a pendulum-based system as depicted in Figure 3.8. The indenter tip is mounted on the pendulum. The force is applied to the pendulum by a coil on top of the pendulum. The resulting depth of the indenter tip is measured by a plate capacitor mounted behind the indenter tip. The samples are mounted on a movable XYZ-stage allowing indentation at the desired positions. For targeted indentations the samples can be inspected with an integrated optical microscope. On the bottom of the pendulum a damping plate is mounted to reduce the noise of the system to less than one nanometre.

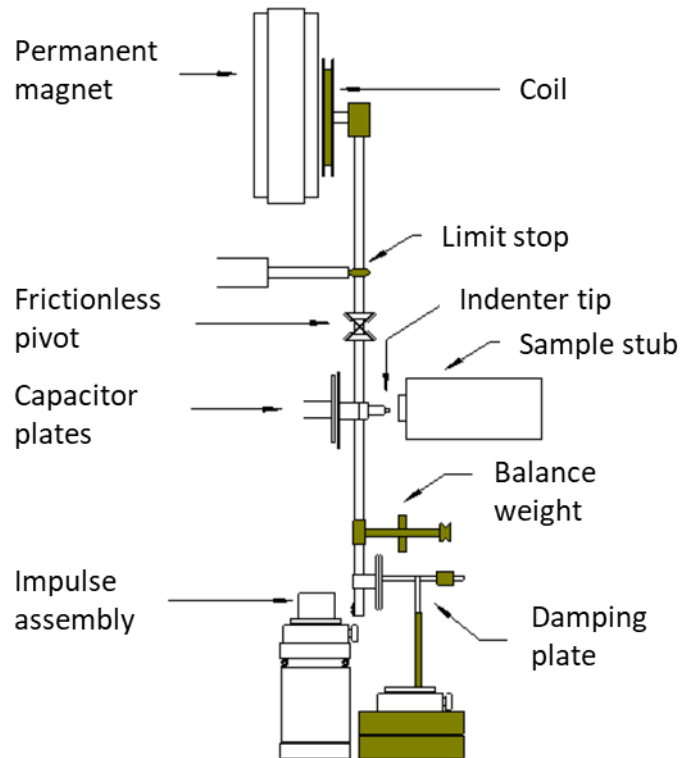


Figure 3.8: Schematic set-up of the nanoindentation platform of the NanoTest Vantage produced by Micro Materials. Adapted from [15].

Indentation experiments except on HOPG and targeted indentations of the fibres of CFC are conducted with the microindentation platform using a diamond Berkovich tip. It has the shape of a three-sided pyramid with a total angle of  $142.3^\circ$ . While it has the same area-to-depth ratio as a Vickers indenter, the three-sided geometry is easier ground to a sharp point required for accurate measurements at shallow depths.

Due to the small size of the fibres, targeted indentations of matrix and fibres of CFC were conducted with the nanoindentation platform using a Berkovich indenter to a maximum depth of 500 nm requiring a force of  $\sim 1-10$  mN,.

A possible source of error in these measurements is the relatively large surface roughness of up to  $1 \mu\text{m}$ . However, using the built-in light microscope, very rough spots on the surface (e.g., pores) were avoided and it can be expected that the examined areas will have a local roughness that is significantly lower than the indentation depth. Examination of the indentation results did not reveal any significant increase in data scattering compared to the microindentation results for the same material. Therefore,

---

even though roughness is considered a possible source of error, the measurements should still represent valid results.

For indentation experiments on HOPG a spheroconical diamond tip with a diameter of 3.125  $\mu\text{m}$  is chosen as the Berkovich tip results in pop-ins because of the sharp edges cutting through the ordered graphite layers [5]. Load controlled nanoindentation experiments with a force of 5 mN corresponding to depths of  $\sim 300$  nm are performed to determine the depth dependence of mechanical properties along the ion path (more details in chapters 4.1 and 4.2.4). The obtained depth of  $\sim 300$  nm is an order of magnitude smaller than the radius of the indenter tip, preventing influence of the part of the tip which is not spherical but conical.

---

### 3.3.3 Nanoimpact

---

With normal indentation experiments it is only possible to determine quasi-static properties. The impact of intense, pulsed ion beams, however, results in dynamic loads with high strain rates. More realistic conditions are thus achieved if the indenter is operated in the impact mode [87,88]. For this the indenter impacts the sample from a distance  $d$  from the sample surface under a defined acceleration force  $F$ . When hitting the sample, the kinetic energy is transformed into elastic and plastic deformation of the sample. The elastic deformation is reversed resulting in repulsion of the indenter tip. These two processes alternate and further impacts occur but their amplitude decays exponentially as illustrated in Figure 3.9.

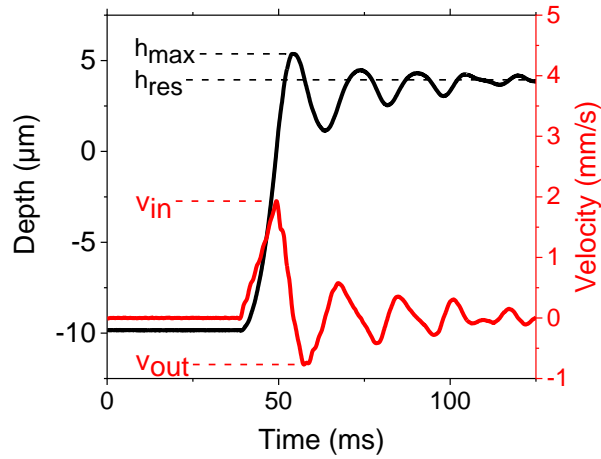


Figure 3.9: Depth and velocity signal of a dynamic hardness measurement on pristine isotropic R6650 graphite. A Berkovich indenter tip is accelerated at 38 s from a distance of  $\sim 10 \mu\text{m}$  to the sample surface with a force of 50 mN. Marked are the maximum and the residual penetration depth ( $h_{max}$  and  $h_{res}$ ), and the incoming and outgoing velocity ( $v_{in}$  and  $v_{out}$ ) of the indenter during the first impact.

To relate the nanoimpact measurements to effects induced by the impact of an intense, pulsed ion beam the strain rate  $\dot{\epsilon}(t)$  is evaluated (Equation 3.7) using the velocity  $v(t)$  and the depth  $h(t)$  [89].

$$\dot{\epsilon}(t) = \frac{v(t)}{h(t)} \quad 3.7$$

A typical result of the behaviour of the strain rate as a function of the depth can be seen in Figure 3.10. The strain rate after contact with the sample surface is in the order of  $10^4$  to  $10^5$  1/s and quickly reduces during penetration. The initial reduction of the strain rate can be fitted using equation 3.8, where  $a$  and  $m$  are fitting parameters [90].

$$\dot{\epsilon}(t) = a \cdot h(t)^m \quad 3.8$$

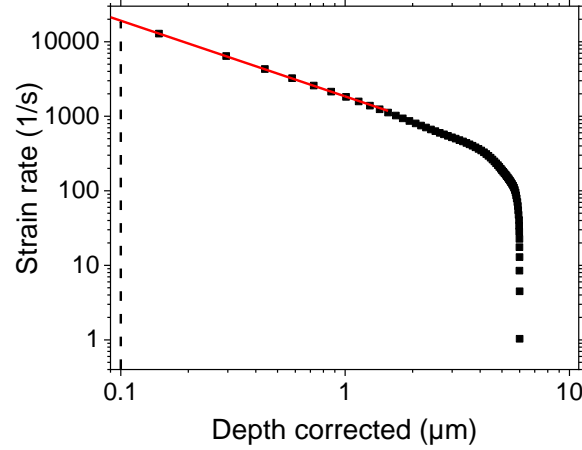


Figure 3.10: Strain rate as a function of depth of the first nanoimpact on pristine isotropic R6650 graphite impacted with a Berkovich indenter. The initial distance is 10  $\mu\text{m}$  and the acceleration force 50 mN. The red line represents a fit to the initial data. The black dotted line is at 50 nm where the strain rate is determined to compare between measurements with different impact parameters.

For comparison of different measurements, it was suggested by Zehnder et al. [89] to evaluate the strain rate at 50 nm (SR50) which, while still being close to the surface, avoids surface effects or the bluntness of the indenter tip that could result in deviation from equation 3.8.

The force applied during the nanoimpact cannot be measured with the standard set-up. Thus, the dynamic hardness  $H_{dyn}$  cannot be determined with the traditional force-based method of Oliver and Pharr. It is therefore typically determined by an energy based approach by using equation 3.9 [89,91–93]. It assumes that the difference between the incoming  $E_{kin,in}$  and outgoing  $E_{kin,out}$  kinetic energy of the first bounce is converted in plastic deformation of the volume  $V(h_{res})$  determined by the residual depth  $h_{res}$  at the end of the measurement.

$$H_{dyn} = \frac{E_{kin,in} - E_{kin,out}}{V(h_{res})} \quad 3.9$$

Several issues have to be considered for the validity of equation 3.9. First of all, if the bounces after the first impact result in additional plastic deformation the residual depth cannot be used anymore since only the loss of kinetic energy of the first impact is considered. However, it has recently been shown that this is not the case and the

---

subsequent bounces remain in the elastic regime [94,95]. Additionally, the residual depth is measured with the acceleration load still applied. This results in elastic deformation leading to an overestimation of the residual depth. It has been considered to determine the residual depth after the first impact at the time of contact of the second impact of the bouncing indenter tip [89,91]. However, this generates new problems as the second impact needs to hit the sample exactly at the same location. Furthermore, ringing of the pendulum can occur [89,93]. This makes the determination of the maximum velocity of the second impact to be very challenging. During the evaluation of the experiments, it is noted that the depth at the second impact is underestimated resulting in huge hardness values. Accordingly, the residual depth at the end of the measurements is utilized in equation 3.9 which delivers more reasonable results.

Another issue to consider is the amount of kinetic energy that is not transformed in plastic deformation but dissipated in the system. It was shown by Rueda-Ruiz et al. [95] that this can significantly overestimate the dynamic hardness. However, this effect is strongest for elastic materials with large Yield stress to Young's modulus ratio. The used graphitic materials have a Yield strength of 10 to 100 MPa and a Young's modulus of ~10 GPa. According to Rueda-Ruiz et al. this corresponds to an underestimation of the volume of approximately 10 % [95] compared to the force based approach of Oliver and Pharr Equation 3.4 [13,14].

All these effects need to be considered for the comparison of static and dynamic hardness measurements. As the nanoimpact technique was only developed recently, no universally accepted way of determining the parameters is established yet. Furthermore, most of the literature available so far exists for metals [91,95], glasses [89] or hard coatings [92]. To investigate the effects of swift heavy ion irradiation on the dynamic mechanical properties of graphite, the evaluation of the nanoimpact experiments is divided in two steps. First, the behaviour of pristine graphite is explored. The influence of the impact velocity and the indenter tip on the results of the three isotropic graphite grades with different microstructures is studied. Afterwards the effect of heavy ion irradiation on the different materials is investigated.

### 3.3.4 Multiple impulse

Nanoimpact measurements are used to investigate the material resistance to high strain rates. In order to simulate effects due to perpetual pulsed beams, multiple impulse experiments are performed [96]. As explained in the previous chapter, the indenter tip is brought into a predetermined distance from the sample surface and accelerated with a constant force towards the sample. In contrast to the nanoimpact experiments, the depth signal is recorded with a much lower temporal resolution. Thus, the bouncing of the pendulum is not monitored, but only the residual depth at the end of the impact. After the impact cycle is finished, the indenter is moved back to the initial distance and the process is repeated several times. Compared to the nanoimpact measurements, the detection of the surface is more prone to errors as the velocity is not recorded due to the low temporal resolution. Accordingly, the initial distance of the indenter is determined by contacting the sample at a position close to the desired impact position. This results in an uncertainty in the order of the sample roughness (typically  $\sim 1 \mu\text{m}$ ).

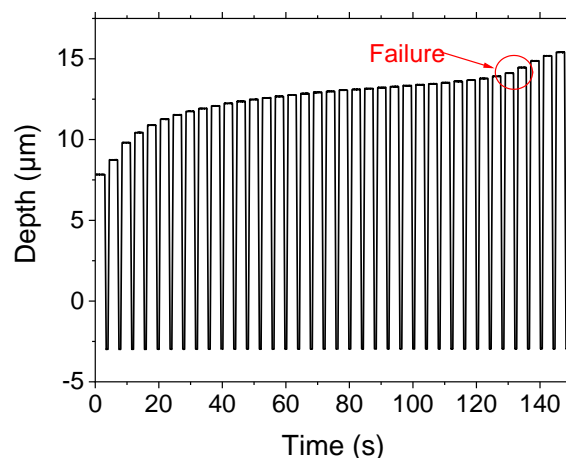


Figure 3.11: Multiple impulse experiment for isotropic R6650 graphite with 38 cycles. A Berkovich indenter tip is accelerated from a distance of  $\sim 3 \mu\text{m}$  to the sample surface with a force of 30mN. Failure of the material can be observed after 32 cycles indicated by a non-linear increase of the depth vs. time evolution (red cycle).

A resulting depth vs. time plot of a series of 38 impacts is shown in Figure 3.11. The initial impact results in a combination of elastic and plastic deformation. After removal of the indenter tip, the elastic part will recover while the plastic deformation remains. The second impact hence hits from a slightly larger distance and further increases the

---

impact depth. This process is repeated with each new impact and increases the impact depth. However, the increase in additional depth decreases exponentially as can be seen up to ~120 s in Figure 3.11. This evolution is interrupted at ~130 s due to a failure event indicated by the observation that the slope of the depth curve rises again. This is ascribed to additionally generated plastic deformation and is a typical indication of fatigue failure of the material. By repeating this experiment  $N$ -times at different positions, a statistical analysis of the failure probability  $P(f)$  (equation 3.10 [96]) as a function of the impact cycle  $f$  can be taken from the number of measurement  $n(f)$  that showed a failure up to that impact number  $f$ .

$$P(f) = \frac{n(f)}{N + 1} \quad 3.10$$

---

## 3.4 In situ measurements

---

In this section, the in-situ characterization experiments conducted during the beam times are presented. While offline analysis requires individual samples for different fluences, online analysis can be conducted with just one sample for which the fluence is step-wise increased. In situ experiments therefore avoid sample-to-sample fluctuations and allow a continuous determination of beam-induced property changes. Furthermore, dynamic effects like vibrations and stress waves can only be observed on-line during the irradiation. The used irradiation set-up is custom-built and thus explained in detail.

---

### 3.4.1 Measurement of beam-induced vibrations and stress waves by laser Doppler vibrometry

---

To investigate the effects of pulsed beams, the ideal solution is to directly observe the impact of beam pulses on the target. Observables that can be measured are the temperature using an infrared camera and the velocity and displacement of the target surface at selected positions either by a laser Doppler vibrometer (LDV) or strain gauges. Experiments measuring effects induced by pulsed beams were previously

conducted at the HiRadMat beamline at CERN [97–101], at Brookhaven National Laboratory [102] and at SIS18 at GSI [103]. This work presents results from irradiations with  $\sim 1$  GeV uranium ions at the UNILAC linear accelerator at GSI. The ion mass is higher and the energy lower than beams used in earlier studies [97–103]. Such beam conditions allow efficient monitoring of the response of the target materials under high-intensity short beams pulses and as a function of radiation damage accumulation. Experiments with accelerated dose accumulation are important in order to test the suitability of production target or beam dump materials under long-term operation conditions.

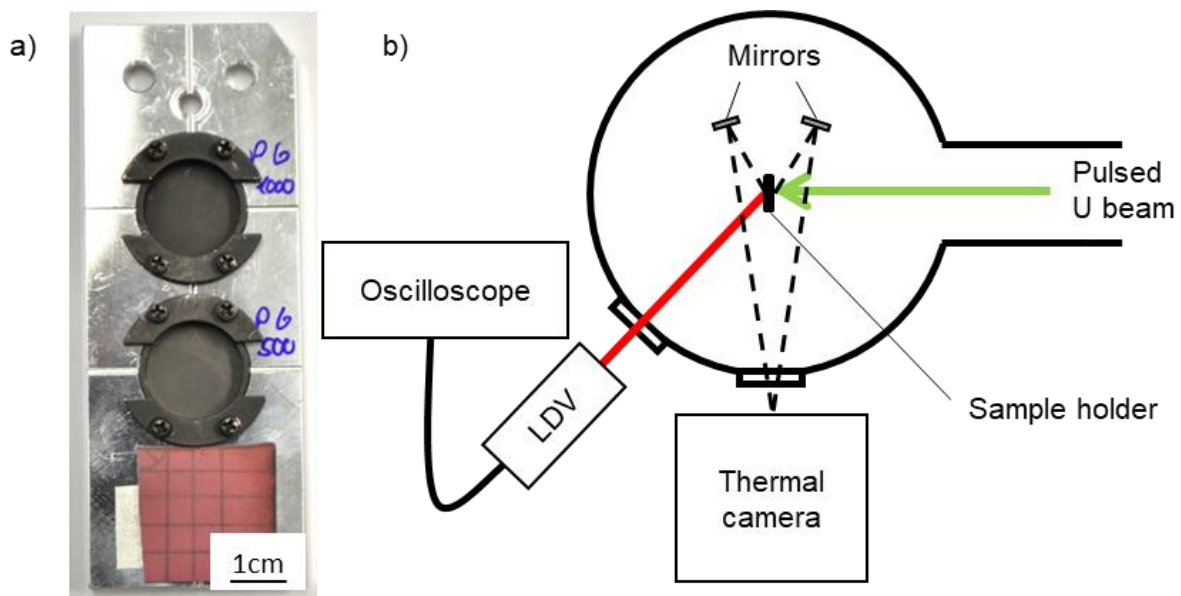


Figure 3.12: a) Sample holder with two graphite samples mounted above a luminescence screen and b) schematic set-up for online monitoring of elastic waves on the rear side of the irradiated samples by a laser Doppler vibrometer (LDV). The temperature on both sample surfaces is monitored with a thermal camera. The experiments are conducted at the M3 beamline at UNILAC.

To measure beam-induced vibrations and stress waves, high thermal stresses are required. Highest energy depositions can be achieved with ions of high mass and energy close to the Bragg peak. Furthermore, the beam pulses should be short. Accordingly, a 4.8 MeV/u U ion beam of pulse length of 50 to 100  $\mu\text{s}$  is used. The pulse repetition rate is 0.5 Hz. These beam parameters lead to an energy deposition of  $\sim 3 \text{ MW/cm}^3$ .

---

Since the beam-induced vibrations are mainly parallel to the direction of the beam, a LDV is superior than strain gauges for the detection of the velocity of the sample surface. To simplify the analysis of the detected signal a simple geometry with good accessibility of the laser beam is required. Disc-shaped samples with diameters of 1 or 2 cm are mounted in ring-shaped sample holders similar to the one shown in Figure 3.12 a). Due to the limited ion range, the thickness of the samples is reduced to values between 0.1 and 1 mm by lapping from both sides. The outer millimetre of the samples is clamped to the holder with low force to obtain free boundary conditions, resulting in a quasi-free-standing disc of 8 or 18 mm in diameter. The holders are mounted in the spectroscopy chamber of the M3 beamline using the set-up depicted in Figure 3.12 b). The beam is shaped with the horizontal and vertical slits, resulting in a square-shaped homogenous beam spot of 10×10 mm<sup>2</sup> positioned in the centre of the samples. For some samples an additional mask with circular holes of different sizes is used to expose the sample to circular beam spots. Position, shape and homogeneity of the beam are controlled with a luminescence screen mounted on the sample holder as shown in Figure 3.12 a). Beam-induced heating is controlled with a thermal camera and the beam flux is adapted such that the temperature stays below 200 °C. This prevents annealing of the generated defects and secures that the properties of the target materials remain close to the values at room temperature given in the data sheets. The thermal camera is positioned normal to the beam axis observing at the same time the temperature on the front and back side of the sample with help of two infrared gold mirrors.

The surface velocity related to beam-induced bending and stress waves in the samples is measured with a Polytec OFV-525/-5000-S LDV. The laser is directed towards the backside of the sample and reflected from the surface. The frequency of the reflected light of a moving object is changed due to the Doppler effect. Comparing the frequency shift of the reflected light to the initial laser signal allows the determination of the velocity of the sample surface. This information provides the frequency and amplitude of thermo-elastic stress waves. The LDV is aligned at the rear side at 45° angle to avoid any beam-induced damage to the LDV and the corresponding view port at the beamline. A tiny piece of adhesive reflective tape with an area of about 1 mm<sup>2</sup> is glued at the centre of the sample to increase the reflectivity for the laser beam and to avoid

the loss of the reflected laser beam during surface displacement. The LDV is connected to an oscilloscope. If required, the ion beam is switched off before each LDV measurement to let the samples cool down to room temperature. Subsequently, the velocity signal generated by the first pulse, after switching on the beam again, is recorded.

---

### 3.4.2 Numerical calculation of bending and stress wave frequencies of a circular disc

---

The generated heat in the beam spot leads to thermal expansion of the material. Since the heating is initially affecting only one surface of the disc, bending modes are generated. To understand the signal measured by the LDV, the expected bending frequencies of a fixed and a free circular plate need to be calculated. In general the vibration of a thin plate can be approximated with the governing differential equation of the Kirchhoff-Love theory (Equation 3.11) [104,105].

$$D\nabla^4 w + \rho_A \frac{\partial^2 w}{\partial t^2} = 0 \quad 3.11$$

$\nabla^4 = \nabla^2 \nabla^2$ , with the Laplacian operator  $\nabla^2$ ,  $w$  is the transverse displacement,  $\rho_A$  is the mass density per unit area, and  $t$  is the time.  $D$  is the flexural rigidity given by equation 3.12

$$D = \frac{Eh^3}{12(1-\nu^2)} \quad 3.12$$

with  $E$  being the Young's modulus,  $h$  the thickness and  $\nu$  the Poisson's ratio. The displacement  $w$  can be expressed using equation 3.13.

$$w = W \cos \omega t \quad 3.13$$

$\omega$  is the radial frequency and  $W$  is a function that depends only on the position. The substitution of equation 3.13 in equation 3.11 yields equation 3.14 using  $k^4 = \rho_A \omega^2 / D$ .

$$(\nabla^4 - k^4)W = 0 \quad 3.14$$

For the case of a cylindrical plate, polar coordinates can be used transforming equation 3.14. into equation 3.15.

$$\left[ \frac{d^2 W_n}{dr^2} + \frac{1}{r} \frac{dW_n}{dr} - \left( \frac{n^2}{r^2} - k^3 \right) W_n \right] \left[ \frac{d^2 W_n}{dr^2} + \frac{1}{r} \frac{dW_n}{dr} - \left( \frac{n^2}{r^2} + k^3 \right) W_n \right] = 0 \quad 3.15$$

$n$  is the order of vibration. The solutions to this differential equation are the Bessel functions of first  $J_n(kr)$  and second  $Y_n(kr)$  kind and the modified Bessel function of the first  $I_n(kr)$  and second  $K_n(kr)$  kind. The functions of the second kind are discarded as they result in infinite displacements at  $r = 0$ . The vibration modes  $W_n$  can be obtained with equation 3.16:

$$W_n = [A_n J_n(kr) + C_n I_n(kr)] \cos n\theta \quad 3.16$$

The parameters  $A_n$  and  $C_n$  are determined using the boundary conditions. For fixed boundary conditions at the outer radius  $a$  equation 3.17 is obtained.

$$\frac{J_n(ka)}{J_{n+1}(ka)} + \frac{I_n(ka)}{I_{n+1}(ka)} = 0 \quad 3.17$$

For free boundary conditions equation 3.18 is obtained, where the primes indicate differentiation with respect to the argument  $ka$  [106].

$$\frac{J_n(ka)}{J'_n(ka)} - \frac{[k^2 a^2 + 2(1 - \nu)n^2] \frac{I_n(ka)}{I'_n(ka)} - 2ka(1 - \nu)}{k^2 a^2 - 2(1 - \nu)n^2} = 0 \quad 3.18$$

The LDV measurements record the velocity in the centre of the disc-shaped sample. Thus, only modes without nodal diameters are observed, corresponding to  $n = 0$  and in consequence equation 3.18 simplifies to equation 3.19.

$$\frac{J_0(ka)}{J_1(ka)} + \frac{I_0(ka)}{I_1(ka)} = \frac{2(1-\nu)}{ka} \quad 3.19$$

Equation 3.17 and equation 3.19 can be numerically solved to obtain the eigenvalues  $ka$  and calculate the bending frequencies  $f_b$  using equation 3.20.

$$f_b = \frac{k^2}{2\pi} \cdot \sqrt{\frac{E \cdot h^2}{12 \cdot \rho \cdot (1-\nu^2)}} \quad 3.20$$

Due to the short time of the ion pulse, the thermal inertia of the outer material prevents the expansion of the heated beam spot causing thermal stress. This stress generates stress waves which travel through the sample and are reflected at the faces at interfaces. The frequency of the transversal elastic wave  $f_{tr}$ , which is reflected between the back and front surfaces of a thin disc is calculated using equation 3.21 [107].

$$f_{tr} = \frac{1}{2 \cdot t} \cdot \sqrt{\frac{E \cdot (1-\nu)}{\rho \cdot (1+\nu) \cdot (1-2\nu)}} \quad 3.21$$

The frequencies expected for the transversal stress waves are typically three orders of magnitude larger allowing an easy differentiation between the two modes.

---

### 3.4.3 Analyzation of the velocity signal

---

The velocity signals obtained from the LDV measurements are analysed using fast Fourier transformation (FFT). Due to strong damping, the frequency resolution of some samples is too low to allow quantitative investigation of beam-induced frequency changes. For these samples the velocity signals are zero-padded. During this process

---

time steps with zeros as signal are added to the end of the signal. Due to the longer signal, the subsequent FFT provides a higher density of FFT result bins allowing a more exact determination of the frequency. However, the FFT spectra shown in section 5 are not zero-padded to avoid possible amplitude changes.

Additional to the FFTs, the first 200  $\mu\text{s}$  of some beam pulses are analysed using continuous wavelet transformation. Wavelet coefficients  $C_{a,b}$  are calculated using equation 3.22 determining the similarity between a wavelet function  $\Psi$  and the velocity signal  $v(t)$  scanned over scales  $a$  (frequency) and translational values  $b$  (time) of interest.

$$C_{a,b} = \frac{1}{\sqrt{a}} \cdot \int v(t) \cdot \Psi\left(\frac{t-b}{a}\right) dt \quad 3.22$$

As wavelet function a Morlet wavelet [108,109] is chosen which is composed from a Gaussian window and an exponential as defined in equation 3.23.

$$\Psi(x) = \pi^{-\frac{1}{4}} \cdot \cos(kx) \cdot e^{-\frac{x^2}{2}} \quad 3.23$$

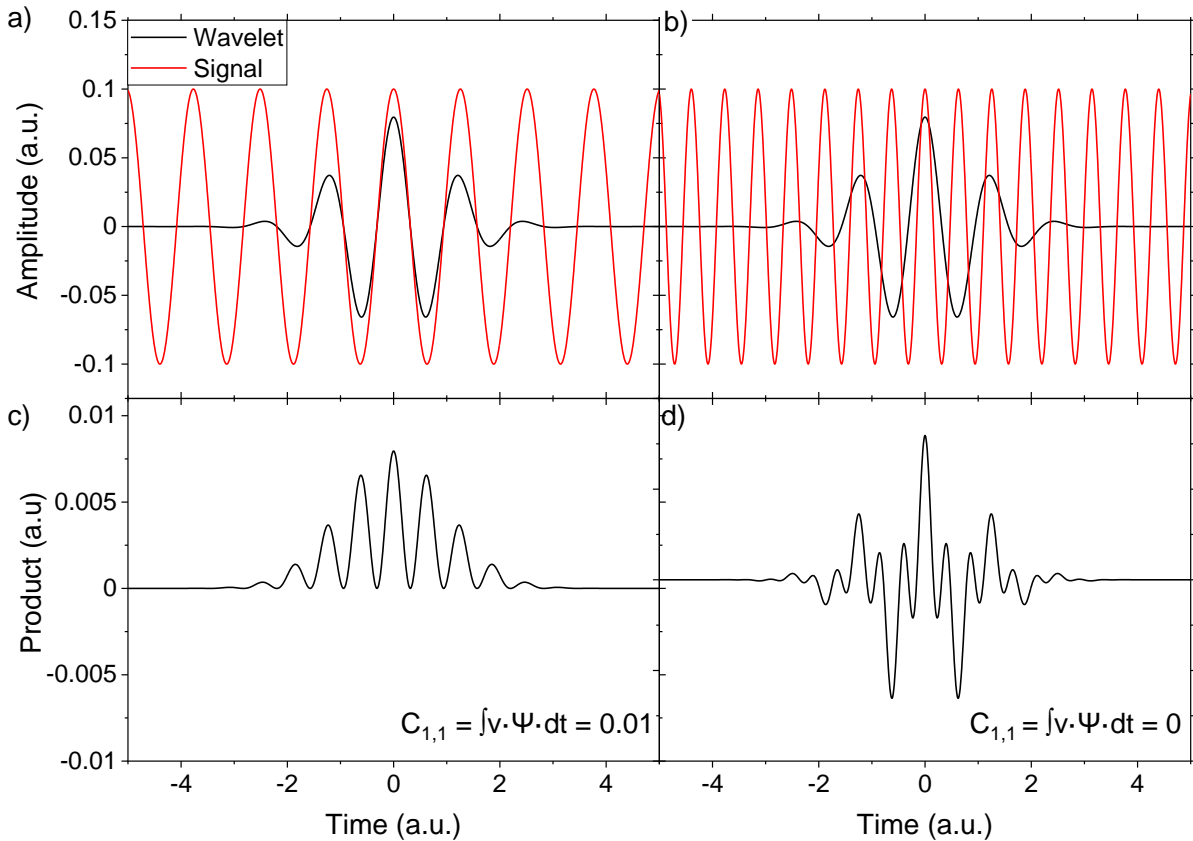


Figure 3.13: Illustration of determination of wavelet coefficients. (Top) Morlet wavelet function with  $k = 5$ ,  $a = 1$  and  $b = 1$  and a sinusoidal signal generated with a) fitting and b) non-fitting frequency. Product of the wavelet function and the signal with c) fitting and d) not-fitting frequency. The product is integrated leading to a positive wavelet coefficient for the fitting frequency and a wavelet coefficient of 0 for the non-fitting frequency.

The wave number  $k$  trades between high time resolution for low  $k$  and high frequency resolution for high  $k$ . A representative Morlet wavelet is illustrated in Figure 3.13 a) and b) together with a generated sinusoidal signal for the case of a) fitting frequency and b) non-fitting frequency. Figure 3.13 c) and d) show the product of wavelet function and signal as done in equation 3.22. If the frequency fits as in Figure 3.13 a), the product is consistently positive and the integration of the product thus gives a positive wavelet coefficient. For the case of a non-fitting frequency as in Figure 3.13 b), the product alternates between positive and negative values and the integration results in a wavelet coefficient of 0. By alternating  $a$  and  $b$ , the wavelet function is stretched and shifted, and the signal is scanned at different times and frequencies. A wavelet coefficient matrix is obtained generating a time resolved frequency analysis. This allows the investigation of rapidly damped signals that are otherwise not visible in the FFTs.

Due to limited recording capacities of the LDV, the high time resolution required to observe transversal stress waves forces a shorter recording time and thus a worse frequency resolution. As the signal of the transversal stress waves is close to or beyond the detection limit of the used set-up, a higher frequency resolution is preferred for most samples to distinguish between different bending peaks. However, the high temporal resolution is kept for an isotropic graphite sample (Section 5.3) which has only one peak in the FFT signal and thus, the required accuracy for the frequency resolution is obtained by zero-padding of the signal.

### 3.4.4 Finite element method simulations of ion beam impacted discs

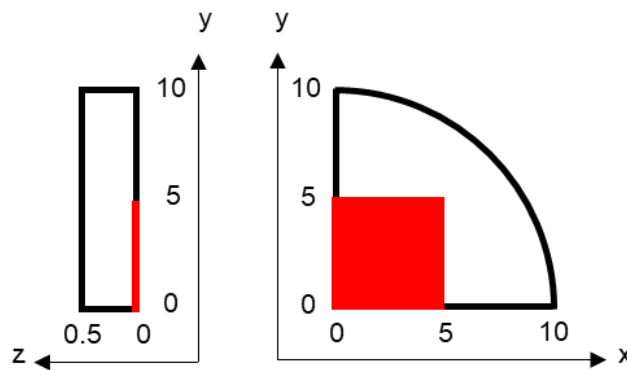


Figure 3.14: Schematic drawing in side and front view of a quarter of a simulated target disc with the plane of the disc oriented in x- and y-direction and the thickness in z-direction. All units are in mm. Note that the z-direction is not drawn to scale for better view. The quadratic beam spot is marked in red.

To benchmark the results of the LDV measurements, simulations with the finite element method (FEM) code ANSYS 2019 R2 release [110] are conducted. For the samples exposed to a quadratic beam spot, a quarter of the disc is simulated using the properties given in Table 2.1 to Table 2.5. A schematic drawing of sample geometry and orientation is shown in Figure 3.14. For samples with a circular beam spot, only a sample segment of 1 degree is simulated with circular symmetry, allowing a larger reduction of computing time. A mesh with element sizes of 0.5 mm in x- and y-direction and 0.05 mm in z-direction was used (Figure 3.15). Convergence of the solution was tested by changing the element size in both directions and securing no significant changes of the obtained results.

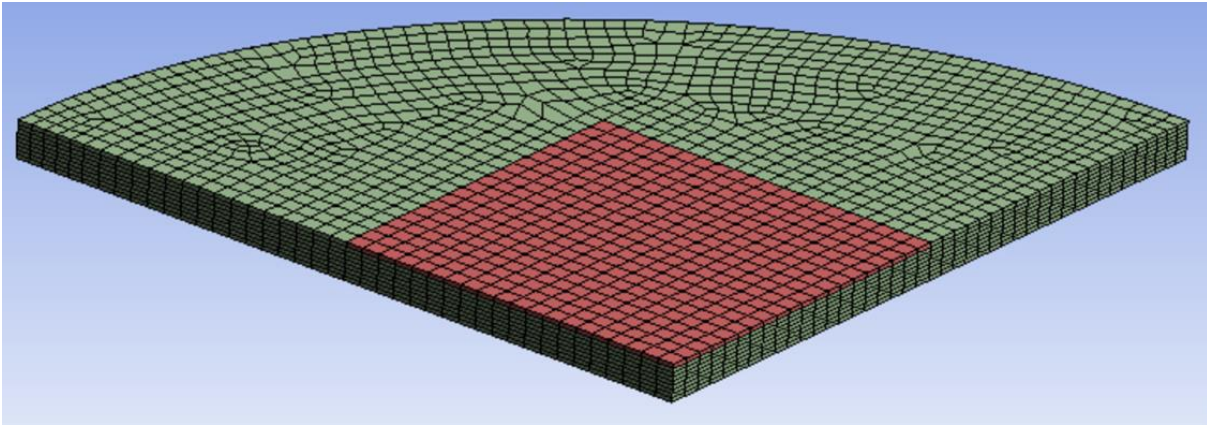


Figure 3.15: Typical mesh used in the Finite element method solver Ansys for a sample with 2 cm diameter and 0.5 mm thickness with a radial element size of 0.5 mm and an axial size of 0.05 mm. The beam spot where the energy is deposited is marked in red and is  $\sim 1/10$ th of the sample thickness.

Since the main focus of this work lies on the frequencies of the discs, modal analysis is used to deduce the frequencies independent of the beam conditions. Transient thermal and mechanical analysis is performed to determine the preferred bending mode and the amplitude of the vibration. To do this, the energy loss of the ions is simplified by depositing the total kinetic energy across the penetration depth resulting in a constant heat generation of some  $\text{MW}/\text{cm}^3$  depending on the average pulse intensity in the irradiated volume for the pulse duration of  $100 \mu\text{s}$ . The simulations were conducted with different time steps. The results shown were performed with a time step of  $5 \mu\text{s}$  for which the results converged. The results of both the modal analysis and the transient thermal and transient mechanical simulations were verified by comparison with the calculations shown in chapter 3.4.2 and the temperature rise calculated by neglecting heat conduction. To simulate the effects of beam-induced material degradation, simulations are also conducted for samples with increased Young's moduli and reduced thermal conductivities [8] in the irradiated volume.

---

## 4 Post-irradiation analysis of structural and mechanical properties

---

This chapter summarizes the results of the post-irradiation experiments. Beam-induced structural changes are analysed by Raman spectroscopy (Section 4.1). The changes of mechanical properties measured both by nanoindentation (Section 4.2) and nanoimpact (Sections 4.3 and 4.4) are shown and correlated to the structural modifications.

---

### 4.1 Beam-induced structural modifications studied by Raman spectroscopy

---

The irradiation of isotropic polycrystalline graphite with 4.8 MeV/u Au and U ions results in pronounced changes within the Raman spectra compared to the spectra of pristine samples (Figure 3.6). The development of the spectra with increasing 4.8 MeV/u Au ion fluence is shown in Figure 4.1 a). The spectra are normalized to the G band. A broadening of the G band is observed with increasing fluence. The most obvious change in the spectra is the increase of the D band due to a higher defect concentration and smaller crystallite sizes according to equation 3.1. The 2D band decreases as well, suggesting a reduction of the length of the continuous graphene layers. Furthermore, the D' band, while easily observable in the pristine sample as shoulder of the G band, is covered by the broadening of the G band. Also, the intensities of the D3 and D4 bands are increasing significantly resulting in the large shoulder at wave numbers of  $\sim 1250 \text{ cm}^{-1}$  and the rise of the valley between D and G band. It should be noted, that the spectra of samples irradiated with ions with high-energy loss approach at high fluences the spectra of the glassy carbon grade Sigradur K, shown on top of Figure 4.1.

For isotropic graphite irradiated with ions with lower energy losses the changes in the Raman spectra are smaller (Figure 4.1 b)). While the ratio of the D band to the G band

is still significantly increasing with increasing ion fluence, the changes of the D', D3 and D4 band are much smaller.

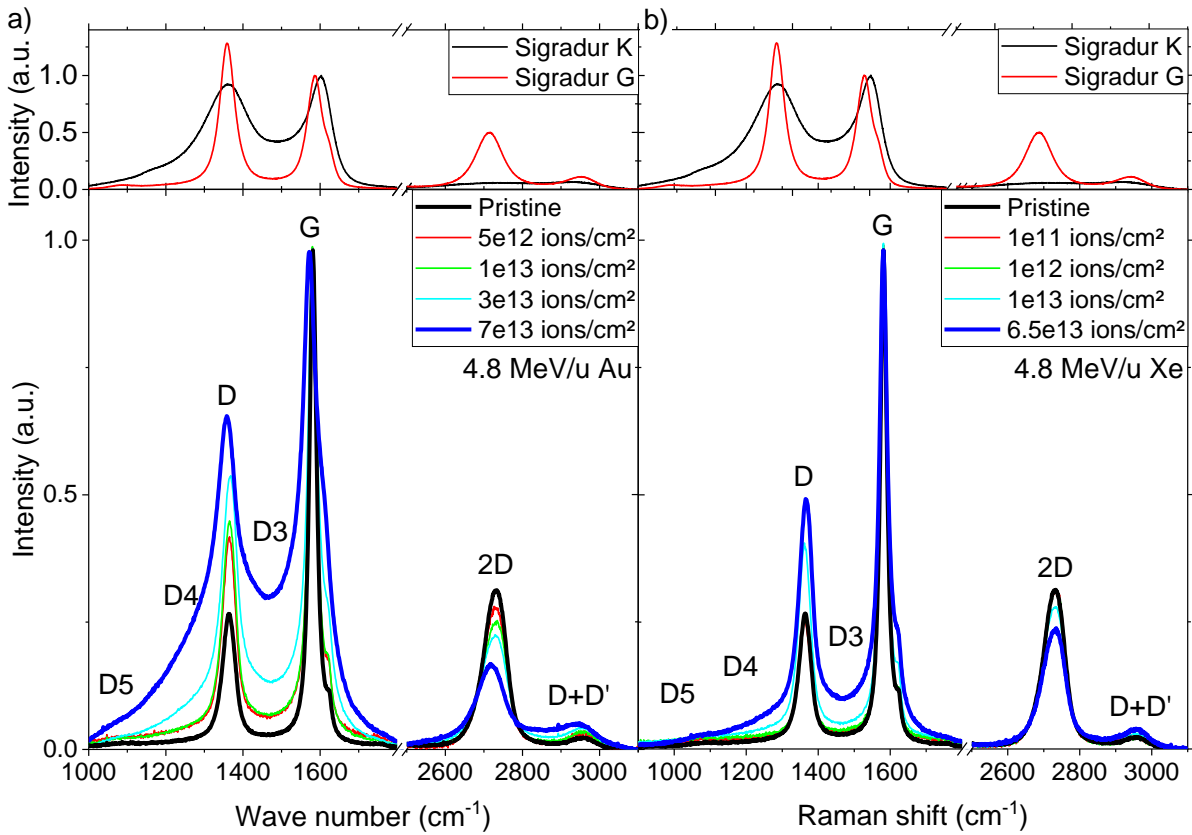


Figure 4.1: Raman spectra (top) of pristine glassy carbon grades Sigradur G and K and (bottom) of isotropic R6650 graphite irradiated with different fluences of 4.8 MeV/u Au ions (left) and 4.8 MeV/u Xe ions (right). In all spectra the intensities are normalized to the G band.

The fluence evolution of the intensities of the D, D3 and 2D band (normalized to the G band) and the FWHM of the G band for irradiations with ions ranging from carbon to uranium is shown in Figure 4.2. The measured pristine values and the values obtained for Sigradur K and G are included as yellow, light grey and dark grey bands, respectively. Error bars and width of the coloured bands in these and all subsequent graphs (unless specifically mentioned otherwise) represent the 95 % confidence interval of the measured parameters and are estimated to be 20 % for the fluences uncertainty. As already indicated in Figure 4.1, there is a clear tendency that all values develop towards the values of Sigradur K. The irradiation damage obviously results in defects within the graphite planes leading to smaller crystallite sizes and non-six-membered rings causing curved graphite planes [51]. Especially the  $I_{D3}/I_G$  and  $I_{2D}/I_G$  ratios of Sigradur G show a different behaviour indicating that the characteristic pores

of a size of ~5 nm are not generated at the investigated fluences. The damage clearly depends on the ion species and their energy loss. It is largest for irradiations with 4.8 MeV/u U ions and less pronounced for the lighter ions. Minimum damage is observed for samples exposed to carbon and calcium ions. Within the experimental uncertainties, the carbon and most of the calcium data are similar to the pristine values. The  $I_{D3}/I_G$  ratio at the highest observed 4.8 MeV/u U ion fluence is larger than the ratio of glassy carbon which might indicate additional amorphous carbon generated by the ion irradiation.

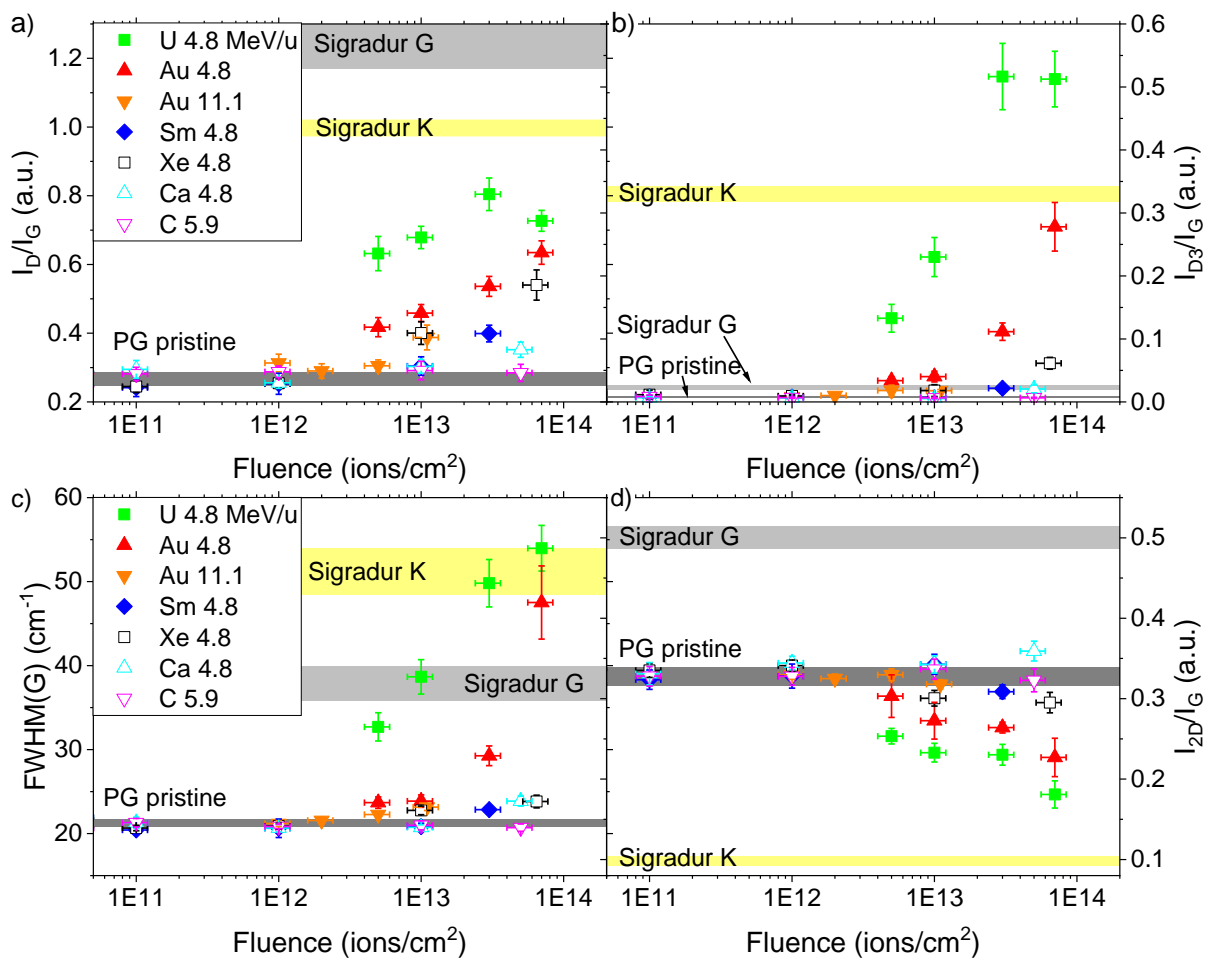


Figure 4.2: Intensity of a) D band, b) D3 band and d) 2D band normalized to the G band and c) Full width half maximum of the G band for isotropic R6650 graphite as a function of the ion fluence. Yellow and dark and light grey bands indicate the respective values of pristine R6650 and glassy carbon Sigradur K and G.

It was shown by Prosvetov et al. [6,8] that damage in flexible graphite scales mainly with the nuclear energy loss and thus appears close to the stopping range of the ions, while changes in isotropic graphite are more homogenous across the entire ion range.

---

The difference was attributed to the different microstructure between well-oriented flexible graphite and randomly oriented isotropic graphite. The higher order of flexible graphite leads to a higher electrical conductivity. The electrical charge induced by the electronic energy loss can be distributed rapidly within the material, preventing damage generation. To test this hypothesis, highly oriented pyrolytic graphite (HOPG) is included in this investigation. It has an even more well-oriented structure and, using adhesive tape, few layers can be removed allowing the determination of the depth dependence without cutting or breaking of samples, which could generate new defects. After each Raman measurements, a thin layer is removed from the HOPG sample surface and the remaining thickness of the sample is measured with a profilometer. This process works well for pristine and low fluence samples. For samples irradiated to high ion fluences, however, after removal of the first layers, further Raman measurement for the depth dependence is not possible because following layers tend to be removed by the adhesive tape in a single step. It is assumed that ion irradiation results in cross linking of the layers. A stronger connection between the layers in the region of the highest nuclear energy loss prevents its separation while the layers in the underlying pristine substrate remain easily separable.

Due to this effect, Figure 4.3 shows the development of the  $I_D/I_G$  ratio of HOPG irradiated with a fluence of  $1 \times 10^{12}$  ions/cm<sup>2</sup> of 4.8 MeV/u Au ions. At this fluence the layers could still be removed in rather small steps. As observed for flexible graphite [6,8], the  $I_D/I_G$  ratio follows the nuclear energy loss with the largest D band intensity at the end of the ion range. However, it can be seen that the  $I_D/I_G$  ratio is already at pristine values at a depth of 45  $\mu\text{m}$  while the penetration depth obtained by SRIM simulations [41] is 48  $\mu\text{m}$ . SRIM assumes an amorphous structure for the calculations. In case of oriented graphite the energy loss is higher perpendicular to the planes [111,112] leading to a lower penetration depth. Furthermore, the exfoliation process could also be responsible for a stretching of the distance between the layers and hence to a slightly underestimated depth.

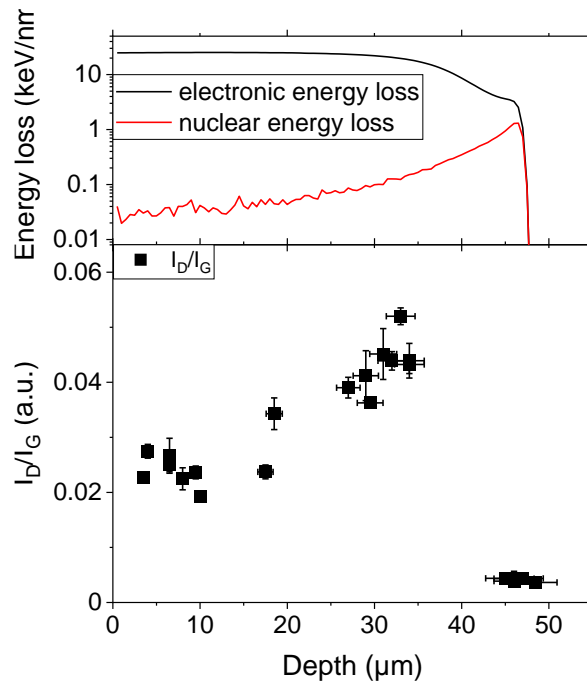


Figure 4.3: (Top) Semi-log presentation of depth dependence of electronic and nuclear energy loss of 4.8 MeV/u Au ions in carbon with a density of 2.25 g/cm<sup>3</sup> calculated using SRIM 2013 code [41]. (Bottom) Ratio of the intensity of the D band to the G band of HOPG irradiated with 4.8 MeV/u Au ions to a fluence of  $1 \times 10^{12}$  ions/cm<sup>2</sup>.

## 4.2 Beam-induced changes of quasi-static mechanical properties

The quasi-static properties obtained by nano- and microindentation are summarized in this section. The well-established method by Oliver and Pharr [13,14] allows the determination of the hardness and the Young's modulus. Especially the Young's modulus is an important material parameter for calculations and simulations of both static and dynamical mechanical effects. The absolute values of the investigated materials are presented in section 4.2.1. Section 4.2.2 presents the results of isotropic graphite, with the main focus on the influence of different energy losses and of the microstructure. Section 4.2.3 investigates CFCs with special attention to the influence of the fibres on the radiation resistance by separate observations of the fibres and the graphite matrix. The results of well-oriented graphite are shown in section 4.2.4, consisting of indentation of flexible graphite and highly oriented pyrolytic graphite which is exfoliated to investigate the depth development of the mechanical parameters.

Finally, the materials are compared in section 4.2.5 and ion track radii deduced from the fluence evolution of indentation measurements are shown in section 4.2.6.

#### 4.2.1 Pristine materials

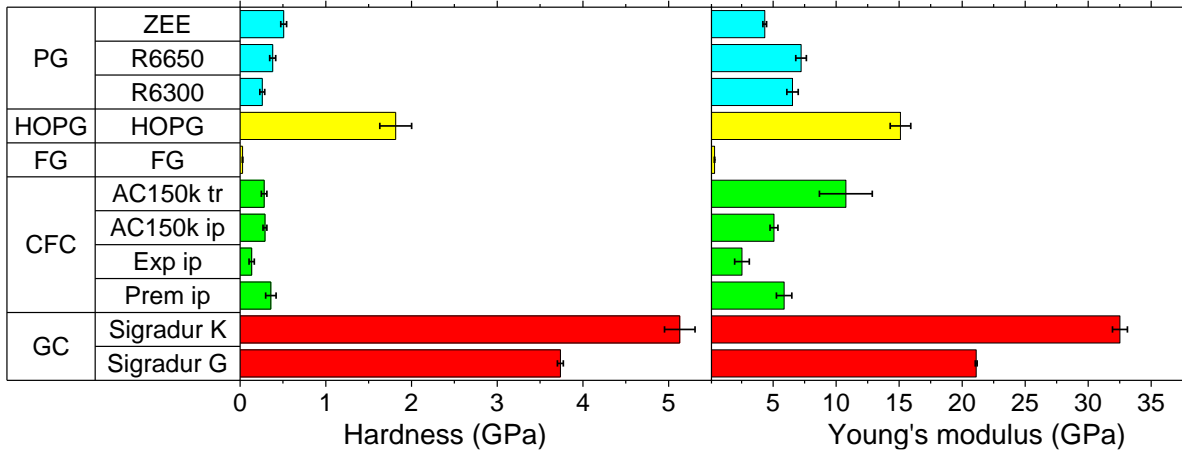


Figure 4.4: Hardness and Young's modulus of pristine graphitic materials obtained by microindentation measurements to a depth of 10  $\mu\text{m}$ .

Results of microindentation experiments conducted on pristine samples are summarized in Figure 4.4. Compared to the literature values from the data sheets [18-20,22,23,30], most of the obtained Young's moduli are slightly underestimated. The investigated polycrystalline graphite grades show a grain size dependence of the hardness with the largest hardness obtained for POCO ZEE which has the lowest average grain size of  $\sim 1 \mu\text{m}$  and the lowest hardness for SGL R6300 which has the largest grain size of  $\sim 20 \mu\text{m}$ . The Young's modulus of the two SGL grades is similar, while the value for ZEE which has the highest graphitization is slightly lower. Hardness and Young's modulus of the investigated CFC grades are in a similar order. AC150k and SGL Premium have very similar values in the in-plane orientation while values obtained for SGL Experimental Premium are approximately half. Both hardness and Young's modulus of flexible graphite is about an order of magnitude lower than the values of the PG and CFC grades. As the graphitic planes have no interconnection or grain boundaries in FG, the planes can easily slide past each other and the low density leads to easier deformation resulting in poor mechanical properties. On the other hand, due to its high density, HOPG is very difficult to compress plastically perpendicular to the planes leading to a high hardness. Glassy carbon has an at least one order of

magnitude higher hardness compared to the PG and CFC grades and a considerably higher Young's modulus. The disordered structure prevents sliding of the planes resulting in a sturdy, brittle structure.

#### 4.2.2 Isotropic polycrystalline graphite

Typical results obtained by microindentation of the isotropic graphite grade SGL R6650 are shown in Figure 4.5. Graphite exhibits a very elastic response with more than 50 % of the maximum depth recovered after releasing the force. Visible inspection of the remaining indent is thus very difficult with the in-built optical microscope, since most of the indent recovers and the existing roughness prevents easy detection with a SEM. However, since pile-up is expected only for very plastic materials and sink-in is corrected by the Oliver and Pharr method, the measured results are expected to be valid.

The sample irradiated with 4.8 MeV/u Au ions to a fluence of  $7 \times 10^{13}$  ions/cm<sup>2</sup> requires about 5-times the load to achieve the same maximum depth. Additionally, a lower slope of the initial unloading curve and a lower contact depth is obtained for the irradiated sample. Using the analysis method by Oliver and Pharr [13,14] reveals that the irradiation leads to a significantly increased hardness and Young's modulus.

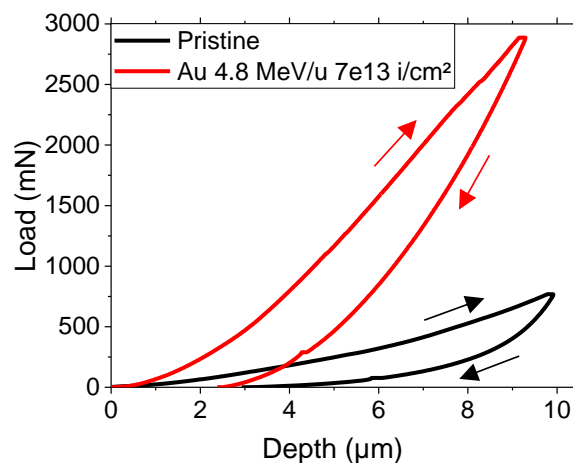


Figure 4.5: Depth signal of an indentation measurement for isotropic R6650 graphite, both pristine and irradiated with 4.8 MeV/u Au ions to a fluence of  $7 \times 10^{13}$  ions/cm<sup>2</sup>.

The development of hardness and Young's modulus with increasing fluence of various ions ranging from carbon to uranium are shown in Figure 4.6 a) and b). The relative

---

increase of hardness and Young's modulus (Figure 4.6) and most of the following figures were obtained from indentation measurements. This was done to avoid possible influences (e.g., indentation size effects and others) that might prevent accurate measurements of the Young's modulus but still allow a relative comparison between the effects of different ion beams. A large increase of up to 10-times the pristine hardness and 3-times the pristine Young's modulus can be seen for the samples irradiated with 4.8 MeV/u Au and U ions. The relative difference of the glassy carbon grades Sigradur K and G to SGL R6650 are marked by yellow and light grey bands. Both the hardness and the Young's modulus of the samples irradiated with the heaviest ions approach these ratios, indicating a phase transformation to a disordered structure as observed in the results of Raman spectroscopy (Figure 4.2) and thermal properties [6,8]. Compared to 4.8 MeV/u Au and U ions, the changes induced by the lighter ion species are much smaller which is obvious when presenting the data as a function of dose (Figure 4.6 c) and d)) which is the product of energy loss and fluence. Although small, they are significant and increase up to 180 % of the respective pristine value of hardness and Young's modulus. The Young's modulus is more sensitive than the hardness to irradiation for all the investigated ions shown by a faster saturation at the highest investigated fluences. This can be attributed to a higher sensitivity of the Young's modulus to stress in the material induced by the ion tracks.

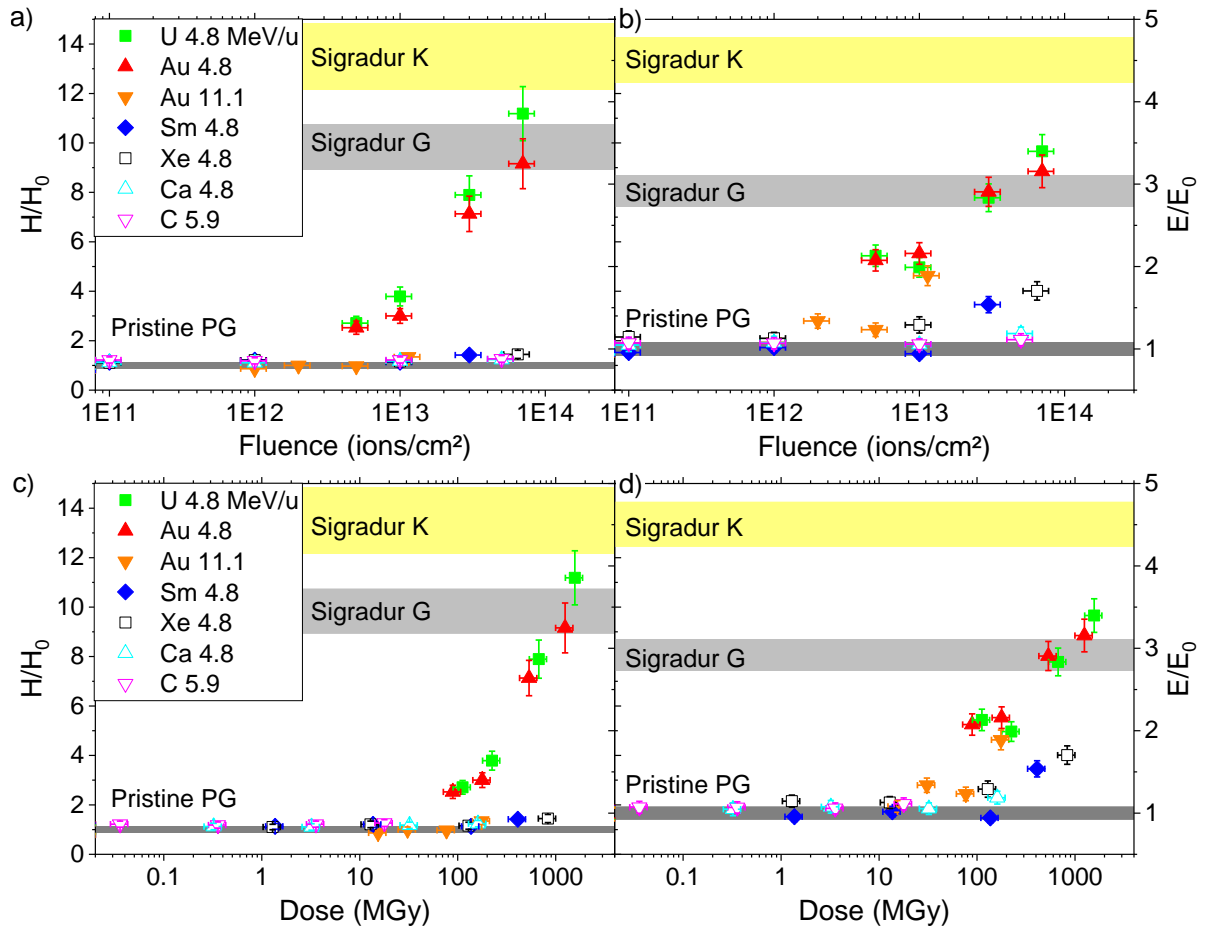


Figure 4.6: Relative change of hardness (left) and Young's modulus (right) of isotropic R6650 graphite as a function of ion fluence (top) and dose (bottom). Yellow and dark and light grey bands indicate respective the values of pristine R6650 and glassy carbon Sigradur K and G.

Figure 4.7 shows the relative changes of hardness and Young's modulus as a function of the surface energy loss for all ion species at a fluence of  $1 \times 10^{13}$  ions/cm<sup>2</sup>. This fluence is selected because data are available for all ion species. The hardness data suggests that the transformation to a disordered structure similar to glassy carbon requires a critical energy loss of at least 18 keV/nm. For U and Au ions with an energy loss above 18 keV/nm the changes of both the hardness and the Young's modulus (Figure 4.6 c) and d)) follow the same trend with dose, whereas ions below 18 keV/nm (C-Au) follow another trend. This indicates two different damage mechanisms with a critical energy loss threshold. For the Young's modulus, the data for the irradiation with 11.1 MeV/u Au ions is surprisingly high (compared to the hardness data). The specific energy of 11.1 MeV/u Au ions is above the Bragg maximum and the energy loss thus increases with increasing penetration depth. It is assumed that the phase

transformation, occurring deeper in the material, induces stress that might influence the Young's modulus at the surface more than the hardness.

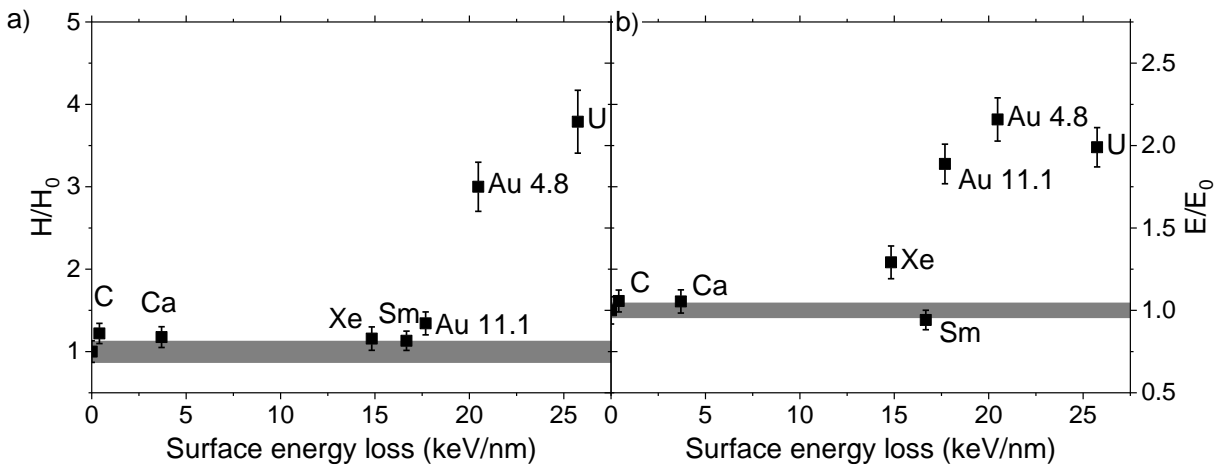


Figure 4.7: Relative change of a) hardness and b) Young's modulus of isotropic R6650 graphite as a function of surface energy loss calculated with SRIM 2013 code [41] at a fluence of  $1 \times 10^{13}$  ions/cm<sup>2</sup>. The dark grey band indicates the values of pristine SGL R6650.

Figure 4.8 compares hardness and Young's modulus changes after 4.8 MeV/u Au ion of three isotropic polycrystalline graphite grades. The increases are largest in SGL R6650. Compared to SGL R6300 the main difference is a smaller average grain size ( $\sim 7 \mu\text{m}$  compared to  $\sim 20 \mu\text{m}$ ) suggesting that the grain boundaries play an important role for the phase transformation. This assumption is supported by measurements of HOPG (Chapter 4.2.4) where swift heavy ion irradiation of the well-aligned graphite layers with very few grain boundaries results in very low changes of hardness and Young's modulus. POCO ZEE has an even lower average grain size of  $\sim 1 \mu\text{m}$ . It is better graphitized than the SGL grades and is produced without added binder resulting in a different structure of the grain boundaries. This obviously leads to a smaller increase of the hardness while the increase of the Young's modulus is similar to the two SGL grades.

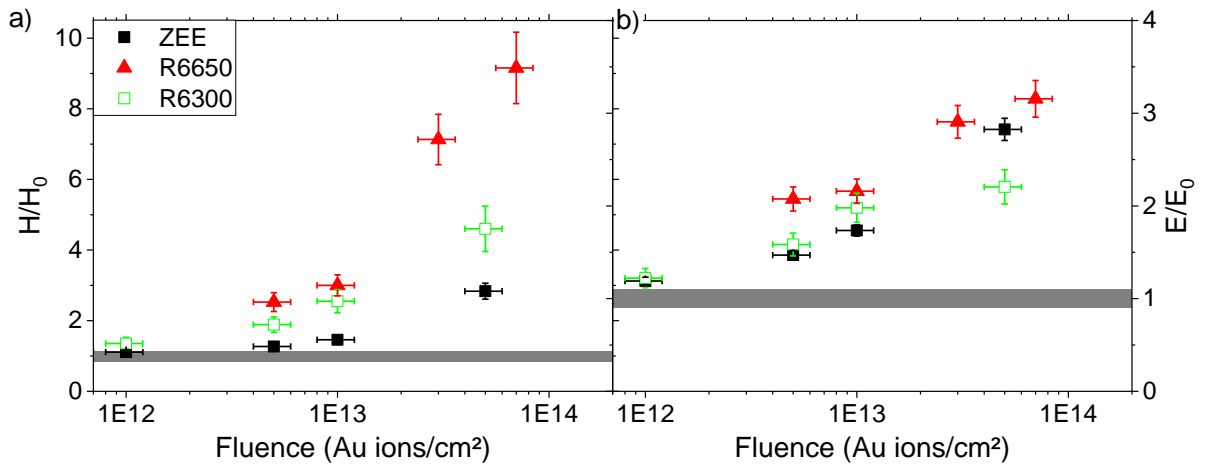


Figure 4.8: Relative change of a) hardness and b) Young's modulus for the isotropic graphite grades R6650, R6300 and ZEE as a function the 4.8 MeV/u Au ion fluence. The dark grey band indicates the values of the pristine graphite grades (the width of the band corresponds to the largest error of the three grades).

#### 4.2.3 Carbon fibre reinforced carbon

Carbon fibre reinforced carbons are designed to improve thermal and/or mechanical properties of graphite. The CFCs investigated in this work have a two-dimensional structure (cf. Figure 2.2) resulting in anisotropic properties. According to literature [24,113], the mechanical properties can vary by an order of magnitude depending on the direction. During indentation experiments, however, the load is not only transmitted in the direction of the indentation but also perpendicular to it. Hence, the measured Young's modulus of  $10.8 \pm 2.1$  GPa and  $5.1 \pm 0.3$  GPa of the transversal and in-plane orientation is considerably lower than the literature values of 62 GPa [114,115] to 77 GPa [24,113] given for measurements perpendicular to the fibres. The measured values are closer to the literature value measured parallel to the fibres of AC150k of 5 GPa [24,113]. While the hardness is very similar in both directions, the Young's modulus of the transversal direction is almost twice the value measured in the in-plane direction. Due to the combination of fibres and matrix, the scattering of both hardness and Young's modulus becomes higher. Owing to the different production process compared to isotropic graphite, the amount and size of pores is higher, which is also indicated by the lower density, resulting in additional scattering of the properties.

After irradiation with several ion species, similar effects as observed for isotropic graphite are also observed in CFC as shown in Figure 4.9 to Figure 4.11. Large changes occur for irradiations with ions of high-energy loss. Due to the lower density, the surface energy loss of CFC is slightly lower than for isotropic graphite. However, since the lower density and thus the lower energy loss is a mean value including graphite grains and the larger fraction of pores the actual energy loss within the graphitic grains should be similar. For ions with a lower energy loss only small increases of the mechanical parameters are obtained. As observed in isotropic graphite, an energy loss threshold is required for a phase transformation to a disordered structure similar to glassy carbon. The Young's modulus is more sensitive than the hardness in both orientations of CFC visible by the faster rise at lower fluences.

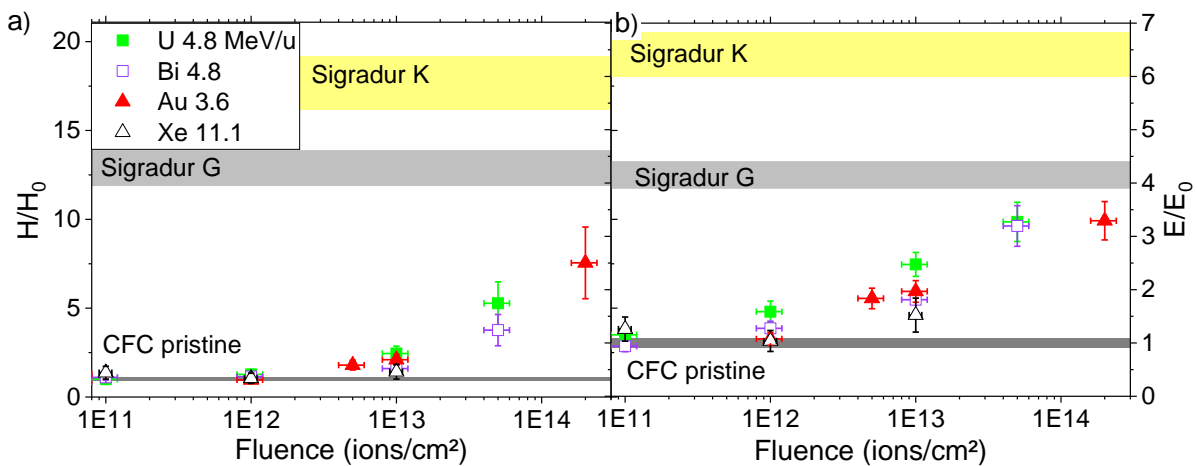


Figure 4.9: Relative change of a) hardness and b) Young's modulus of the in-plane orientation of the carbon fibre reinforced carbon grade AC150k as a function of ion fluence. Yellow, dark and light grey bands indicate the values of unirradiated AC150k and glassy carbon Sigradur K and G, respectively.

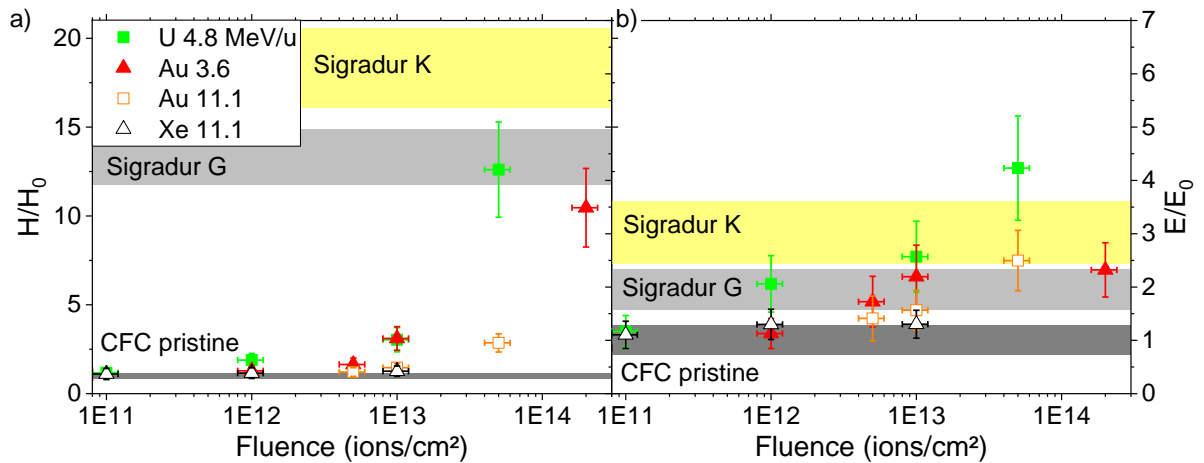


Figure 4.10: Relative change of a) hardness and b) Young's modulus of the transversal orientation of the carbon fibre reinforced carbon grade AC150k as a function of the ion fluence. Yellow, dark and light grey bands indicate the values of unirradiated AC150k and Sigradur K and G, respectively.

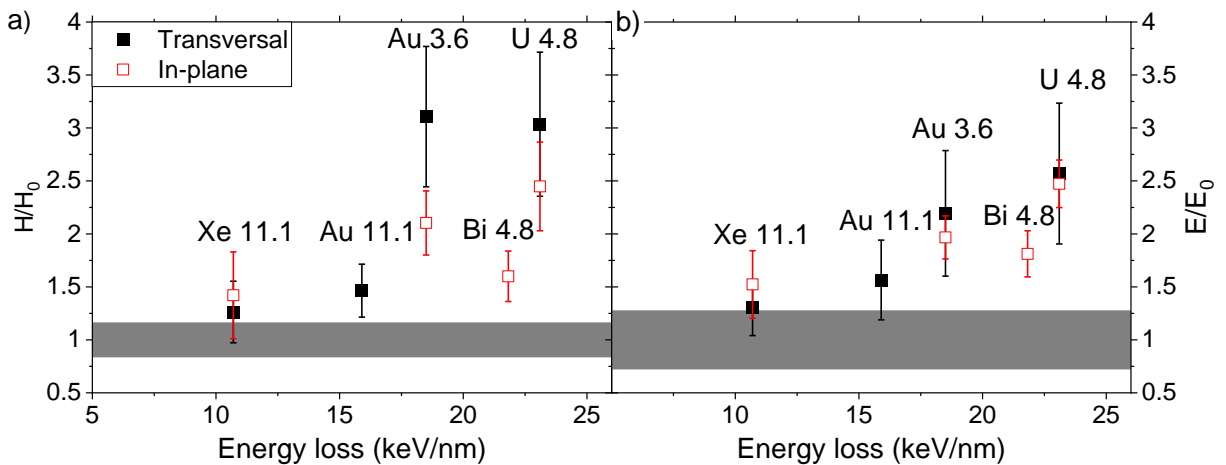


Figure 4.11: Relative change of a) hardness and b) Young's modulus of the carbon fibre reinforced carbon grade AC150k as a function of the surface energy loss. The dark grey band indicates the values of pristine AC150k (the width of the band corresponds to the largest error of the two orientations).

Comparing the two directions, the increase of the hardness is larger in the transversal orientation. The relative increase of the Young's modulus is similar in both orientations despite the different pristine values. From these measurements it is not clear if the different changes of the hardness are caused by the fibres or the surrounding matrix. To probe the matrix and the fibres separately, nanoindentation experiments are conducted in combination with optical microscopy as illustrated in Figure 4.12. This is only possible in the in-plane orientation as the fibres in the transversal orientation mostly do not lie in the plane of the cut sample, and fibre cross sections cannot be

identified by optical microscopy. The indentation measurements are performed along a line starting from the matrix onto a fibre. The indents could only be detected by optical microscopy in the matrix by comparing an image before the measurement with an image after the measurement, due to the roughness remaining after the lapping of the samples. In the fibres, no indents are visible due their high elasticity. The indents could be attributed to the locations in the matrix, and based on the known spacing of the line scan, the exact location on the fibre could be determined. In Figure 4.12 hardness and Young's modulus values attributed to the fibre are marked in red and values attributed to the matrix are marked in black. At least three similar locations are investigated for each sample.

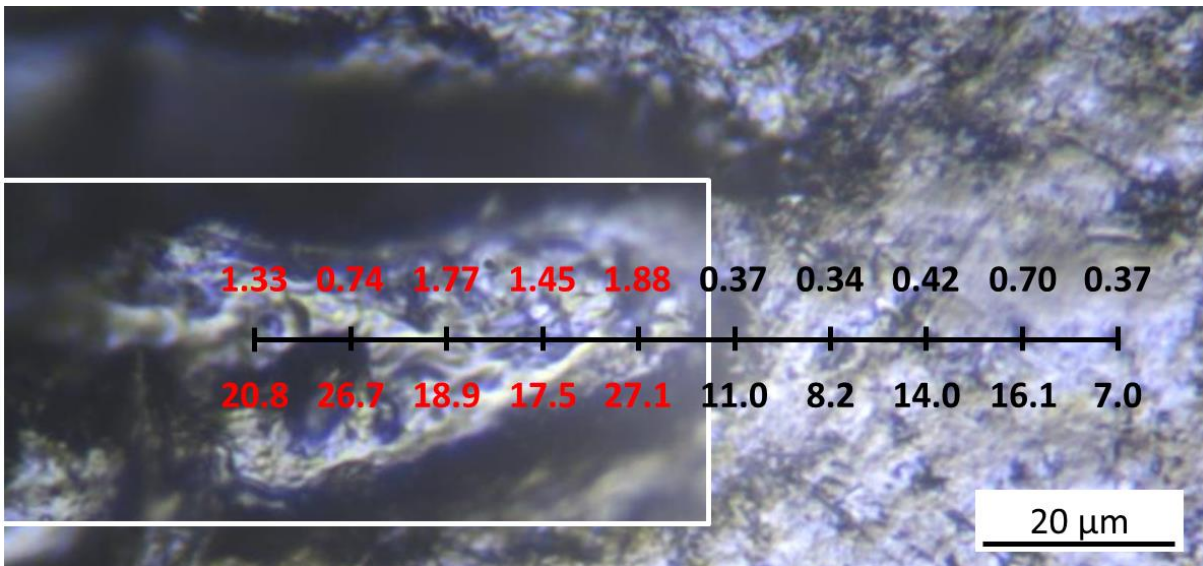


Figure 4.12: Targeted indentation of a fibre and the matrix of the CFC grade AC150k irradiated with 4.8 MeV/u U ions to a fluence of  $1 \times 10^{12}$  ions/cm<sup>2</sup>. The figure is composed of two optical microscope images required to focus on the matrix and the fibre (within the white frame) positioned deeper within a pore. Hardness (above the line) and Young's modulus (beyond the line) values in GPa attributed to the fibres are marked in red, values attributed to the matrix are marked in black.

The obtained hardness and Young's modulus values for the fibres are significantly higher than for the graphite matrix and on a similar level as HOPG (Table 4.1). The scattering relative to the measured values is smaller for the fibres. This can be explained by the highly ordered and dense structure of the fibres compared to the lower density of the matrix. Comparing the results of the randomly positioned indents to the results of the targeted indents, it is observed that the latter are dominated by measurements of the matrix with only very few outliers by indents of the fibres.

Table 4.1: Hardness and Young's modulus for the matrix and fibres of the CFC grade AC150k

	Matrix	Fibres
Hardness [GPa]	$0.47 \pm 0.08$	$1.39 \pm 0.26$
Young's modulus [GPa]	$8.5 \pm 1.0$	$13.6 \pm 1.5$

After irradiation with 4.8 MeV/u U ions and 3.6 MeV/u Au ions (Figure 4.13), the relative changes of the hardness and the Young's modulus are similar to the values measured in the randomly positioned indents (Figure 4.9), as expected. Both the matrix and the fibres have a similar increase of the Young's modulus, while the increase of the hardness is higher in the matrix for almost all fluence steps. In the comparison between in-plane and transversal orientation similar effects are observed. The in-plane orientation has a larger increase of the hardness as the transversal orientation where most of the fibres are not in the direction of the targeted indentation. As the randomly positioned indents are larger as the diameter of the fibres, the influence of the matrix is higher in the transversal direction. On the other hand, the Young's modulus shows no difference depending on the indentation direction as matrix and fibres have a similar increase.

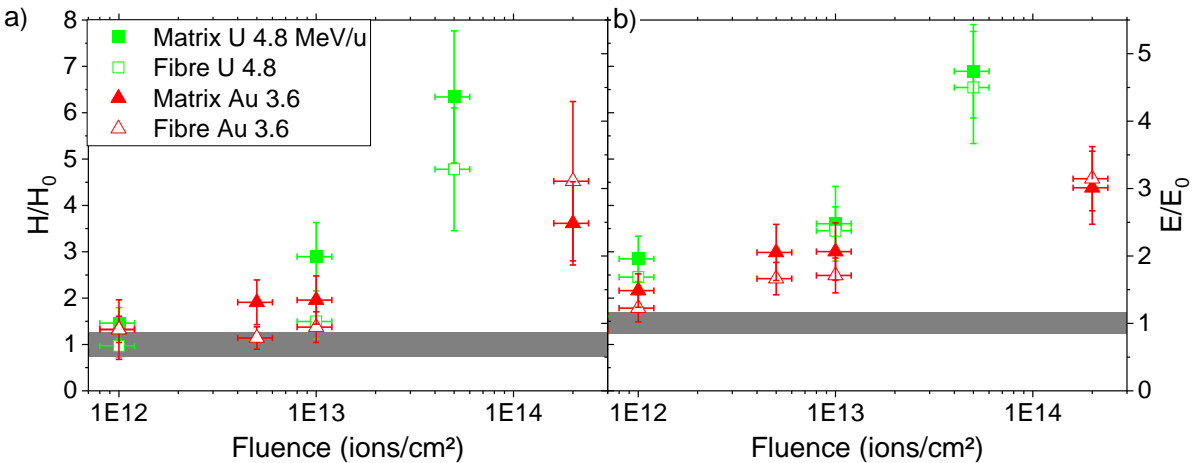


Figure 4.13: Relative change of a) hardness and b) Young's modulus fibres and matrix of the carbon fibre reinforced carbon grade AC150k as a function the ion fluence. The dark grey band indicates the values of the pristine matrix and fibres with the larger respective error.

In Figure 4.14 results of three different CFC grades are compared. Due to the woven structure of the carbon fibre bundles in SGL Premium and Experimental Premium, the measurements highly depend on the location of the measurement. This leads to a higher scattering within the measurements of a sample and amongst the samples compared to AC150k. SGL Premium and Experimental Premium are only distinguished by an additional heating step for Experimental Premium. Both the measured hardness and the Young's modulus of the pristine samples of Experimental Premium is approximately half the values obtained for Premium. The data sheets furthermore show a lower flexural strength for Experimental Premium [22,23]. On the other hand, the additional heat step leads to an increased thermal conductivity indicating a better graphitization [22,23]. After Au ion irradiation, the changes of the hardness are similar for all three different CFC grades. The change of the Young's modulus seems to be highest for Experimental Premium and lowest for Premium.

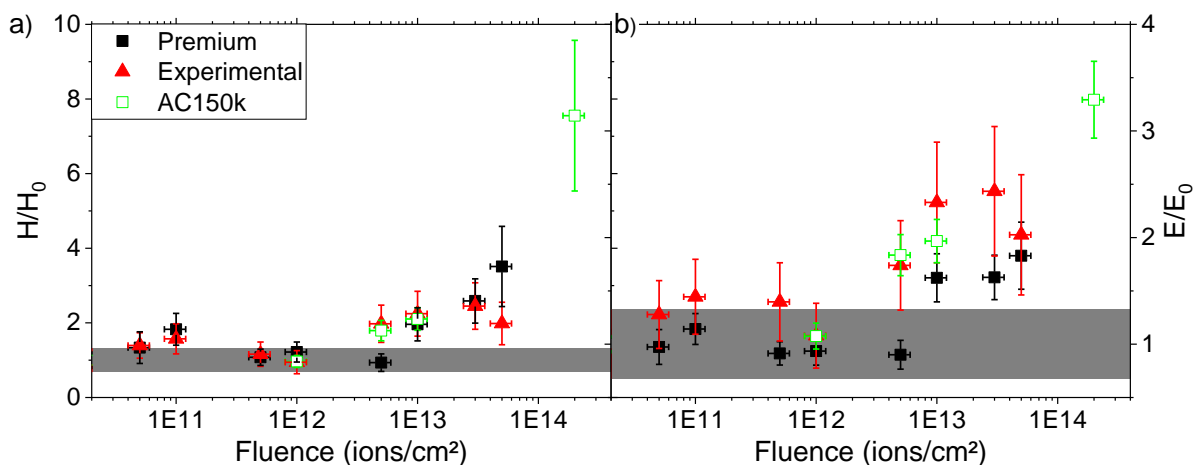


Figure 4.14: Relative change of a) hardness and b) Young's modulus of the in-plane orientation of various carbon fibre reinforced carbon grades (Premium, Experimental Premium and AC150k) as a function of the ion fluence. SGL Premium and Experimental Premium are irradiated with 4.8 MeV/u Au ions and AC150k with 3.6 MeV/u Au ions. The dark grey band indicates the values of the pristine CFC grades (the width of the band corresponds to the largest error of the three grades).

#### 4.2.4 Well-oriented graphite

The changes of hardness and Young's modulus of flexible graphite (FG) and highly oriented pyrolytic graphite (HOPG) are illustrated in Figure 4.15. The irradiation of HOPG results in only small changes of the mechanical parameters. While the ion

beam-induced damage can result in cross linking between the graphitic layers, the main load applied during indentation is perpendicular to these layers whose properties are not significantly changed. Flexible graphite is less well-oriented resulting in the lowest pristine values of density, hardness and Young's modulus of all the investigated graphitic materials (Figure 4.4). Changes induced by 4.8 MeV Au and U ion are significantly larger than for irradiated HOPG, however the obtained absolute values still remain below the pristine values of HOPG.

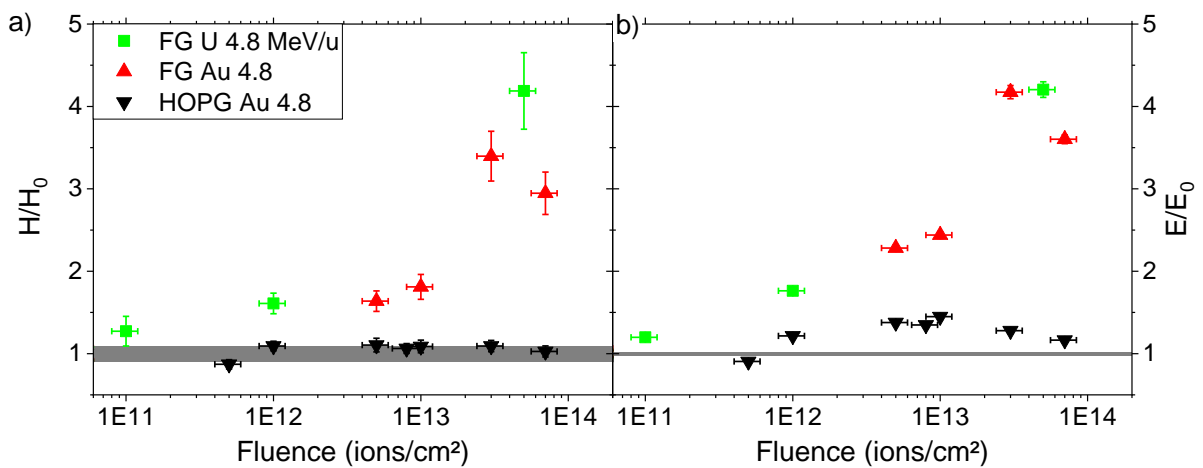


Figure 4.15: Relative change of a) hardness and b) Young's modulus of flexible graphite and highly oriented pyrolytic graphite as a function of ion fluence. The dark grey band indicates the values of pristine FG and HOPG (the width of the band corresponds to the largest error of the two materials).

As shown in Figure 4.3, Raman spectroscopy of HOPG indicates that the I<sub>D</sub>/I<sub>G</sub> ratio follows the nuclear energy loss rather than the electronic energy loss. Nanoindentation is performed at every exfoliation step (Figure 4.16), similar to the Raman measurements. Compared to the measurements of the initial surface of the samples, the exfoliating process generates flakes causing a higher uncertainty of the measurement results. The changes induced by the 4.8 MeV/u Au ions are very low due to the low fluence required for the successful exfoliation process. A small increase can be identified especially for the hardness at depths between 30 and 40 μm where also the highest I<sub>D</sub>/I<sub>G</sub> is observed. However, due to the low ion fluence and the large scattering of the values, the reliability of this observation needs to be confirmed.

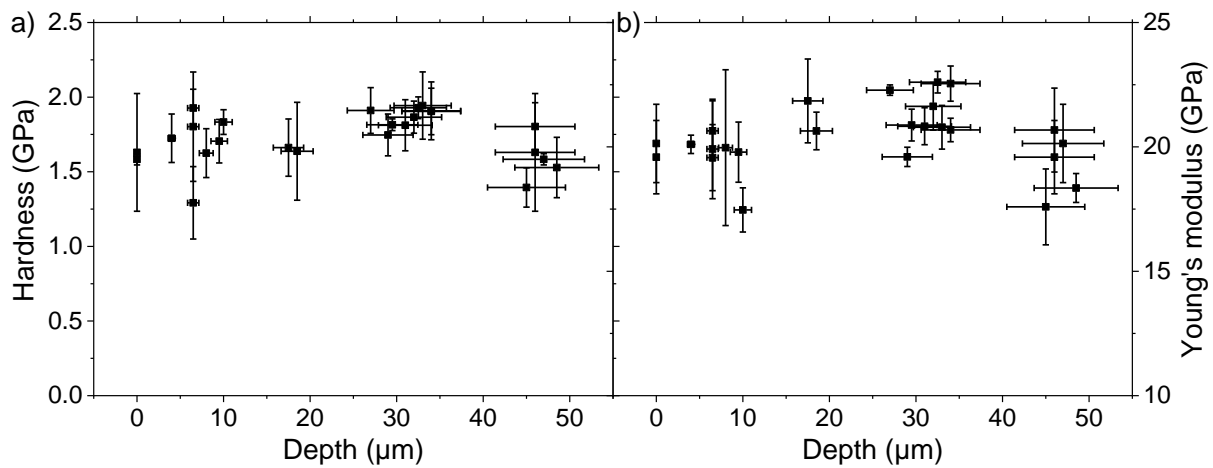


Figure 4.16: Depth dependence of a) hardness and b) Young's modulus of HOPG irradiated with 4.8 MeV/u Au ions to a fluence of  $1 \times 10^{12}$  ions/cm<sup>2</sup>. The uncertainty of the depth is estimated to be 10 %.

#### 4.2.5 Material comparison

The hardness and Young's modulus changes obtained for various graphitic materials after Au ion irradiation are summarized in Figure 4.17. While the hardness of HOPG is almost not changing, large changes up to 1000 % were observed for PG and the transversal orientation of CFC. The in-plane orientation of CFC has a lower increase of the hardness compared to the transversal orientation. In the in-plane orientation the fibres are aligned perpendicular to the direction of indentation. Their density and orientation is more similar to HOPG compared to the matrix, resulting in a smaller hardness change of the fibres than the matrix. This leads to the overall smaller change of the in-plane orientation. Flexible graphite has a smaller increase of the hardness than the other materials except HOPG, but the largest increase of the Young's modulus. This might indicate a different damage mechanism related to milling of the graphitic planes. The Young's modulus changes of both CFC orientations and of PG show the same trend. It is already observed for the targeted indentation of fibres and matrix and of the different PG and CFC grades that the Young's modulus change is less dependent on the microstructure.

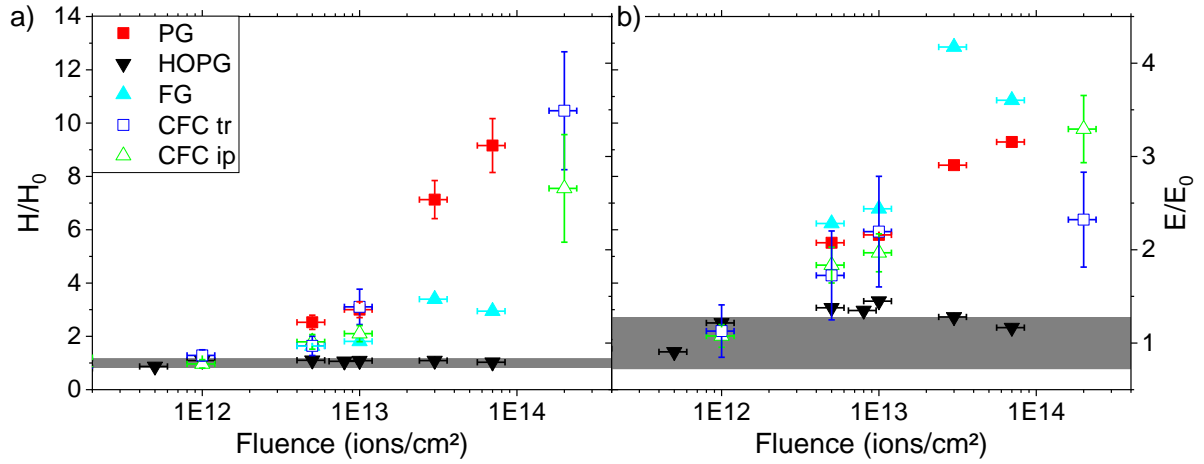


Figure 4.17: Relative change of a) hardness and b) Young's modulus of graphitic materials as a function of fluence of 4.8 MeV/u Au ions for PG (SGL R6650), FG and HOPG and 3.6 MeV/u Au ion fluence for transversal (tr) and in-plane (ip) orientation CFC (Tatsuno Ac150k). The dark grey band indicates the values of the pristine materials (the width of the band corresponds to the largest error of the investigated materials).

#### 4.2.6 Estimation of damage cross section

Typical phenomena induced by swift heavy ions such as track formation are single hit processes. In the low fluence regime where each ion produces an individual damage track the property changes increase linearly with increasing fluence. As soon as tracks start to overlap, the contribution of subsequent ions to property changes is less and less, leading to a sublinear fluence evolution. Once the entire sample is covered with tracks, the properties reach a saturation level.

Mathematically this process can be described by a Poisson's equation (Equation 4.1 [116,117]). Curves fitted to the hardness data ( $H$ ) of R6650 versus ion fluence are shown in Figure 4.18 a).

$$\frac{H}{H_0} = \frac{H_{max}}{H_0} - \left( \frac{H_{max}}{H_0} - 1 \right) e^{-\sigma\Phi} \quad 4.1$$

$H_{max}$  and  $H_0$  are the saturated and pristine hardness, respectively,  $\sigma$  is the damage cross section induced by a single ion and  $\Phi$  is the ion fluence. To deduce the damage cross section responsible for the beam-induced change of the Young's modulus, equation 4.1 is applied as well, but the hardness parameters are replaced by the

respective Young's moduli values ( $E$ ,  $E_{max}$  and  $E_0$ ). The respective fits are shown in Figure 4.18 b).

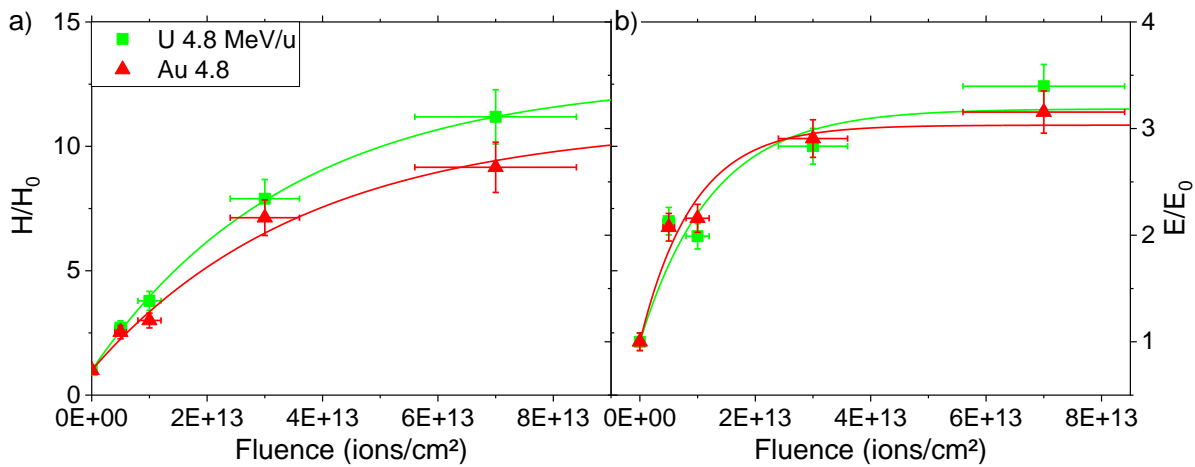


Figure 4.18: Relative change of a) hardness and b) Young's modulus of isotropic graphite with increasing 4.8 MeV/u U and Au ion fluence. Solid lines represent the respective Poisson's fits (Equation 4.1) with  $\sigma$  and  $H_{max}$  (a) and  $E_{max}$  (b) as fit parameter.

For many sample series, the number of samples with fluences of  $1 \times 10^{13}$  ions/cm<sup>2</sup> or more is not high enough for reliable fitting equation 4.1 to the data. Accordingly, only data from the irradiation with 4.8 MeV/u Au and U ions are considered. The damage cross sections deduced from the fits to the indentation data (Figure 4.18) are plotted in Figure 4.19 as a function of the energy loss. Compared to other materials especially insulators, the damage cross sections are unusually small (by a factor of 2-5). Furthermore, the damage cross section is barely changing with increasing energy loss.

Comparing the here deduced damage cross sections to literature values, the data follows roughly the trend of track radii in HOPG observed by Liu et al. [59] using scanning tunnelling microscopy (STM). Compared to thermal spike calculations by Toulemonde et al. [48] and to results of photothermal radiometry (PTR) measured by Prosvetov et al. [6,8], the values are smaller and almost constant with increasing energy loss. It can be concluded that the damage cross sections deduced from hardness and Young's modulus measurements do not follow the typical trend obtained during electronic stopping. The origin of the small damage cross section is probably linked to the high electrical conductivity of graphite that allows a quick dissipation of the deposited energy and limit the track formation to a small volume around the ion path. Moreover, given the simple structure of graphite rapid recrystallization is likely.

The damage cross sections deduced from the Young's modulus measurements are larger than the hardness values, as also obvious from the changes observed already at lower fluences (compare Figure 4.6, Figure 4.9 and Figure 4.10). This effect might be due to beam-induced stress around the ion track having a stronger influence on the Young's modulus than on the hardness.

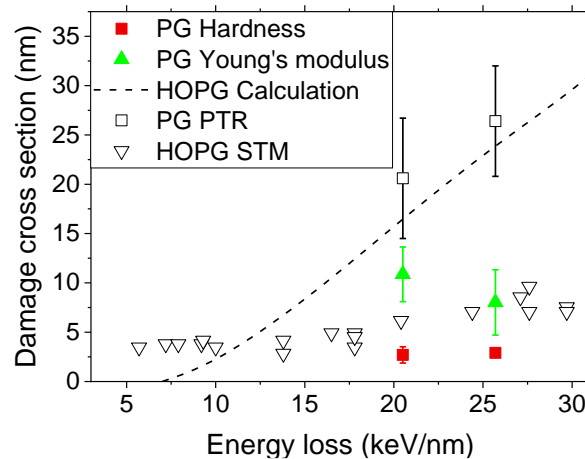


Figure 4.19: Damage cross section as a function of the energy loss. Results of hardness (red squares) and Young's modulus (green triangles) are compared to previous experimental data for polycrystalline isotropic graphite (PG) deduced from photothermal radiometry (PTR) [6] and for surface tracks in highly oriented pyrolytic graphite (HOPG) investigated by scanning tunnelling microscopy (STM) [59]. The dotted lines represent thermal spike calculations [48].

### 4.3 Investigation of dynamic mechanic properties of graphite by nanoimpact measurements

This section summarizes the results of the nanoimpact measurements. Section 4.3.1 presents experiments on the pristine isotropic graphite grades ZEE, R6650 and R6300. The influence of the impact parameters, the indenter geometry and the grain size of graphite are evaluated. Section 4.3.2 shows the development of the dynamic mechanical properties of these materials after heavy ion irradiation. In section 4.3.3 results of the CFC grades AC150k, Premium and Experimental Premium are summarized.

### 4.3.1 Influence of impact parameters on pristine samples

To test the validity of the nanoimpact method, pristine samples of the isotropic graphite grades ZEE, R6650 and R6300 are impacted with a wide range of impact parameters. The acceleration force is varied between 25 and 100 mN and the acceleration distance between 2.5 and 20.0  $\mu\text{m}$ . Furthermore, both a Berkovich and a cube corner indenter tip are used. Figure 4.20 shows the strain rate at a depth of 50 nm as a function of the incoming kinetic energy of the pendulum. The obtained strain rate is obviously very similar for all materials and does not depend on the tip geometry. Using different combinations of force and distance but the same kinetic energy also yields the same strain rate. This result is not unexpected since the surface strain rate is not influenced by the impacted material. It shows however that the method of fitting equation 3.8 to the strain rate data as shown in Figure 3.10 delivers very reliable results. The strain rate increases linearly with the velocity of the indenter tip and hence with the square root of the kinetic energy.

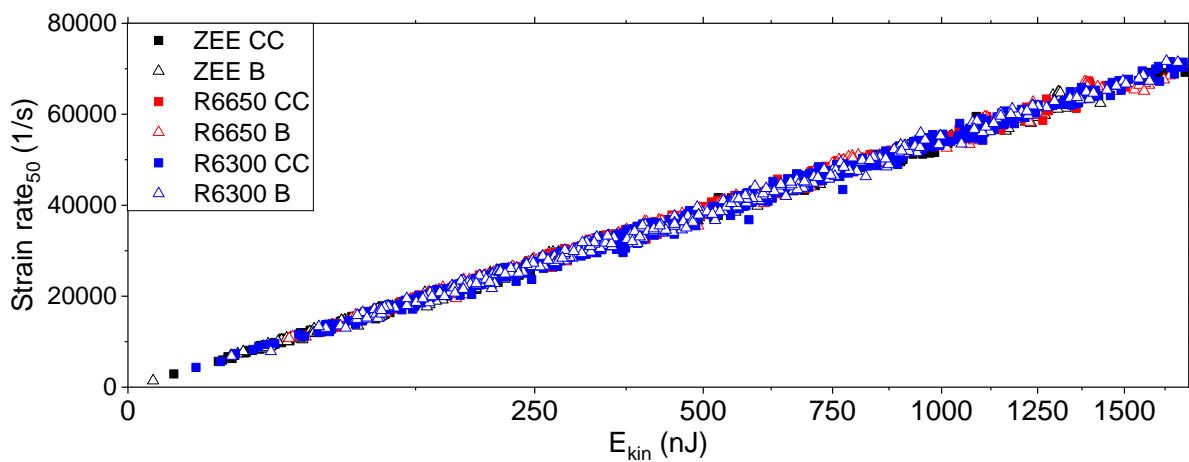


Figure 4.20: Strain rate at a depth of 50 nm as a function of kinetic energy on a square root scale of a Berkovich (B) and a cube corner (CC) tip impacting the isotropic graphite grades ZEE, R6650 and R6300.

Figure 4.21 shows the kinetic energy transferred during the first impact. For all investigated materials it increases linearly with increasing kinetic energy of the pendulum. For the investigated graphite grades an increasing energy transfer with increasing grain size can be observed. Especially ZEE has a very elastic response due its small grain size and the binder-free structure. An example of the influence of the

indenter geometry on the energy transfer is depicted in Figure 4.22 for R6650. The sharper indenter geometry leads to more plastic deformation and hence to a higher energy transfer.

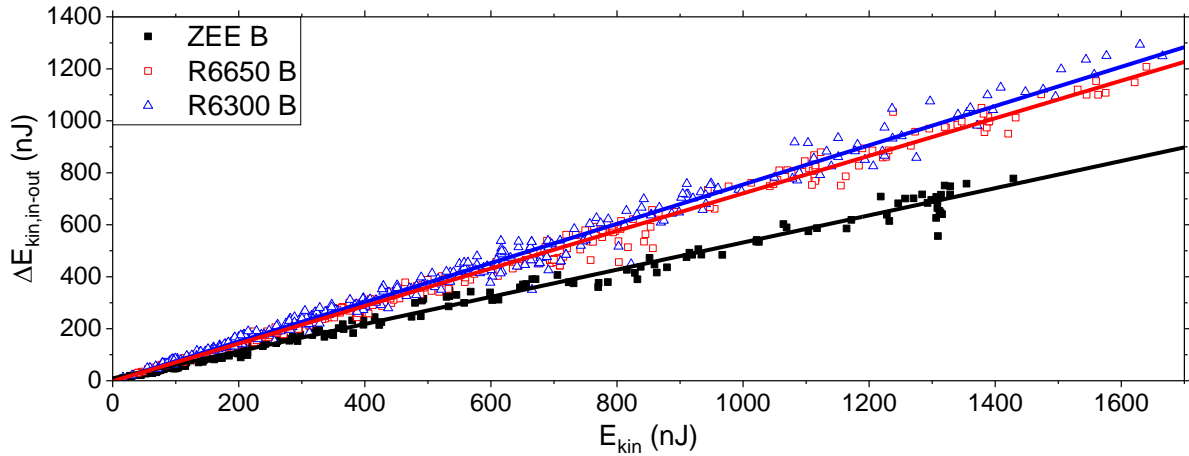


Figure 4.21: Difference between incoming and outgoing kinetic energy of the first impact as a function of incoming kinetic energy for isotropic graphite grades ZEE, R6650 and R6300 impacted with a Berkovich (B) tip. The solid lines represent linear fits.

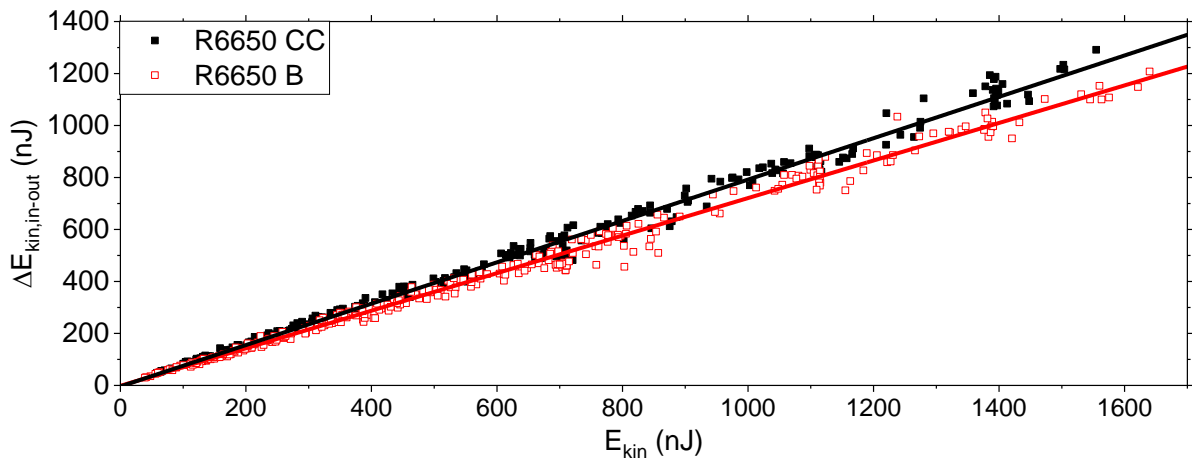


Figure 4.22: Difference between incoming and outgoing kinetic energy of the first impact as a function of incoming kinetic energy for isotropic R6650 graphite impacted with a cube corner (CC) and Berkovich (B) tip. The solid lines represent linear fits.

Similar to the difference of the incoming and outgoing kinetic energies, a damping constant (DC) can be calculated (equation 4.2) by fitting an exponential decay function to the maximum velocities  $v_{in,n}$  of the  $n$  bounces at their respective time  $t_n$ . Given that the transferred kinetic energy increases linearly with the kinetic energy, one would expect the damping constant to be independent of the impact parameters as well.

$$v_{in,n} = v_{in,max} \cdot e^{-DC \cdot t_n}$$

4.2

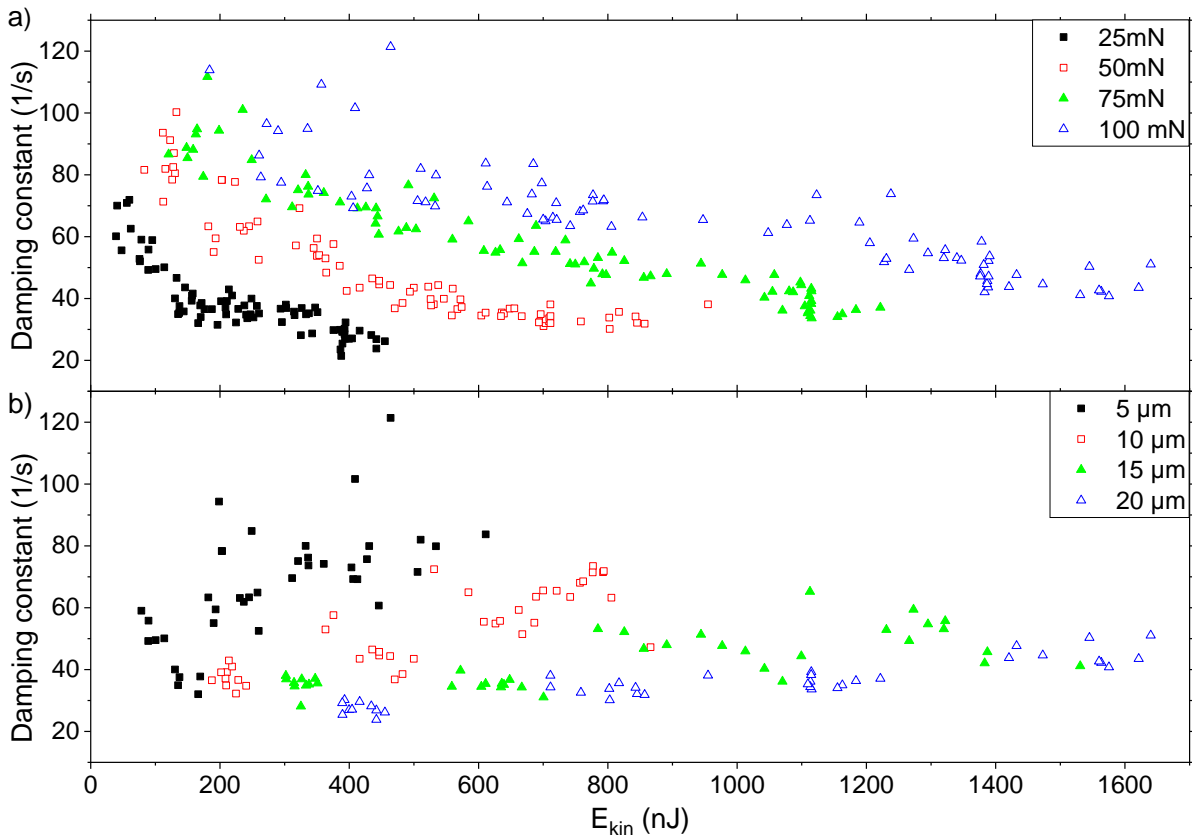


Figure 4.23: Damping constant as a function of incoming kinetic energy for isotropic R6650 graphite impacted with a Berkovich tip with different acceleration forces ranging from 25 to 100 mN in 25mN steps and distances ranging from 2.5 to 20.0  $\mu$ m in 2.5  $\mu$ m steps. The same data set is sorted by a) acceleration force and b) initial distance between indenter tip and sample surface. Data of only 4 different initial distances are shown in b) for better view.

However, as can be seen in Figure 4.23, this is not the case. The damping constant increases with increasing acceleration force and decreases with increasing acceleration distance. While the kinetic energy difference between the bounces is independent of the parameters, the time duration of the bounces is not. For a constantly accelerated object, the time  $t$  depends on distance  $s$  and acceleration  $a$  (Equation 4.3).

$$t = \sqrt{\frac{2 \cdot s}{a}} \quad 4.3$$

In order to obtain a property that is independent of the selected parameters, the damping factor  $k$  is derived from the damping constant  $DC$ , the acceleration force  $F$  and the distance between the indenter tip and the surface  $d$  (Equation 4.4).

$$k = DC \cdot \sqrt{\frac{F}{d}} \quad 4.4$$

The damping factors calculated with equation 4.4 as a function of the kinetic energy of the impacting indenter are shown in Figure 4.24. Considering the scattering of the data points, the damping factor is almost a constant value independent on the selected acceleration force or distance. As observed by the linear slope of the difference between the incoming and outgoing kinetic energy in Figure 4.21, different kinetic energies do not lead to different deformation mechanisms in the investigated range.

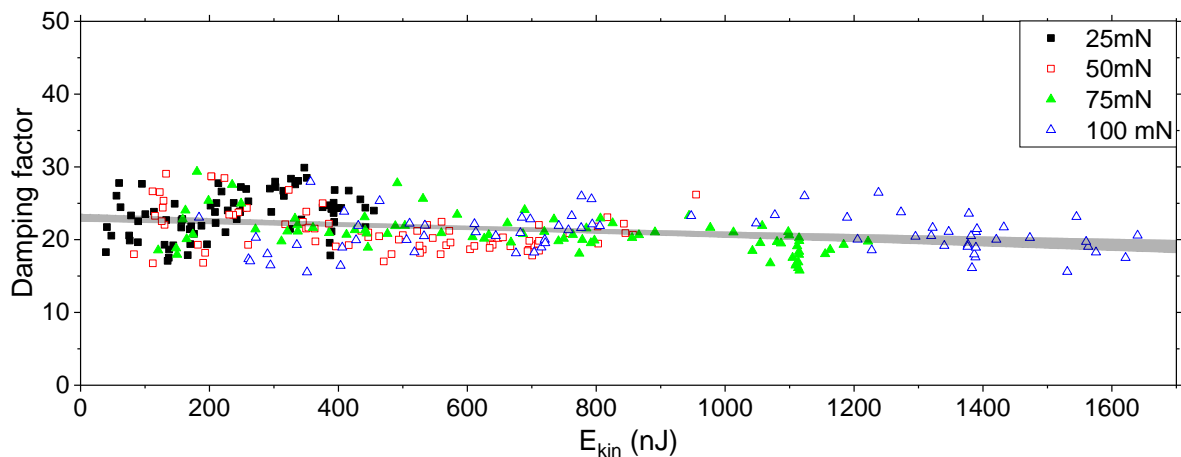


Figure 4.24: Damping factor as a function of incoming kinetic energy for isotropic R6650 graphite impacted with a Berkovich tip with different acceleration forces and distances. The shaded area represents the 95 % confidence interval of a linear fit to the entire data set.

Similar results are obtained for all three grades of isotropic grades (Figure 4.25). However, it can be seen that the damping factors are different between the grades. R6300 with the largest grain size also possesses the highest damping factor even though it is only slightly higher compared to the similarly produced R6650 with a smaller grain size. ZEE has a considerably lower damping factor corresponding to a higher portion of the impact transferred to elastic deformation due to the small grain size and the binderless structure.

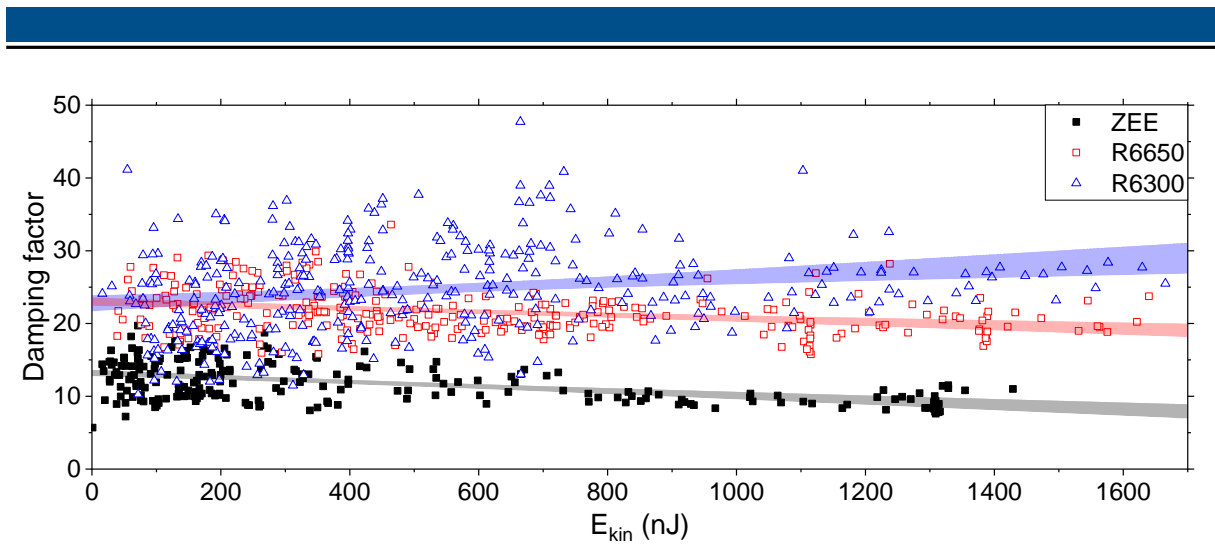


Figure 4.25: Damping factor as a function of incoming kinetic energy for isotropic graphite grades ZEE, R6650 and R6300 impacted with a Berkovich tip with different acceleration forces and distances. The shaded areas represent the 95 % confidence intervals of linear fits to the entire data sets of the three graphite grades.

The corresponding dynamic hardness values calculated with equation 3.9 as a function of kinetic energy are shown in Figure 4.26. Using the kinetic energy difference between before and after the first bounce shows a dependence on the acceleration distance and force used, whereas the dynamic hardness proves to be independent due to the inclusion of the volume of the residual impact. Comparing the three isotropic graphite grades and all used kinetic energies, the dynamic hardness becomes larger for smaller grain size with the highest values obtained for ZEE and the smallest values for R6300. The same sequence is observed for the quasi-static hardness, as well. For all three isotropic grades the dynamic hardness is high for low energies and becomes almost constant above ~500 nJ.

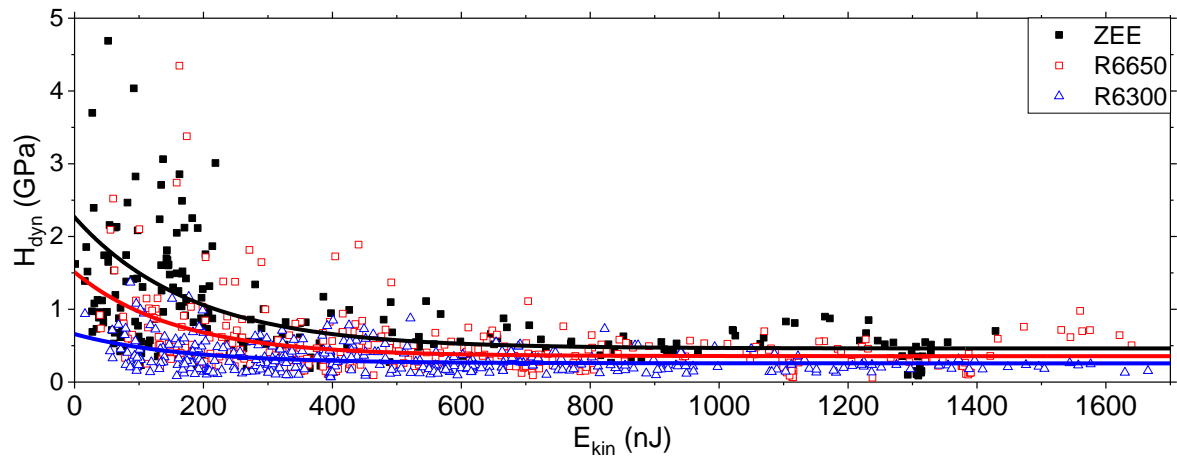


Figure 4.26: Dynamic hardness as a function of incoming kinetic energy for isotropic graphite grades ZEE, R6650 and R6300 impacted with a Berkovich tip with different acceleration forces and distances. Exponential decay curves are fitted to the corresponding data points as a guide for the eye.

With decreasing kinetic energy, the penetration depth into the material decreases. The effect that the hardness can depend on the indentation depth has been shown for several materials [118] including graphite [119]. This so-called indentation size effect is ascribed to the fact that for smaller indents geometrically necessary dislocations induced by the deformation need to be stored in a smaller volume, resulting in a higher strain gradient relative to the size of the plastic zone [120,121]. Comparing the dynamic and quasi-static hardness of graphite in Figure 4.27, the depth dependence of the dynamic hardness measurements is more pronounced. Similar effects were observed in aluminium by Qin et al. [122]. Moreover, it was previously shown that shorter loading times can lead to a larger indentation size effect for quasi-static indentation [123,124]. Very fast application of the load during impact indentation should therefore have a strong effect at low impact depth. To avoid these problems, the impact indentation experiments of irradiated PG and CFC are conducted with an acceleration force of 50 mN and an initial distance between indenter tip and sample surface of 10  $\mu\text{m}$  yielding kinetic energies of 500 nJ, where the measured dynamic hardness is rather constant (Figure 4.26 and Figure 4.27).

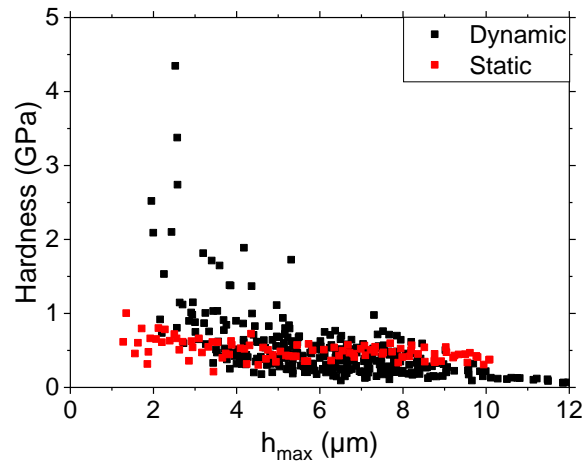


Figure 4.27: Dynamic and static hardness as a function of maximum depth for isotropic R6650 graphite impacted with a Berkovich indenter.

Results of nanoimpact measurements of pristine graphitic materials are illustrated in Figure 4.28. The obtained dynamic hardnesses are similar to the quasi-static hardnesses (Figure 4.4). Among the isotropic graphite grades both dynamic and static hardness increase with decreasing grain size indicating higher sturdiness due to the grain boundaries. For the investigated CFC grades, SGL Experimental Premium has the lowest dynamic hardness. The additional heating step compared to SGL Premium results in a slight softening of the material. AC150k has a similar dynamic hardness as SGL Experimental Premium, but a higher damping constant. The obtained dynamic hardness is approximately half and one third of the quasi-static hardness for Sigradur G and K, respectively. While Sigradur K had both a larger quasi-static hardness and Young's modulus compared to Sigradur G, the dynamic hardness is lower and the damping factor is larger, which might indicate brittle behaviour of this grade. The damping factor of Sigradur G is about one fifth of the other graphitic materials. Most of the incoming kinetic energy is not transformed to plastic deformation but elastically reverted to a repulsion of the indenter tip.

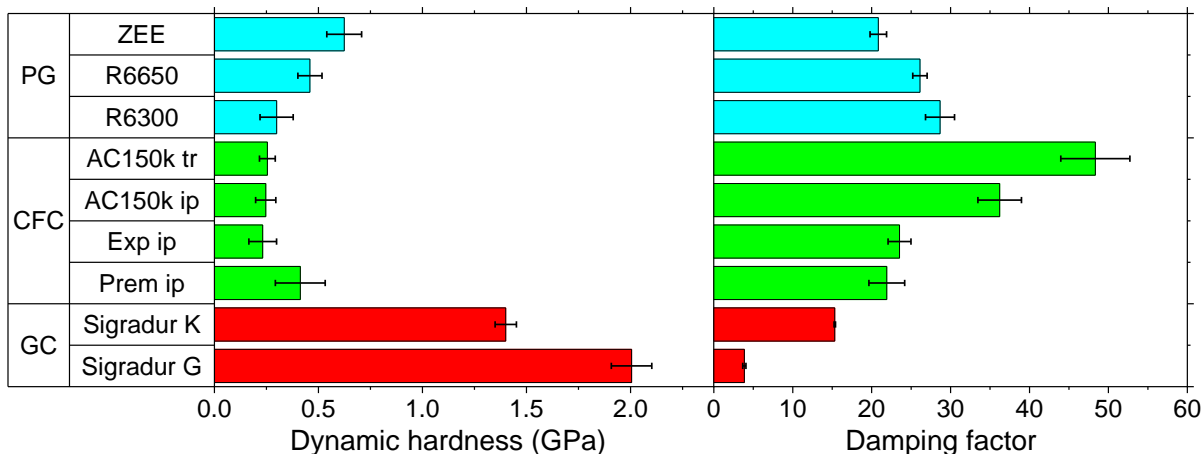


Figure 4.28: Dynamic hardness and damping factor of pristine graphitic materials obtained by nanoimpact measurement. A Berkovich indenter is accelerated with a force of 50 mN from a distance of 10  $\mu\text{m}$ .

### 4.3.2 Beam-induced changes of dynamic properties of isotropic polycrystalline graphite

Figure 4.29 shows a typical comparison of depth vs time measurement of an impact on isotropic graphite, both pristine and irradiated with 4.8 MeV/u Au ions to a fluence of  $7 \times 10^{13}$  ions/cm<sup>2</sup>. For both samples, the impact parameters are the same obvious by the similar distance and slope of the initial section of the curve. For the irradiated sample, the maximum achieved depth is significantly reduced illustrating the increased resistance to penetration as already observed by the increase of the quasi-static hardness. The decreased plastic deformation due to the increased hardness leads to a larger elastic contribution visible by the larger distance between maximum penetration depth and the subsequent minimum depth after the repulsion of the indenter tip and the reduced damping. Small distortions with a higher frequency are visible for the sample irradiated with Au ions in Figure 4.29. These are attributed to the ringing of the pendulum [89,93] which occurs for harder and more elastic materials. However, they are small and do not significantly affect the evaluation.

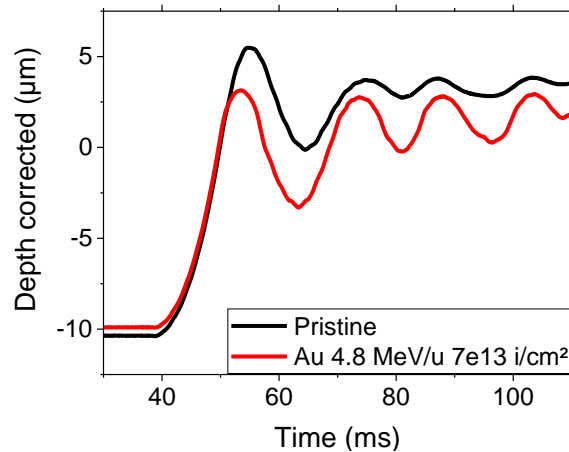


Figure 4.29: Depth signal of a dynamic hardness measurement for isotropic R6650 graphite, both pristine and irradiated with 4.8 MeV/u Au ions to a fluence of  $7 \times 10^{13}$  ions/cm<sup>2</sup>. A Berkovich indenter is accelerated with a force of 50 mN from a distance of 10  $\mu\text{m}$ .

For all the investigated samples of isotropic R6650 graphite grade, the relative change of dynamic hardness and damping factor as a function of irradiation fluence are summarized in Figure 4.30. The results show a similar trend as observed for the static hardness and Young's modulus with large changes of the samples irradiated with 4.8 MeV U and Au ions. Both dynamic hardness and damping factor approach the values obtained for the glassy carbon grade Sigradur G. Samples irradiated with ions of energy loss lower than 18 keV/nm (Table 3.1) have smaller changes. However, the dynamic hardness increases still by 70 % of the pristine value for the highest investigated fluences. Above the critical energy loss of 18 keV/nm the quasi-static hardness increase is approximately 2 times larger than the dynamic hardness increase. The sensitivity of the dynamic hardness is more similar to the changes observed for the Young's modulus. The ratio of outgoing to incoming kinetic energy depends on the elastic properties of the material which might explain the similarity of the changes of these two mechanical properties.

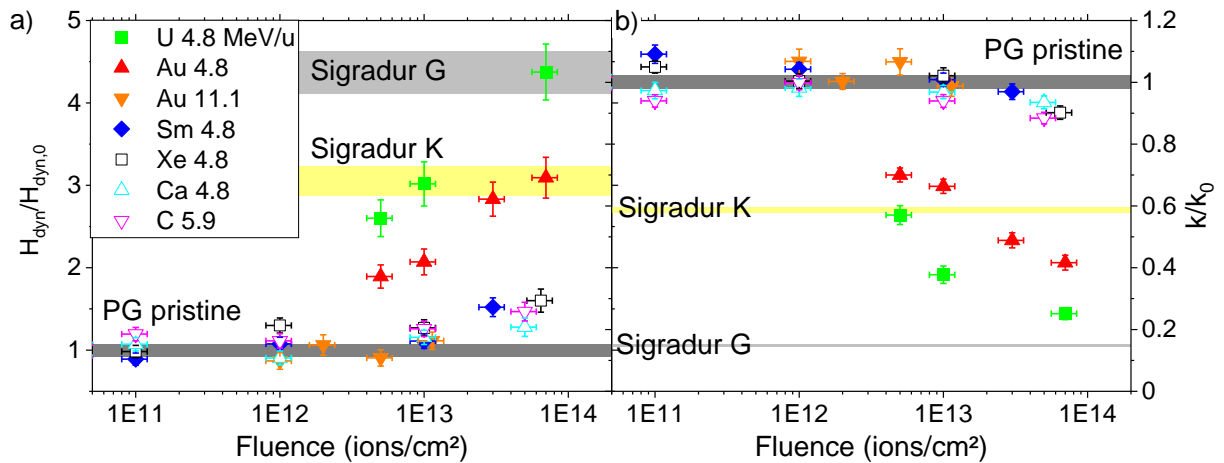


Figure 4.30: Relative change of a) dynamic hardness and b) damping factor for isotropic R6650 graphite as a function of the fluence for various ion species. A Berkovich indenter is accelerated with a force of 50 mN from a distance of 10  $\mu\text{m}$ . Yellow and dark and light grey bands indicate the respective values of pristine R6650 and glassy carbon Sigradur K and G.

Changes of dynamic hardness and damping factor induced by 4.8 MeV/u Au ion irradiation of SGL R6650, SGL R6300 and POCO ZEE are compared in Figure 4.31. The dynamic hardness of POCO ZEE remains similar to the pristine hardness up to the highest investigated fluence of  $5 \times 10^{13}$  ions/cm<sup>2</sup>. The dynamic hardness increase of R6300 is very similar to the irradiation induced increase of the quasi-static hardness (Figure 4.6). R6650 on the other hand has a lower increase of the dynamic hardness on a similar level as R6300 at fluences above  $3 \times 10^{13}$  ions/cm<sup>2</sup>. As observed during the irradiation of R6650 with different ion species, the dynamic hardness increase is more similar to the increase of the Young's modulus than the increase of the quasi-static hardness.

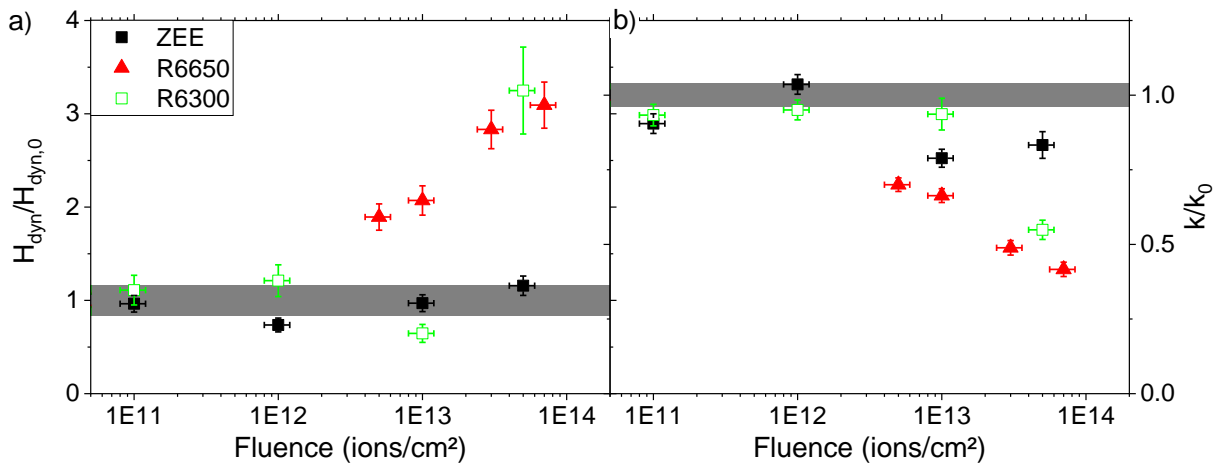


Figure 4.31: Relative change of a) dynamic hardness and b) damping factor for isotropic graphite grades ZEE, R6650 and R6300 as a function 4.8 MeV/u Au ion fluence. A Berkovich indenter is accelerated with a force of 50 mN from a distance of 10  $\mu\text{m}$ . The dark grey band indicates the values of the pristine isotropic graphite grades with the largest respective error.

### 4.3.3 Beam-induced changes of dynamic properties of carbon fibre reinforced carbon

Au ion induced relative changes of the dynamic hardness and damping factor of carbon fibre reinforced carbon grades are presented in Figure 4.32. The transversal orientation of AC150k increases more than its in-plane orientation. Similar differences are observed for quasi-static hardness measurements. While the obtained pristine values are almost equal in both orientations for this grade, the damage mechanism responsible for the large changes in mechanical properties seem to be suppressed in the direction perpendicular to the fibres. This is supported by significantly smaller changes of the mechanical properties of the SGL grades compared to AC150k. These grades have a woven fibre structure with more and highly oriented fibres and less matrix and a visibly reduced matrix fraction. As already seen for the quasi-static hardness measurements, the data on these two SGL grades scatter considerably from sample to sample due to the structure of the fibre bundles. The damping constant of Experimental Premium is larger than its pristine value for all investigated fluences. Premium shows a contrary behaviour with its damping constant being below the pristine value. In general, there is little influence of the ion fluence on the damping constant for both SGL grades.

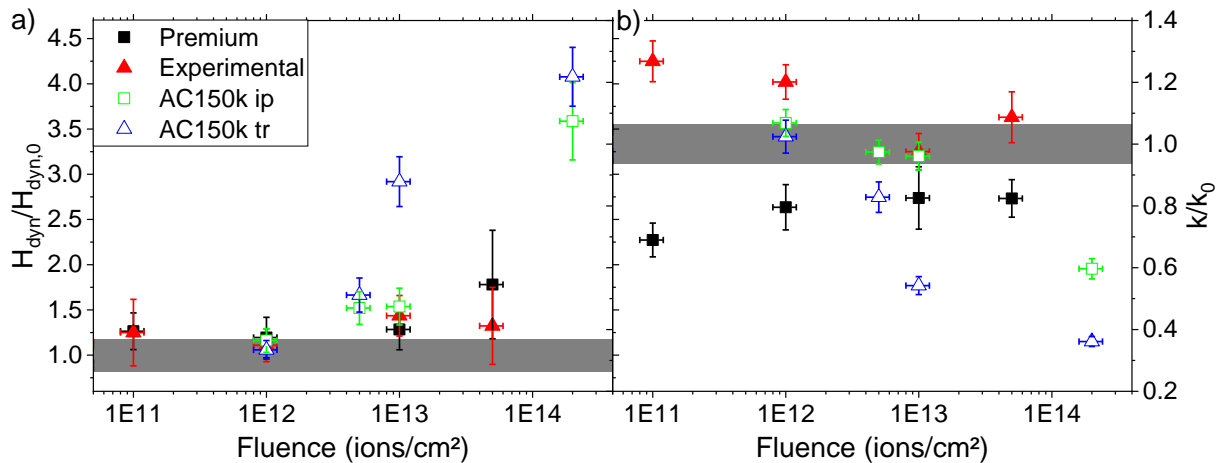


Figure 4.32: Relative change of a) dynamic hardness and b) damping factor of carbon fibre reinforced carbon grades Premium and Experimental Premium as a function the 4.8 MeV/u Au ion fluence and AC150k as a function the 3.6 MeV/u Au ion fluence. A Berkovich indenter is accelerated with a force of 50 mN from a distance of 10  $\mu\text{m}$ . The dark grey band indicates the values of the pristine CFC grades with the largest respective error.

## 4.4 Observation of fatigue failure by multiple impact measurements

To investigate the response of materials exposed to repeated loads as occurring in pulsed beam conditions, multiple impulse experiments are conducted. To increase the local load a cube corner indenter tip is used. To observe the overall behaviour of the materials, the obtained depth vs. time signals are averaged. The respective results for pristine isotropic graphite and carbon fibre reinforced carbon samples are presented in Figure 4.33. The zero position corresponds to the initial sample surface while the depth signal at the time when the indenter is moved back to the starting position is -3  $\mu\text{m}$  (not shown). Fatigue failure occurring during the single measurements are not visible due to the averaging.

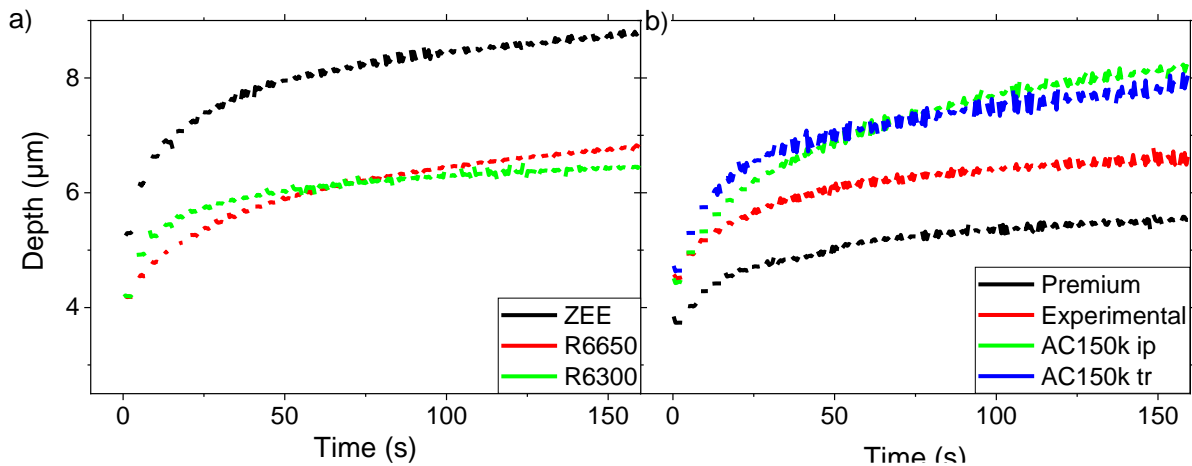


Figure 4.33: Depth as a function of time of multiple impulse measurements of a) isotropic graphite grades ZEE, R6650 and R6300 and b) CFC grades SGL Premium, SGL Premium Experimental in in-plane orientation and AC150k with both orientations. The curves show the average of 20 positions, impacted 40 times with a frequency of 0.25 Hz by a cube corner indenter with an acceleration force of 30 mN from a distance of 3 µm. The 95 % confidence interval of the averaged curves is smaller than  $\pm 0.5 \mu\text{m}$  for the PG grades and  $\pm 1.4 \mu\text{m}$  for the CFC grades (not shown for better view).

For isotropic graphite the largest depth is obtained for POCO ZEE. While it has both a larger quasi-static and dynamic hardness, the sharper shape of the cube corner seems to allow an easier cutting of the smaller grains with better graphitization. The depth is smallest for R6650 for the first ~15 impacts. However, the depth in R6650 rises faster than that in R6300 leading to a greater depth with larger impact numbers. The steeper rise can be explained by a higher number of failures detected in the measurements as obvious in Figure 4.34 a). While only less than 15 % of the measurement positions of R6300 showed signs of failure over the course of 75 impacts, more than 50 % of the positions failed for R6650. POCO ZEE has an even higher failure probability explaining the larger depth contrary to the results obtained by quasi-static and dynamic hardness measurements.

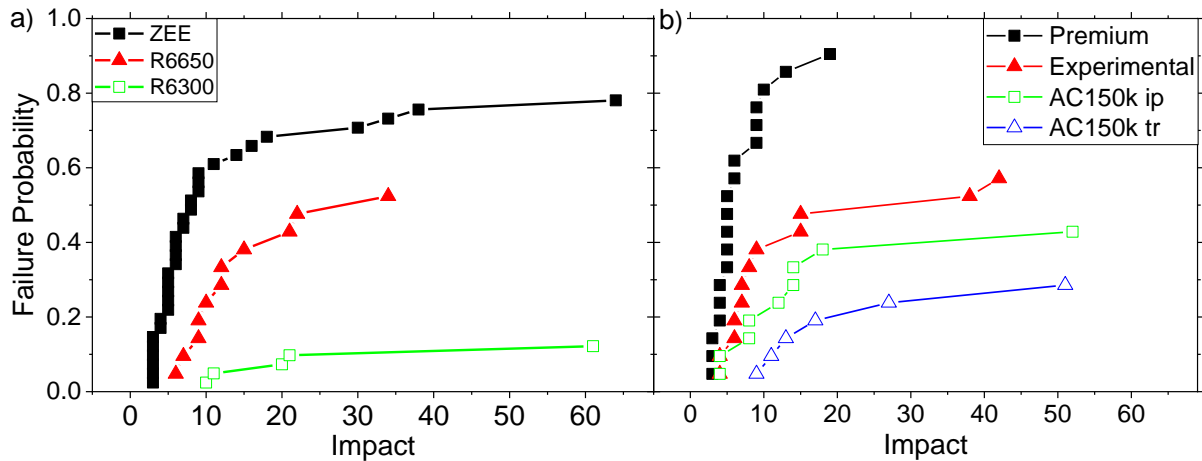


Figure 4.34: Failure probability depending on the impulse number of a) isotropic graphite grades ZEE, R6650 and R6300 and b) CFC grades SGL Premium, SGL Premium Experimental for in-plane orientation and AC150k for both orientations.

The results obtained for carbon fibre reinforced carbon are shown in Figure 4.33 b) and Figure 4.34 b). Impacts on SGL Premium led to the smallest penetration depth of the investigated grades. It is shown in chapter 4.2.1 that SGL Premium possesses the highest hardness of the CFC grades. However, this high hardness results in embrittlement as can be seen by a failure probability of more than 90 % of the positions after 20 impacts. The additional heat step during the production of SGL Premium Experimental obviously reduces the hardness compared to SGL Premium leading to a higher penetration depth. The brittleness seems also reduced because the failure probability is smaller. Both orientations of AC150k have a similar penetration depth, larger than that observed for the SGL grades. While the woven structure of the SGL grades has a higher resistance against the penetration, breaking the bundles leads to more sudden increases of the depth after repeated impact. The fibres of AC150k are less oriented leading to less resistance against penetration but fewer failures. The failure probability is higher for the in-plane orientation leading to a slightly larger depth after approximately 15 impacts.

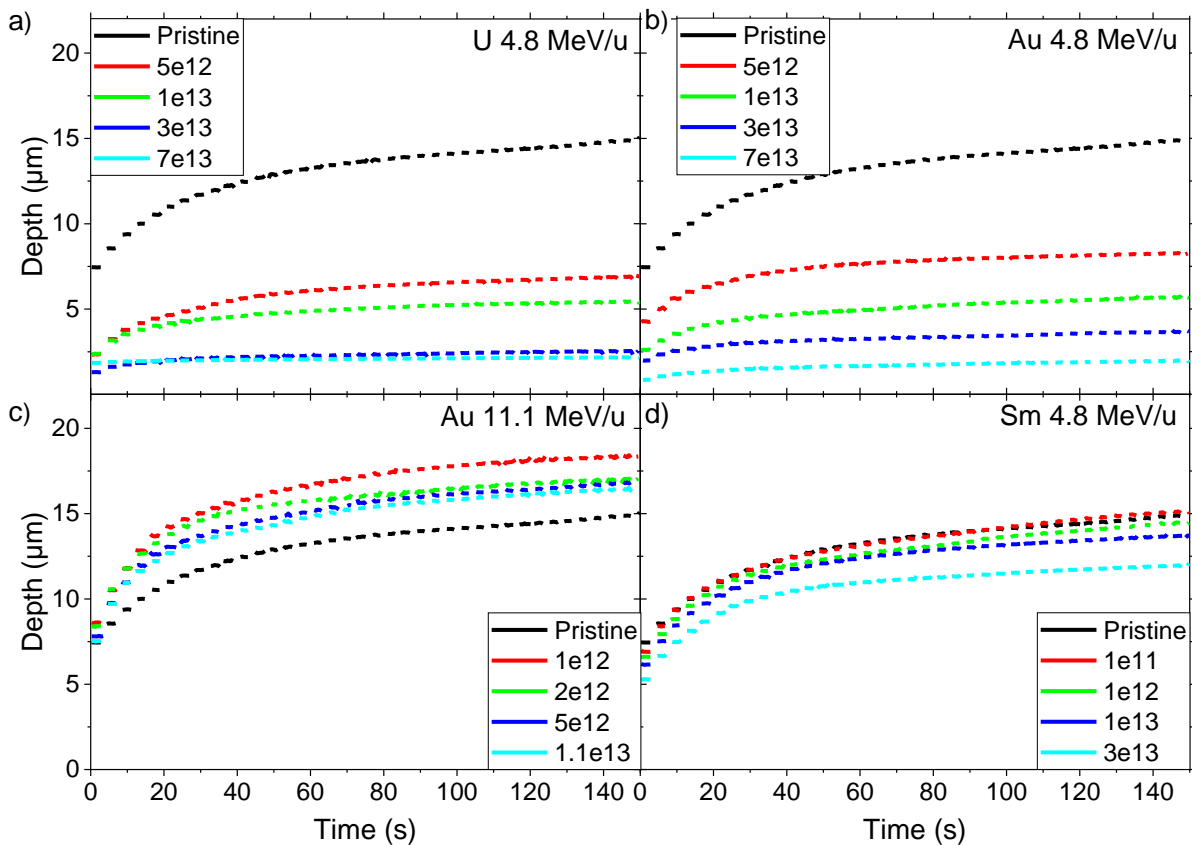


Figure 4.35: Depth as a function of time of multiple impulse measurements for isotropic R6650 graphite irradiated with a) 4.8 MeV/u U, b) 4.8 MeV/u Au, c) 11.1 MeV/u Au and d) 4.8 MeV/u Sm ions to different fluences in ions/cm<sup>2</sup>. The curves show the average of 20 positions, impacted 37 times with a frequency of 0.25 Hz by a cube corner indenter with an acceleration force of 30 mN from a distance of 3 μm. The 95 % confidence interval of the averaged curves is smaller than ± 0.5 μm for all samples (not shown for better view).

Figure 4.35 and Figure 4.36 show the fatigue response to multiple impact measurements of SGL R6650 samples irradiated with various ions. Similar to the results obtained from quasi-static and dynamic hardness measurements only a slight reduction of the penetration depth occurred for irradiation with 4.8 MeV/u Sm ions. For irradiation with 11.1 MeV/u Au ions the penetration depth even slightly increases. A slight decrease of quasi-static and dynamic hardness at low fluences is as well observed in Figure 4.6 and Figure 4.30 for this fluence series, however, less visible due to the large scale required for the figures. This increase can be caused by annealing due to the low irradiation flux used at the X0-branch. Irradiation with 4.8 MeV/u Au or U ions on the other hand resulted in a large reduction of the penetration depth to less than one sixth of the pristine penetration depth. The large effect (Figure 4.36) emphasizes the important role of the energy loss. The data

suggests that the transformation to a structure similar to glassy carbon as observed for quasi-static hardness and Raman spectroscopy requires a critical energy loss of at least 18 keV/nm.

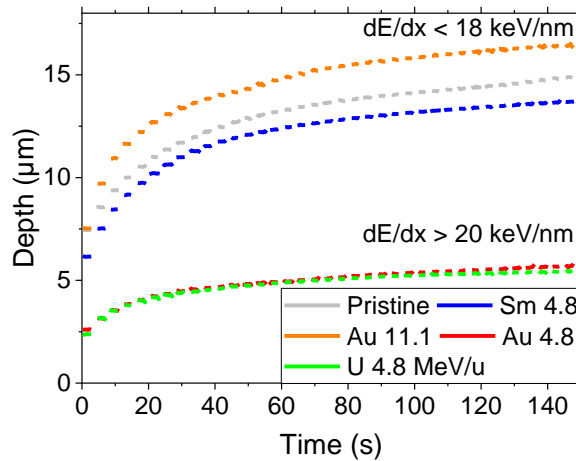


Figure 4.36: Averaged depth as a function of time of multiple impulse measurements for isotropic R6650 graphite irradiated with different ions to a fluence of  $1 \times 10^{13}$  ions/cm<sup>2</sup> ( $1.1 \times 10^{13}$  ions/cm<sup>2</sup> for 11.1 MeV/u Au irradiation). Samples are impacted 75 times with a frequency of 0.25 Hz by a cube corner indenter with an acceleration force of 30 mN from a distance of 3 µm. The 95 % confidence interval of the averaged curves is smaller than  $\pm 0.5$  µm for all samples (not shown for better view).

The obtained failure probabilities of SGL R6650 irradiated with various ion species are illustrated in Figure 4.37. The results obtained for irradiation with 4.8 MeV/u Sm and 11.1 MeV/u Au ions have slightly decreased failure probabilities compared to the pristine sample, but mostly within the scattering of the data. Irradiation with 4.8 MeV/u U and Au ions on the other hand show a large decrease of the failure probability at fluences from  $5 \times 10^{12}$  to  $3 \times 10^{13}$  ions/cm<sup>2</sup>. The increase of the hardness and the Young's modulus results in a larger resistance against the first impact and lowers the chance for additional plastic deformation of subsequent impacts. A reversed effect is observed for samples irradiated to a fluence of  $7 \times 10^{13}$  ions/cm<sup>2</sup>. The failure probability increases again, especially at low impact numbers. This behaviour might indicate embrittlement of the structure due to the phase transformation to a structure similar to glassy carbon.

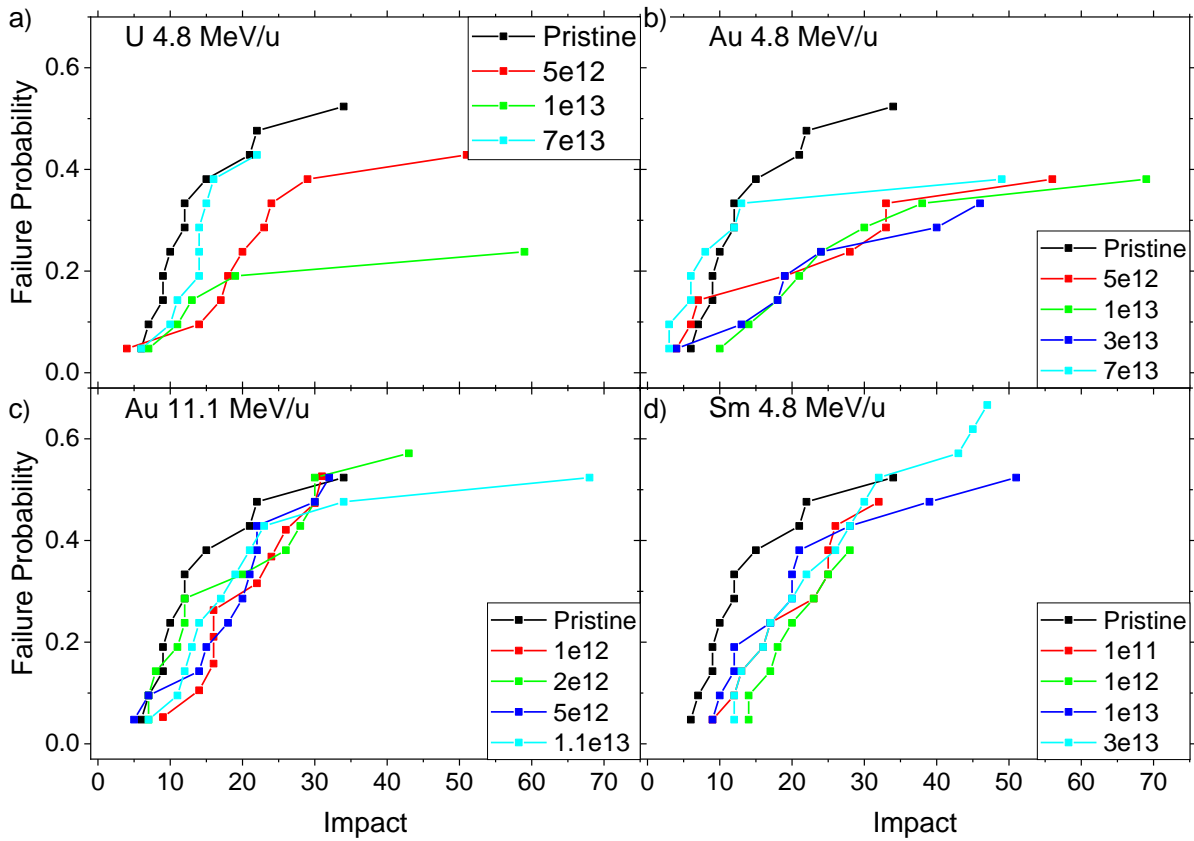


Figure 4.37: Failure probability for isotropic graphite SGL R6650 irradiated with a) 4.8 MeV/u U, b) 4.8 MeV/u Au, c) 11.1 MeV/u Au and d) 4.8 MeV/u Sm ions to different fluences in ions/cm<sup>2</sup>. A Berkovich indenter is accelerated with a force of 30 mN from a distance of 3  $\mu$ m. This impact is repeated 75 times at 20 different positions of each sample. Failures are detected as demonstrated in Figure 3.11.

---

## **5 Online monitoring of beam-induced bending and stress waves**

---

The following chapter presents the results of the online monitoring of bending and stress waves [125]. With the set-up described in 3.4.1, the temperature and the velocity at the rear side of thin discs during the impact of 4.8 MeV/u U ion pulses are recorded. In section 5.1 the simulation results of the temperature evolution during the impact of a U ion impact are described. The temperature difference between the beam spot and the surrounding unirradiated material results in stress which finally leads to bending and stress waves within the material. Recorded surface velocities and the comparison to calculations described in section 3.4.2 and simulations described in section 3.4.4 allow conclusions about beam-induced changes of material properties of the irradiated discs. Section 5.2 presents the results for tungsten and copper. Material parameters of these metals are well known and thus allow the testing of the method. In the subsequent sections the results of several different graphitic materials are shown. Section 5.3 shows the results of isotropic graphite. Carbon fibre reinforced carbon (Section 5.4) and flexible graphite (Section 5.5) are more challenging due to their anisotropic properties. Glassy carbon is rather brittle which resulted in chipping of the irradiated part as shown in section 5.6. Finally, the results of hexagonal boron nitride are presented in section 5.7. While the structure is similar to isotropic graphite, brittleness of this ceramic leads to sample fracturing. Indications of this process is already visible in the LDV velocity signal before the final fracture occurs.

---

### **5.1 Temperature development during U ion beam impacts**

---

To estimate the maximum temperature rise per pulse, it is assumed that the entire energy of a U ion pulse is converted into heat. For graphite this corresponds to a power density of  $\sim 3 \text{ MW/cm}^2$ . In the FEM simulations this value is inserted continuously over the duration of the 100  $\mu\text{s}$  long ion pulse. The results of simulations of a quarter of a graphite disc with a diameter of 20 mm and a thickness of 0.5 mm exposed to a square beam spot of  $1 \times 1 \text{ cm}^2$  are shown in Figure 5.1. They are representative for the different

materials and dimensions. Adiabatic boundary conditions are used justified by the short time scales of the involved processes. Figure 5.1 a) shows the simulated temperature evolution as a function of time for a single U ion beam pulse on a pristine isotropic graphite disc at different depths ( $z = 0, 0.06, 0.25$  and  $0.5$  mm) and radial positions ( $y = 0, 5$  and  $10$  mm). The temperature of the quasi-pristine sample increases during the duration of the pulse and reaches a maximum of  $156$  °C at the end of the ion pulse at  $100$   $\mu$ s in the centre of the beam spot ( $y = 0$  mm,  $z = 0$  mm). The generated heat is conducted through the sample equilibrating within  $1$  ms to almost the same temperature values on both surfaces of the disc ( $y = 0$  mm, compare  $z = 0$  and  $0.5$  mm). Over the entire time the outer rim of the disc ( $y = 10$  mm,  $z = 0$  mm) remains at room temperature, confirming that the use of adiabatic conditions in the investigated time frame is adequate.

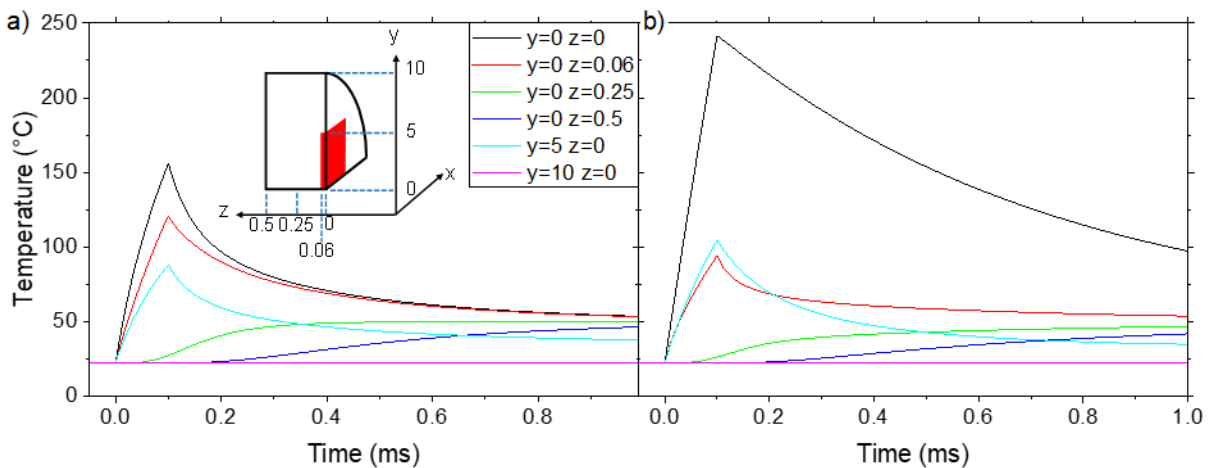


Figure 5.1: FEM simulated time dependent temperature evolution of a  $0.5$  mm thick isotropic graphite disc for  $1$  ms after the impact of a  $100$   $\mu$ s long U ion pulse. Coordinates are in millimetres and the sample orientation is shown in the inset. All points are at  $x = 0$  mm. More details can be seen in Figure 3.14. a) pristine material b) calculation for graphite of reduced thermal conductivity in the beam spot ( $4$  W/m·K [8] instead of  $95$  W/m·K) corresponding to graphite irradiated with  $4.8$  MeV/u U ions to a fluence of  $3 \times 10^{13}$  ions/cm<sup>2</sup>.

To simulate the case of a radiation-damaged sample, the thermal conductivity of the volume exposed to the beam is reduced to  $4$  W/m·K [8]. The density is kept constant since radiation-induced swelling was shown to be below  $5$  % [7,126]. The values of specific heat and coefficient of thermal expansion are expected to change towards those of glassy carbon [8,30]. As the difference of these two properties between graphite and glassy carbon is small, they are kept constant for the simulation. Due to

the degraded thermal conductivity, the temperature at the sample surface ( $y = 0$  mm,  $z = 0$  mm) increases to 240 °C after a U ion pulse of 100  $\mu$ s duration. A temperature of 255 °C is obtained if no heat conduction is included illustrating the severely limited heat conduction from the front of the sample within the time duration of the pulse. The temperature in a depth where the ions stop ( $y = 0$  mm,  $z = 0.06$  mm) is lower than observed for the pristine sample. For damaged material, the dissipation of the energy deposited in the central beam spot is obviously slowed down whereas heat conduction into the pristine surrounding is not affected. After 1 ms the temperature difference between the front and the back surface of the sample, at the central spot of the beam ( $y = 0$  mm, compare  $z = 0$  and 0.5 mm), is still larger than 50 °C. The achieved temperature evolutions are used as input for the mechanical simulations, presented in the subsequent chapters.

## 5.2 Metals

Velocity signals and corresponding fast FFT measured by LDV of a 110  $\mu$ m thick tungsten disc with a diameter of 2 cm and a spherical beam spot of 6 mm diameter are shown in Figure 5.2. For clarity, only data after the accumulation of a fluence of  $4 \times 10^{11}$  and  $6 \times 10^{12}$  ions/cm<sup>2</sup> are presented.

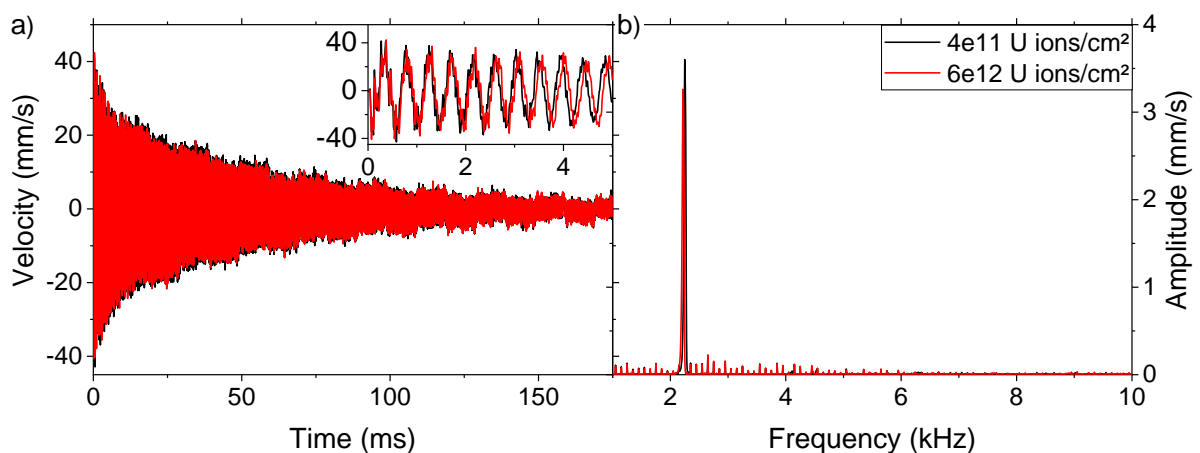


Figure 5.2: a) Time dependent velocity signal measured by LDV and b) corresponding FFT spectra at the rear side of a 0.11 mm thick tungsten disc with a diameter of 2 cm for the irradiation with 4.8 MeV/u U ions at different fluences. The inset in a) shows a zoom-in to the initial 5 ms of the signal.



of the ion beam and hence results in a smaller deformation of tungsten. It is also noticed that the damping in copper is far higher than in tungsten.

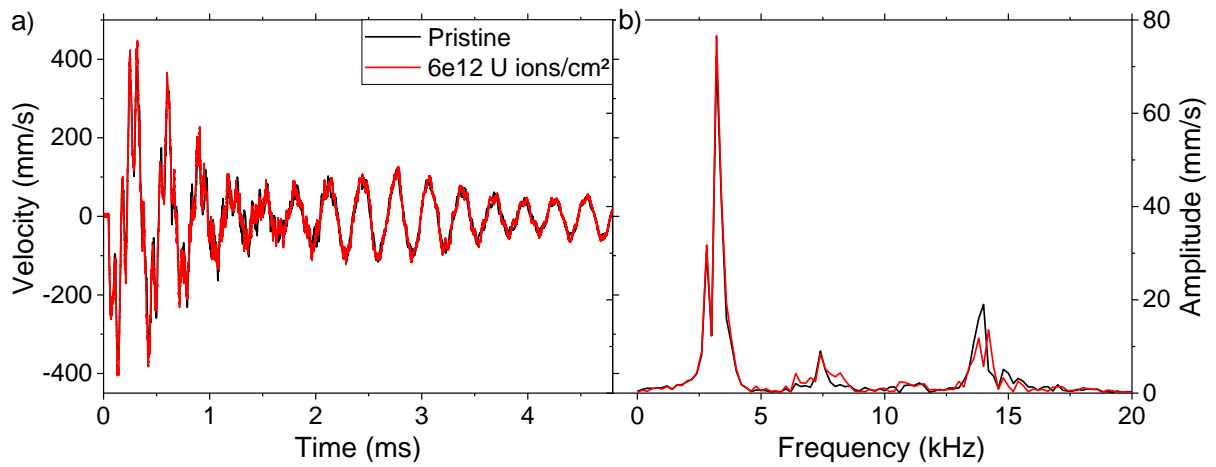


Figure 5.4: a) Time dependent velocity signal measured by LDV and b) corresponding FFT spectra at the rear side of a 0.2 mm thick copper disc with a diameter of 2 cm for the irradiation with 4.8 MeV/u U ions at different fluences.

With increasing U ion fluence no change of the signal is observed (Figure 5.5), suggesting no severe damage to the material and thus no change of the material parameters.

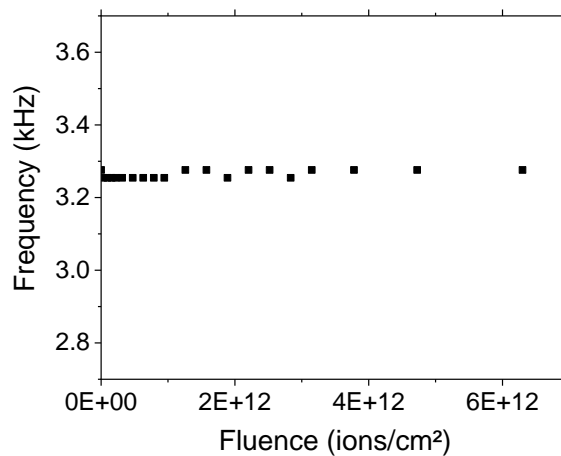


Figure 5.5: Measured bending frequency of a 0.2 mm thick copper disc with a diameter of 2 cm as a function of accumulated 4.8 MeV/u U ion fluence.

---

## 5.3 Isotropic polycrystalline graphite

---

Figure 5.6 a) and b) show velocity signals and corresponding FFTs spectra measured with the LDV at the rear side of a 500  $\mu\text{m}$  thick SGL R6650 disc with a diameter of 2 cm impacted with 4.8 MeV/u U ions. The beam spot is a square with an area of 1x1  $\text{cm}^2$ . Due to problems during the recording the measured voltage of this sample could not be converted to velocities. Thus, the raw voltage signal is presented and the focus is put on the frequency spectra of the involved processes. In the quasi-pristine sample a harmonic oscillation with a frequency of  $5.38 \pm 0.02$  kHz is generated in excellent agreement with the frequency  $f_{b1,free}$  of 5.32 kHz calculated for the free binding condition (Equation 3.20). With increasing U ion fluence, the frequency signal increases to  $6.10 \pm 0.02$  kHz at the maximum applied fluence of  $3.5 \times 10^{13}$  ions/ $\text{cm}^2$ . The increase of the frequency is ascribed to an increase of the Young's modulus in the irradiated area, assuming that the boundary conditions remained constant because no large failures of the samples such as cracks are observed using optical microscopy. As discussed in section 2.4, the irradiation of graphite results in the formation of interstitials and vacancies. Agglomeration of these defects are known to create vacancy clusters [53]. These more complex defects prevent movement of dislocations and sliding of basal planes causing a significant hardening and increase of the Young's modulus.

FEM simulations of the deformation of the graphite disc are performed to infer beam-induced changes of the Young's modulus. In a first step, the thermal input of Figure 5.1 a) is used on a pristine disc. The velocity and the corresponding FFT spectrum in the centre of the rear side of the disc with free boundary conditions are shown in Figure 5.6 c) and d). An oscillation with a frequency of  $5.32 \pm 0.02$  kHz is obtained, similar to the calculated value using equation 3.20 and measured with the LDV on the pristine sample. A small additional signal is observed at a frequency of  $\sim 22$  kHz which can be attributed to the second order bending mode and causes the fine-structure visible at the initial maxima and minima of the velocity signal.

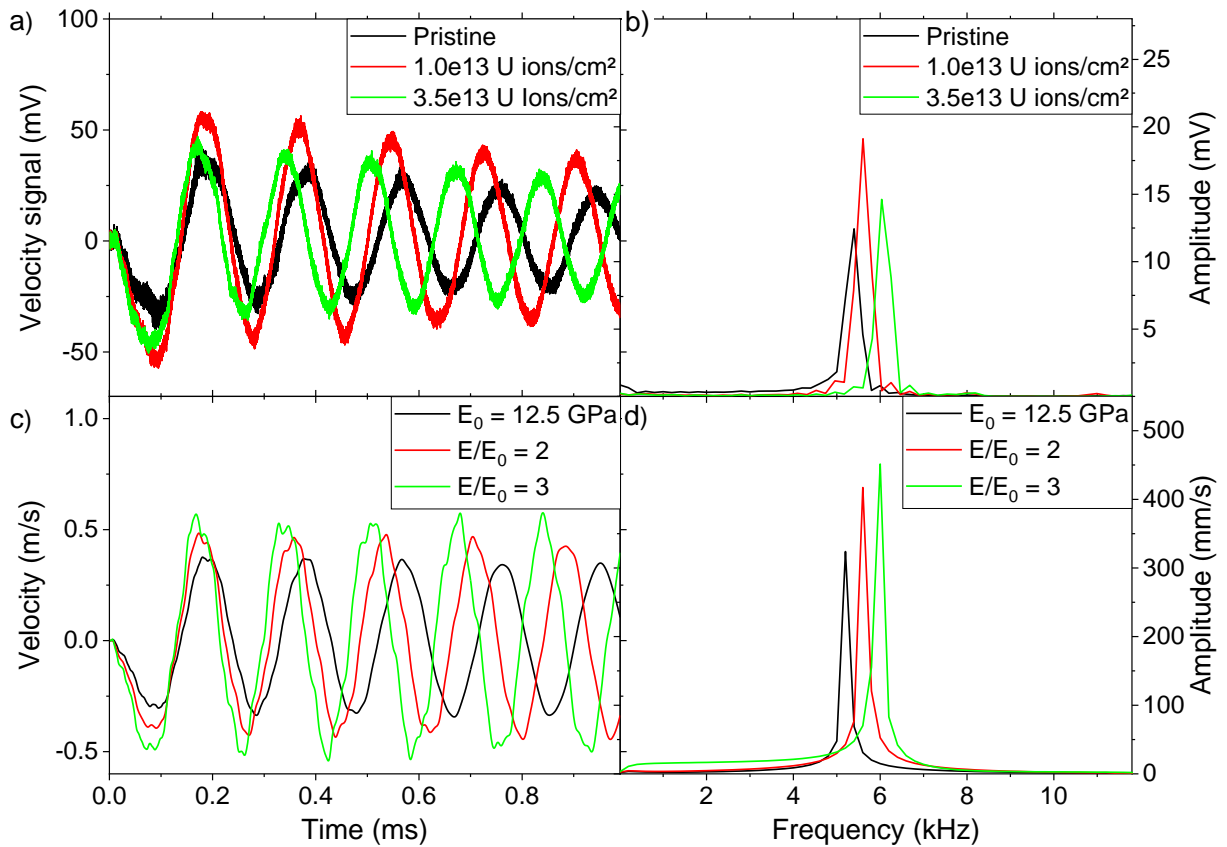


Figure 5.6: a) Time dependent velocity signal measured by LDV and b) corresponding FFT spectra at the rear side of a 0.5 mm thick isotropic R6650 graphite disc for the irradiation with 4.8 MeV/u U ions at different fluences. Corresponding FEM simulations: c) time dependent velocity and d) FFT spectra for the impact of a 100  $\mu$ s U ions pulse (power density 3 MW/cm<sup>3</sup>). Depicted are simulations of a pristine sample (black) and samples with values of Young modulus 2 (red) and 3 (green) times higher than the pristine value as well as thermal conductivity degradation from 95 W/m·K (pristine graphite) to 11 W/m·K ( $E/E_0 = 2$ ) and 4 W/m·K ( $E/E_0 = 3$ ), respectively [8], in the heated volume.

In a second step, FEM simulations of discs with larger Young's modulus in the beam spot are conducted. In Figure 5.6 c) and d) examples of the velocity in the centre of the rear side of discs with 2 and 3 times the pristine Young's modulus are shown. The properties of the part outside the beam spot are assumed to stay constant since the temperature increase is not high enough to significantly change the properties (as seen in Figure 5.1). The frequency spectra of the LDV recordings at different fluences can now be compared with the frequency results of the FEM simulations as demonstrated in Figure 5.7 a) for 2 and 3 times the pristine Young's modulus. The frequencies for those two simulations are measured in the LDV signal at accumulated fluences of  $1.5 \times 10^{13}$  and  $3.3 \times 10^{13}$  ions/cm<sup>2</sup>. The same procedure is used to estimate a continuous development of the Young's modulus depending on the fluence as shown in Figure

5.7 b). Important requirements for this method, are the proper knowledge of the pristine material parameters, the geometry of the sample and its boundary conditions and no large-scale defects due to the irradiation such as cracks.

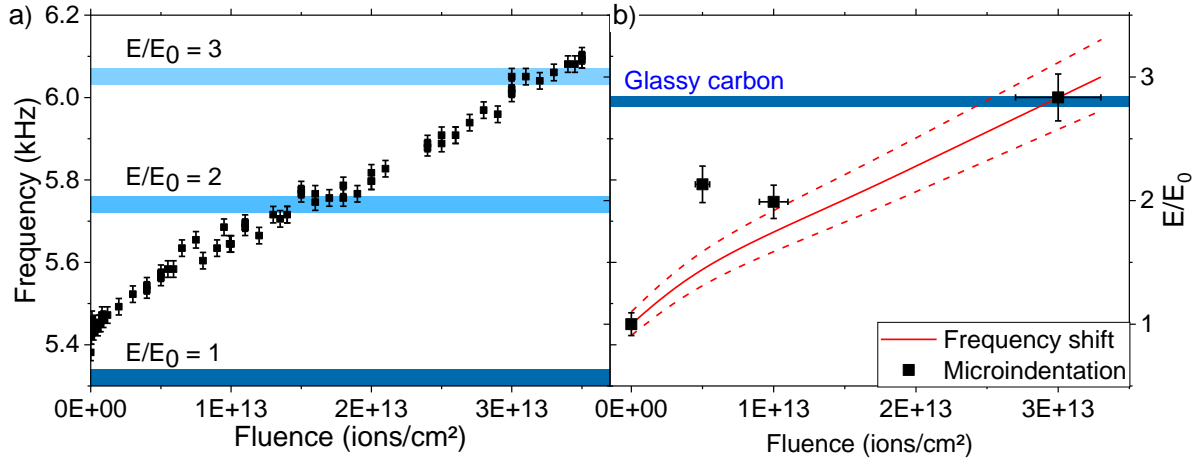


Figure 5.7: a) Measured bending frequency of isotropic SGL R6650 graphite as a function of accumulated 4.8 MeV/u U ion fluence. Shaded areas represent the frequencies obtained by FEM simulations with pristine properties as well as with 2 and 3 times the pristine Young's modulus in the beam spot. The uncertainty of the frequencies of 0.02 kHz is obtained by the frequency resolution of the FFT. b) Relative increase of the Young's modulus as a function of the U ion fluence measured by microindentation and deduced from simulations of frequency shifts of LDV velocity signals. The shaded blue area represents the ratio of the Young's modulus between the glassy carbon grade HTW Sigradur K and SGL R6650 taken from the data sheets.

To test the validity of this method, the deduced Young's modulus values are compared to microindentation measurements on the sample series shown in Figure 4.6. The sample itself could not be used for microindentation since the large diameter to thickness ratio resulted in a slight bending of the sample preventing the required contact for indentation experiments. From the good agreement in the investigated fluence range, it can be concluded that the LDV online measurements method provides realistic results for beam-induced changes of the Young's modulus for isotropic graphite. This is excellent news, because it reduces the need to irradiate samples series with different accumulated fluences and avoids uncertainties due to property fluctuations between several samples. Both methods show a large increase up to about 3 times the pristine Young's modulus  $E_0$  for irradiation with a fluence of  $3 \times 10^{13}$  U ions/cm². The obtained increase is similar to the ratio of the Young's moduli of glassy carbon [30] and SIGRAFINE R6650 [19] of 2.8. This supports the assumption that

intensive ion irradiation induces a transition towards a disordered structure similar to glassy carbon [8,61]. Compared to neutron irradiation, the effects of heavy ion irradiation are much more severe. The fluences achieved in this study correspond to less than 0.01 dpa as calculated by SRIM Kinchin and Pease damage calculation [41,127]. Several tens of dpa are necessary for similar changes induced by neutron irradiation [56,62,63].

Besides the large amplitude caused by the bending of the sample, also elastic or plastic transversal stress waves are expected at a pulse length of 100  $\mu\text{s}$  and a deposited power of approximately 3 MW/cm<sup>3</sup> [128]. These transversal waves propagate along the disc axis and according to the values calculated in equation 3.21, appear in the MHz frequency regime. A colour plot for the continuous wavelet transform coefficients for the first dynamic response obtained for a pristine isotropic graphite target is shown in Figure 5.8. A wave number of  $k = 20$  provided the best trade-off between frequency and temporal resolution.

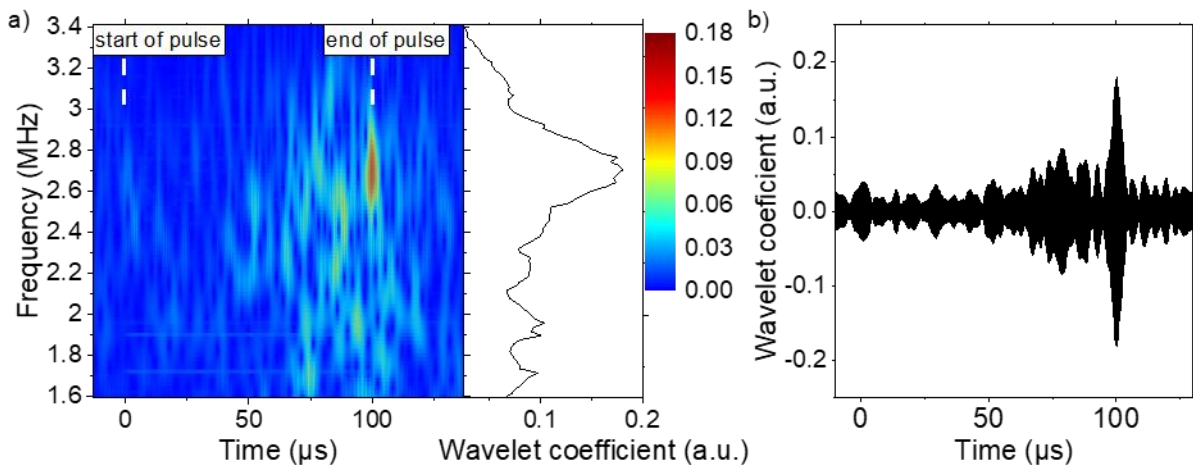


Figure 5.8: a) Contour plot of the absolute wavelet coefficient (in a.u.) determined with a Morlet wavelet with a wave number of  $k = 20$  as a function of time and frequency and maximum wavelet coefficient from the entire depicted time span depending on the frequency. Shown is the frequency range around the expected value for transversal stress waves (2.73 MHz). b) time dependent wavelet coefficient at 2.70 MHz. Both graphs show the impact of the first 4.8 MeV/u U ion pulse on pristine isotropic graphite.

The highest wavelet coefficient appears at a frequency of  $2.70 \pm 0.02$  MHz, very close to the calculated frequency of 2.73 MHz. This signal corresponds to an elastic stress wave as the pressure wave propagates at the speed of sound [129]. The yield strength of graphite is not reached and hardly any plastic deformation occurs. This supports the

---

hypothesis that the sample properties outside the beam spot are not changed as inserted in the FEM simulations. The maximum of the wavelet coefficient is obtained at the end of the pulse of 100  $\mu$ s. At this point the highest values of temperature and velocity are reached, resulting in the highest thermal stress. After the end of the beam pulse, the temperature difference decreases and the stress wave signal is rapidly damped. Smaller maxima are visible at lower frequencies. These can be caused due to sample roughness leading to slightly larger path lengths.

---

## 5.4 Carbon fibre reinforced carbon

---

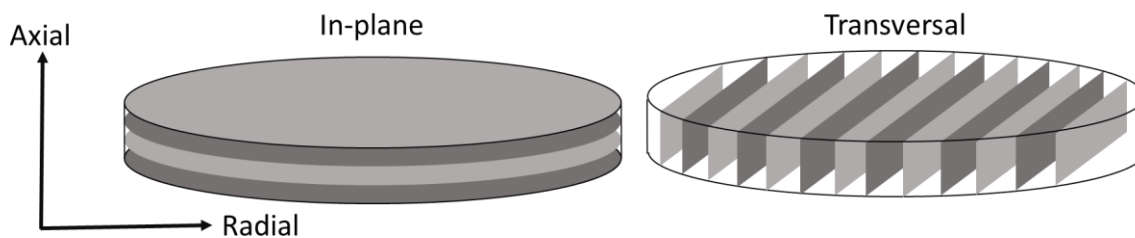


Figure 5.9: Scheme of the fibre plane orientation of in-plane and transversal orientation of the investigated 2D CFCs with marked axial and radial directions.

Carbon fibre reinforced carbon is an anisotropic material leading to different Young's moduli and shear moduli depending on the orientation of the fibre planes. However, for the case of a thin disc investigated in this work, the Kirchhoff-Love theory uses only the radial properties of the discs and neglects the small influence of the properties in axial direction. In the case of CFC, the in-plane orientation of carbon fibre reinforced carbon has its fibre planes parallel to the sample surface leading to homogenous properties within this plane (cf. Figure 5.9). Neglecting the different properties in the transversal direction, the bending frequencies can be calculated by only one Young's modulus.

In case of SGL Premium investigated in this section, the Young's modulus is not available from the data sheets. However, by measuring the bending frequency the pristine Young's modulus can be calculated. The beam-induced velocity signal of two discs with different dimensions ((1) 2 cm diameter and 0.53 mm thickness and (2) 1 cm diameter and 0.21 mm thickness) is measured with the LDV to test if similar Young's

moduli are obtained. Figure 5.10 shows the velocity signal and the corresponding FFT spectra of a 0.53 mm thick SGL Premium disc with a diameter of 2 cm and a beam spot with a diameter of 6 mm. The first measurement is recorded at a fluence of  $2 \times 10^{11}$  ions/cm<sup>2</sup>. As seen in Figure 4.14, the mechanical properties at this fluence are still very similar to the pristine properties. A rapidly damped signal with a main frequency of  $11.48 \pm 0.02$  kHz is obtained. Using equation 3.20, this bending frequency corresponds to a Young's modulus of  $46 \pm 2$  GPa in case of free boundary conditions. With increasing U ion fluence the frequency slightly increases up to  $11.75 \pm 0.02$  kHz for a fluence of  $4 \times 10^{13}$  ions/cm<sup>2</sup> which is ascribed to an increase of the Young's modulus.

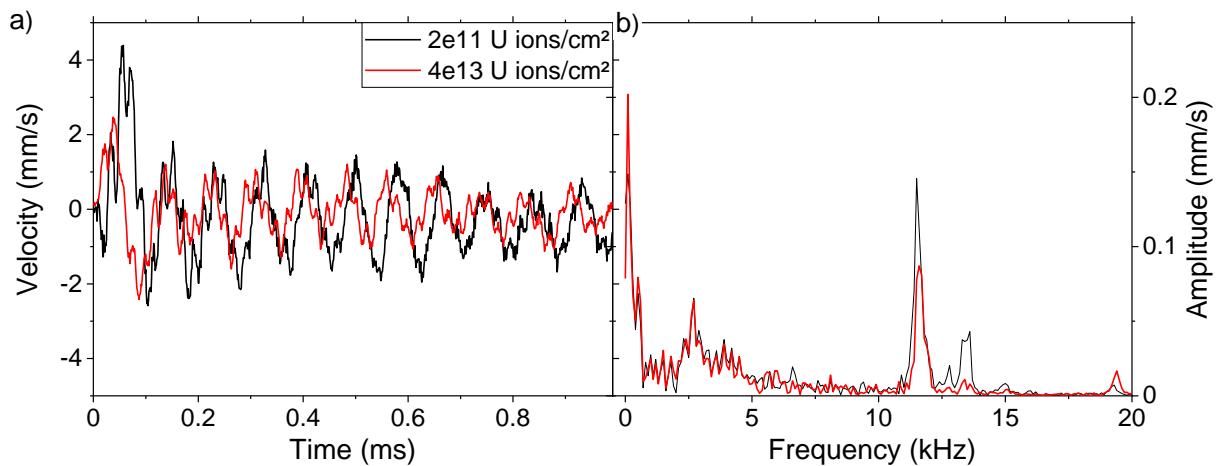


Figure 5.10: a) Time dependent velocity signal measured by LDV and b) corresponding FFT spectra at the rear side of a 0.53 mm thick SGL Premium disc in-plane orientation with a diameter of 2 cm for the irradiation with 4.8 MeV/u U ions at lowest and highest investigated fluence.

Figure 5.11 shows the velocity signal and the corresponding FFT spectra of a 0.21 mm thick SGL Premium disc with a diameter of 1 cm completely irradiated by the U ion beam. It is noted that the initial direction of the sample movement switches during the irradiation for both sample dimensions. While the 2 cm diameter disc initially moves towards the beam (negative) at low fluence and away from the beam (positive) at higher fluences, the 1 cm diameter disc has the opposite effect. It is clear that this behaviour must be related to the specific material as these effects are not observed for isotropic graphite or the metals. Movement towards the beam is expected for samples with a positive coefficient of thermal expansion (CTE) as the front of the sample is heated, while movement away from the beam is expected for samples with a negative

CTE. Highly oriented materials such as HOPG or carbon fibres have a negative CTE parallel to the graphitic planes. However, it is not clear why the two samples behave differently and show such different behaviour during irradiation.

The smaller thickness, smaller radius and larger beam spot results in a larger part of the 1 cm diameter sample exposed to the beam. This leads to a larger amplitude and a less noisy signal with only one prominent frequency at  $17.96 \pm 0.02$  kHz. Using equation 3.20, a Young's modulus of  $45 \pm 2$  GPa is obtained for free boundary conditions. This shows good agreement with the 2 cm diameter disc and supports the validity of the determination of the Young's modulus.

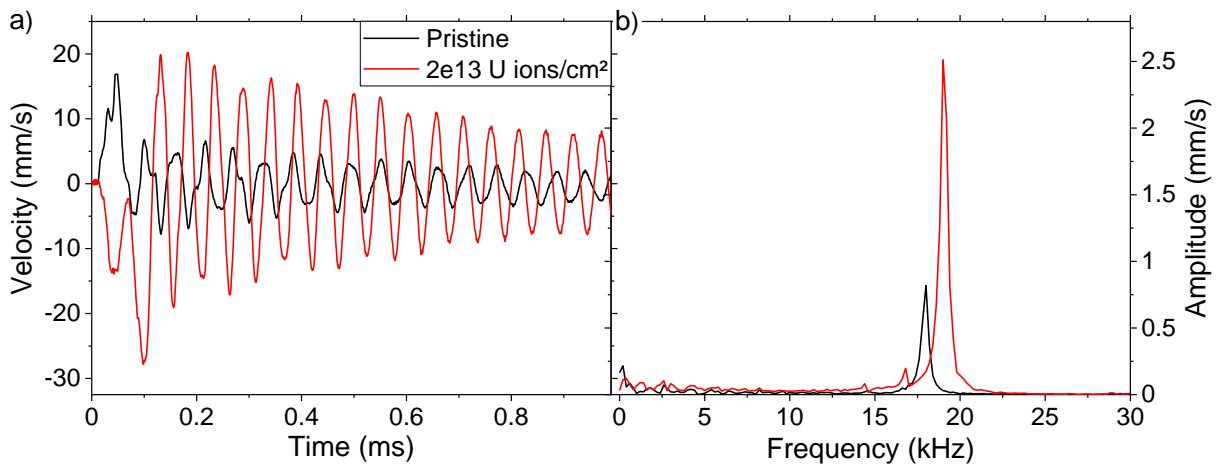


Figure 5.11: a) Time dependent velocity signal measured by LDV and b) corresponding FFT spectra at the rear side of a 0.21 mm thick SGL Premium disc in in-plane orientation with a diameter of 1 cm for the irradiation with 4.8 MeV/u U ions of the pristine sample and at high fluence.

With increasing U ion fluence, the bending frequency of the 1 cm diameter disc reaches  $19.08 \pm 0.02$  kHz at a fluence of  $2.2 \times 10^{13}$  ions/cm<sup>2</sup>. As observed for isotropic graphite and measured by microindentation, an increase of the Young's modulus occurs after U ion impact. Using FEM simulations of a disc with this given sample geometry and a Young's modulus of  $45 \pm 2$  GPa, a frequency of 17.8 kHz is obtained in accordance with the calculated frequency. Figure 5.11 shows that in order to fit the experimental value, an increase of the pristine Young's modulus in the beam spot by a factor of approximately 1.4 times is required to match the experimental bending frequency of  $19.08 \pm 0.02$  kHz as obtained at the highest investigated fluence of  $2.2 \times 10^{13}$  ions/cm<sup>2</sup>. Compared to the Young's modulus from microindentation of

SGL Premium irradiated with 4.8 MeV/u Au ions, the LDV provides a clearer trend without the scattering observed by microindentation. While microindentation measurements strongly depend on which parts of the fibre bundles are hit, the measurements of the bending frequency provide a signal from the complete sample.

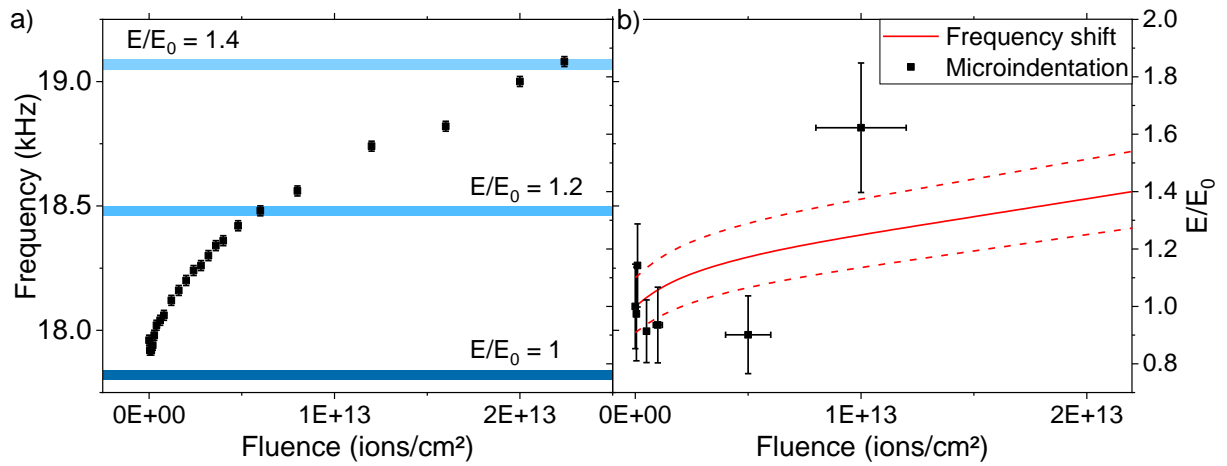


Figure 5.12: a) Measured bending frequency of a 0.21 mm thick SGL Premium disc in in-plane orientation with a diameter of 1 cm as a function of accumulated 4.8 MeV/u U ion fluence. The blue horizontal lines indicate FEM simulations with pristine properties as well as with 1.2 and 1.4 times the pristine Young's modulus in the beam spot. The frequency uncertainty of 0.02 kHz is due to the frequency resolution of the FFT. b) Relative increase of the Young's modulus as a function of the ion fluence measured by microindentation (black data) and deduced from simulations of frequency shifts of LDV velocity signals (red solid line with uncertainties indicated by dashed line).

Figure 5.13 shows the velocity signal and the corresponding FFT spectra of the transversal orientation of SGL Premium. The diameter of the sample is 1 cm and the thickness 0.57 mm. The bending frequency cannot be calculated by the Kirchhoff-Love theory as there are different Young's modulus depending on whether the direction aligns with the fibre plane. Moreover, the shear moduli are not available from the data sheet. As observed for the 1 cm diameter disc of the in-plane orientation, the pristine sample initially moves away from the beam indicating a negative CTE. With increasing fluence the initial movement is reversed in the direction towards the beam. The FFT spectra show several peaks induced by additional bending modes generated by the lack of rotational symmetry within the sample. The largest peak for the pristine sample occurs at a frequency of  $36.35 \pm 0.02$  kHz which is most likely caused by a bending mode without nodal radii or diameters, similar to the first order bending mode of the samples shown previously (e.g., Figure 5.11).

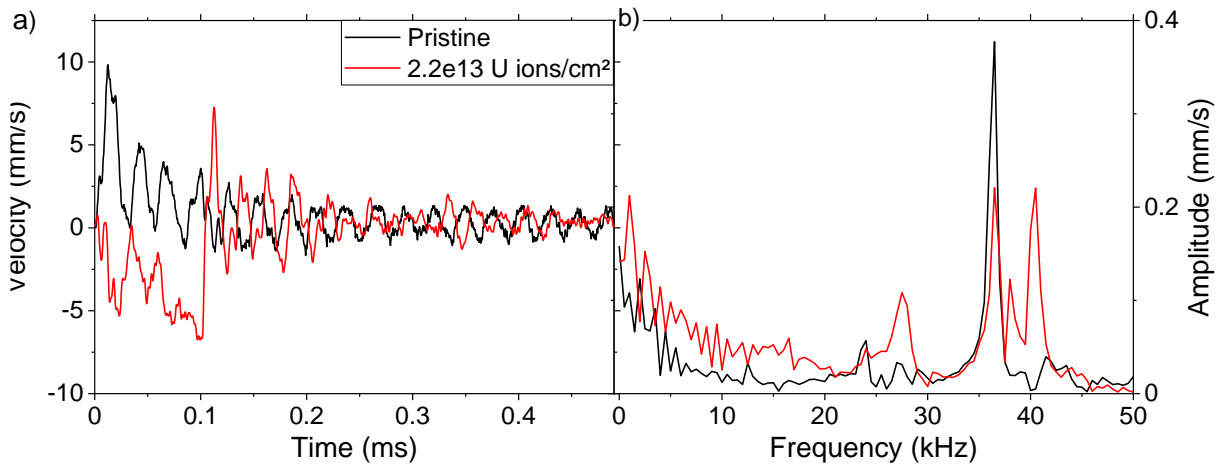


Figure 5.13: a) Time dependent velocity signal measured by LDV and b) corresponding FFT spectra at the rear side of a 0.57 mm thick SGL Premium disc in transversal orientation with a diameter of 1 cm for the irradiation with 4.8 MeV/u U ions of the pristine sample and at high fluence.

## 5.5 Flexible graphite

Velocity signal and corresponding FFT spectra of a 150  $\mu\text{m}$  thick flexible graphite disc with a diameter of 2 cm are shown in Figure 5.14. The beam spot is circular with a diameter of 6 mm. Similar to CFC the initial velocity is positive i.e. the surface moves away from the beam indicating a negative CTE. For the quasi-pristine sample, a frequency of  $3.57 \pm 0.02$  kHz is obtained. Using the values from the data sheet [33] with a Young's modulus of  $E = 0.7$  GPa and equation 3.20, yields a first order bending frequency of 0.56 kHz. Such a large frequency difference cannot be caused by non-free binding conditions or inaccuracy of the geometry measurement as both would result in a much smaller discrepancy. It is assumed that either the Young's modulus is incorrect and/or the observed peak is not the first order bending mode. Flexible graphite is anisotropic due to high orientation of the graphitic planes after the rolling process. As only the Young's modulus in the radial directions of the disc is relevant for the bending frequency, which is the direction within the graphitic planes, the actual Young's modulus could be higher. To obtain a first order bending frequency of  $3.57 \pm 0.02$  kHz a Young's modulus of 29 GPa would be required. This seems unreasonable as it is close to the Young's modulus of a single crystal of graphite and larger than the values obtained for HOPG (see Figure 4.4 and [130]). However, assuming the peak not to be caused by the first order bending mode, but the second

order bending mode would only require a Young's modulus of 1.6 GPa. This assumption is supported by the additional peak observed at  $8.27 \pm 0.02$  kHz. Which is due to the third order bending mode which expected at a frequency of 8.2 kHz. The first order bending mode might not be measurable due to the short measurement time, limited by the damping of the vibration of the sample.

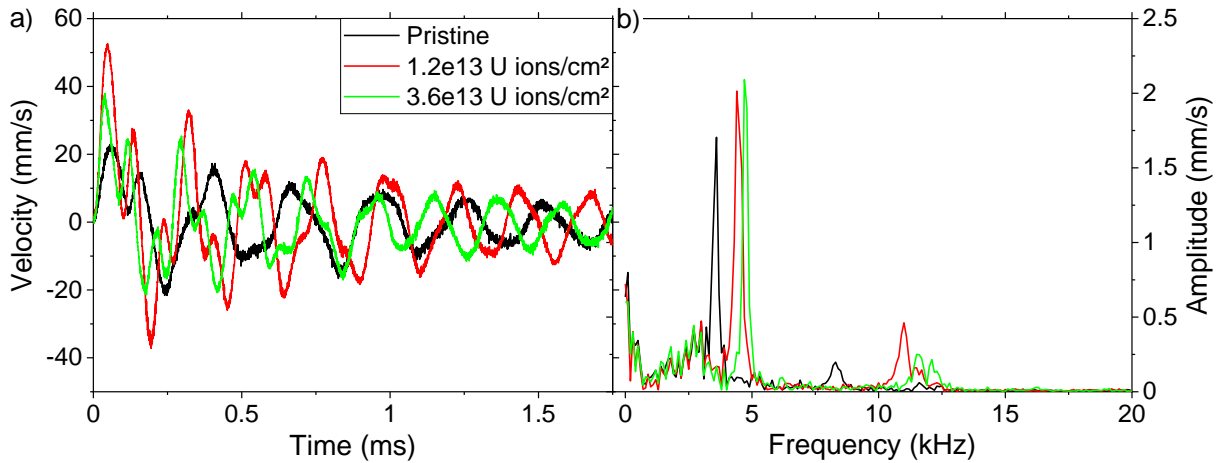


Figure 5.14: Time dependent velocity signal measured by LDV and b) corresponding FFT spectra at the rear side of a 0.15 mm thick isotropic SGL Sigraflex disc with a diameter of 2 cm for the irradiation with 4.8 MeV/u U ions of the pristine sample and at different fluences.

With increasing fluence the frequency of the peak at  $3.57 \pm 0.02$  kHz increases to  $4.74 \pm 0.02$  kHz for the highest investigated fluence of  $4 \times 10^{13}$  ions/cm<sup>2</sup> as illustrated in Figure 5.15. Furthermore, the frequency of the peak at  $8.27 \pm 0.02$  kHz increases to  $11.55 \pm 0.02$  kHz. These changes are caused by the increase of the Young's modulus within the beam spot. Prosvetov [6] showed by means of Raman spectroscopy that ion beam-induced damage in flexible graphite follows the nuclear energy loss and not the electronic energy loss. This leads to defect accumulations mainly at the end of the ion range. Accordingly, the assumption of homogenous property changes within the beam spot used for the FEM simulations of PG and CFC cannot be upheld. Quantitative analysis of the Young's modulus changes cannot be performed as the depth dependence of the Young's modulus is not accessible.

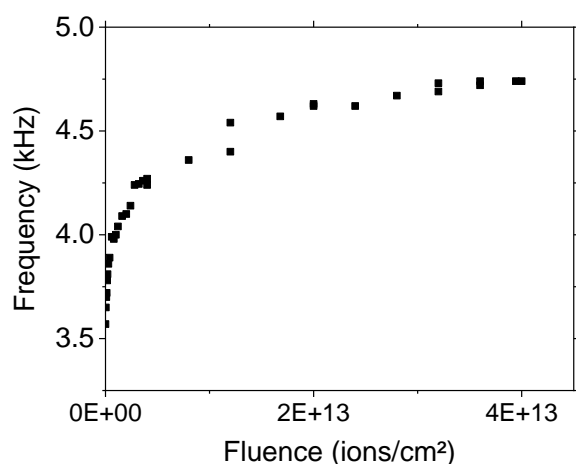


Figure 5.15: Measured bending frequency of a 0.15 mm thick isotropic SGL Sigraflex disc with a diameter of 2 cm as a function of accumulated 4.8 MeV/u U ion fluence.

---

## 5.6 Glassy carbon

---

Results of the 4.8 MeV/u U ion pulse irradiation of a 0.27 mm thick glassy carbon disc with a diameter of 1 cm and a beam spot covering the complete sample are shown in Figure 5.16. For the pristine sample the measured harmonic oscillation with a frequency of  $23.5 \pm 0.1$  kHz agrees well with the calculated first order bending frequency of 24.0 kHz and the simulated frequency of 24.4 kHz. The difference between the calculation and the simulation can be explained by the simplification of the Kirchhoff-Love theory (Equations 3.11 to 3.20) which considers the disc as a 2D object neglecting axial contributions. For the ratio of thickness to diameter of the glassy carbon sample this simplification leads to a slight overestimation of the calculated frequency.

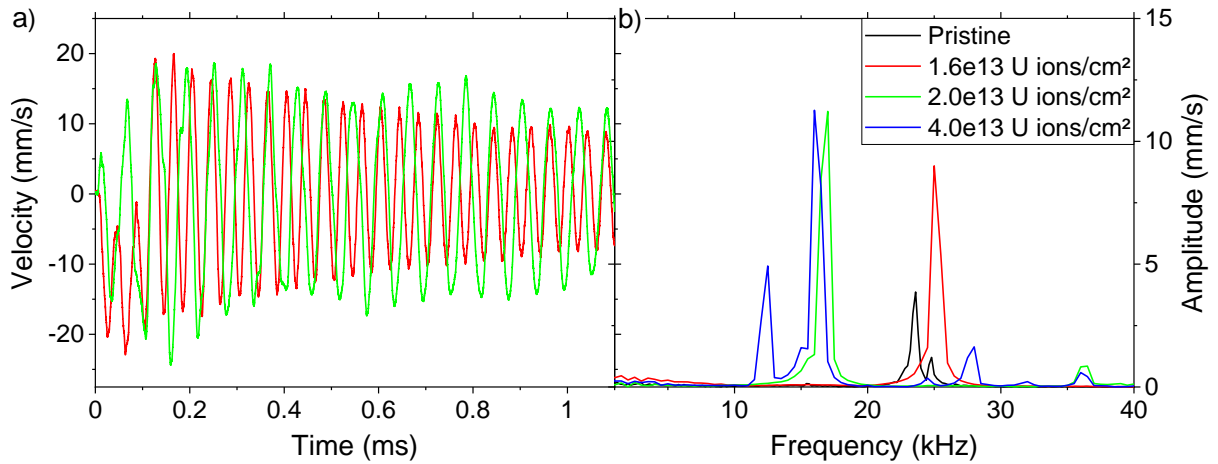


Figure 5.16: a) Time dependent velocity signal measured by LDV and b) corresponding FFT spectra at the rear side of a 0.27 mm thick Sigradur G disc with a diameter of 1 cm for the irradiation with 4.8 MeV/u U ions at different fluences. The velocity signals of the pristine sample and irradiated to a fluence of  $4 \times 10^{13}$  ions/cm<sup>2</sup> are not shown for better view.

Under the irradiation with 4.8 MeV/u U ions the most dominant frequency shifts from initially  $23.5 \pm 0.1$  kHz to  $25.1 \pm 0.1$  kHz at a fluence of  $1.6 \times 10^{13}$  ions/cm<sup>2</sup>. Between  $1.6 \times 10^{13}$  ions/cm<sup>2</sup> and  $2.0 \times 10^{13}$  ions/cm<sup>2</sup> a sudden jump of the frequency to  $16.8 \pm 0.1$  kHz occurred which only slightly shifts to a slightly lower frequency for the remaining irradiation up to  $4.0 \times 10^{13}$  ions/cm<sup>2</sup>. In addition, the second order bending mode is observed at a frequency of  $\sim 36$  kHz.

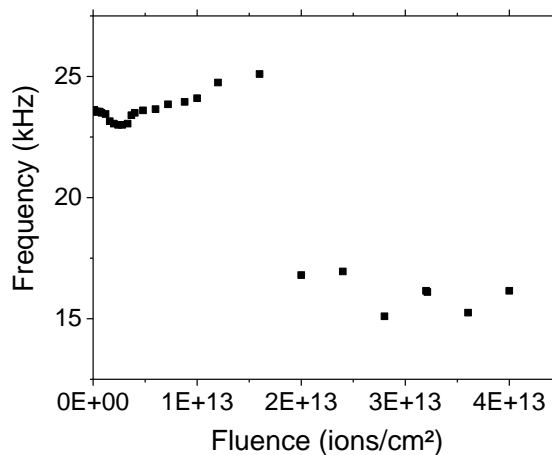


Figure 5.17: Measured bending frequency of a 0.27 mm thick Sigradur G disc with a diameter of 1 cm as a function of accumulated 4.8 MeV/u U ion fluence.

During optical inspection of the sample after irradiation with  $4 \times 10^{13}$  ions/cm<sup>2</sup>, chipping of the face exposed to the U ion beam is detected (Figure 5.18). The top layer breaks into small flakes with lose contact to the underlying layer. These fractured pieces no

---

longer contribute to the main bending mode with the consequence that the thickness of the sample is effectively reduced leading to a lower frequency. In a first approximation, it is assumed that a layer is removed across the entire sample. The frequency of  $16.8 \pm 0.1$  kHz observed at  $2.0 \times 10^{13}$  ions/cm<sup>2</sup> would correspond to a sample thickness of 190  $\mu$ m. This corresponds to a removed layer of 80  $\mu$ m which is slightly larger than the ion penetration depth of  $\sim 60$   $\mu$ m. However, this is only a rough estimate since the sample is not damaged across the entire surface (Figure 5.18) and fractured pieces are not fully removed. For the highest achieved fluence of  $4 \times 10^{13}$  ions/cm<sup>2</sup> two additional peaks appear at  $\sim 12$  and  $\sim 28$  kHz. It is assumed that these frequencies are also related to the damaged character of the irradiated surface. Once chipped pieces are removed, the damage process continuous on the freshly exposed layer. Moreover, the sample disc loses rotational symmetry resulting in additional bending modes that can be activated, which can however not be ascribed exactly due to damaged sample condition.

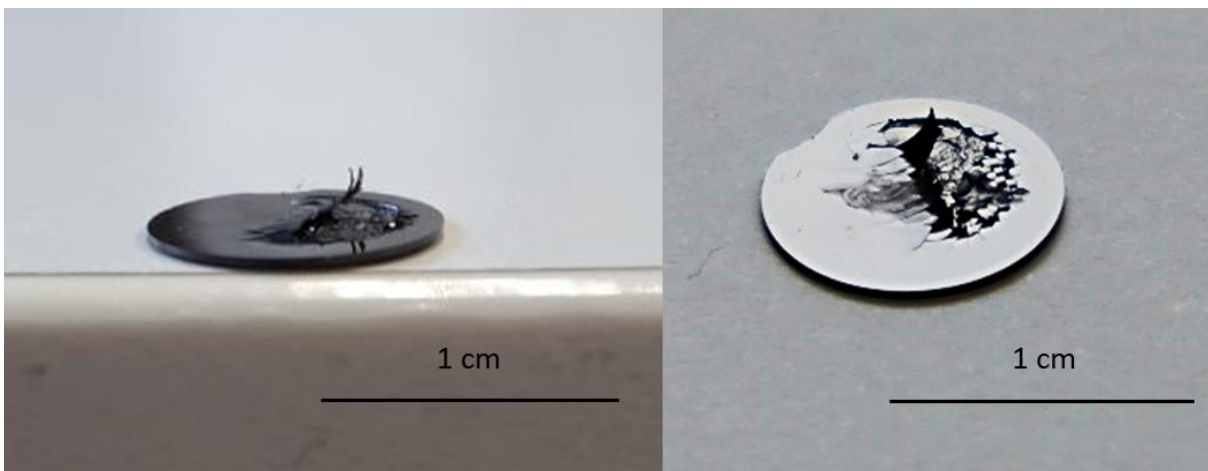


Figure 5.18: Side (left) and top (right) view of the Sigradur G sample after irradiation with 4.8 MeV/u U ions to an accumulated fluence of  $4 \times 10^{13}$  ions/cm<sup>2</sup>. Radiation damage leads to fragmentation of the irradiated layer which finally detaches from the underlying non-irradiated substrate.

---

## 5.7 Hexagonal boron nitride

---

Isotropic hexagonal BN has a similar structure as graphite. However, its polar bonding results in a lower resistance to crack propagation. LDV velocity signals and corresponding FFT spectra measured at the rear side of a 0.5 mm thick sample with a

diameter of 2 cm and a square beam spot with an area of 1x1 cm<sup>2</sup> are shown in Figure 5.19. Similar to the measurement of isotropic graphite the voltage signal could not be converted to velocity and the raw voltage signal is presented. At a low fluence of 4x10<sup>11</sup> ions/cm<sup>2</sup> a bending frequency of 9.5 ± 0.1 kHz is measured. According to the calculation (Equation 3.20), a frequency of 10.1 kHz corresponds to a bending mode for a fixed sample. FEM simulations with a fixed support at the outer 1 mm rim show fair agreement of the waveform with the measured velocity signals as presented in Figure 5.20.

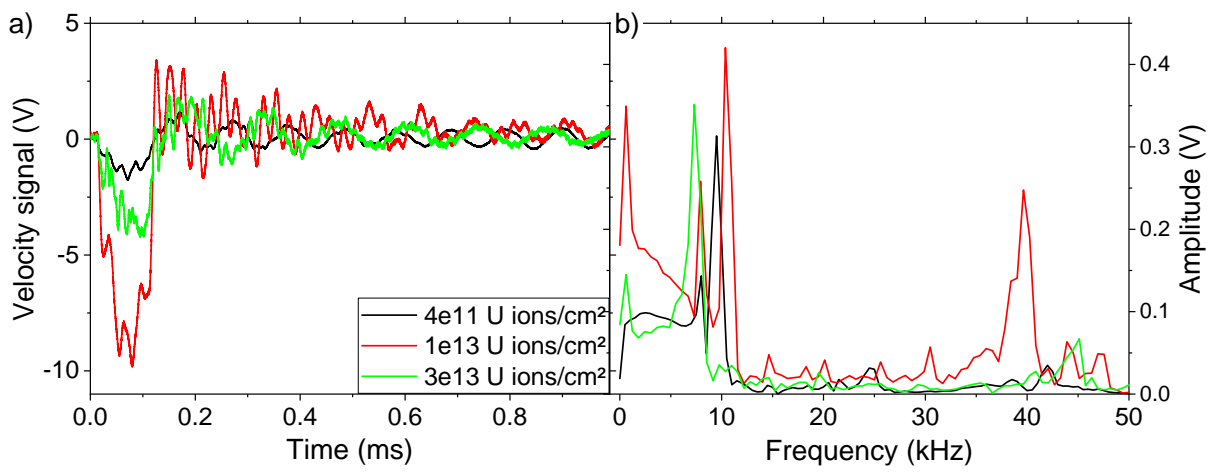


Figure 5.19: a) Time dependent velocity signal measured by LDV and b) corresponding FFT spectra measured at the rear side of a 0.5 mm thick h-BN disc with a diameter of 2 cm under irradiation with 4.8 MeV/u U ions at different fluences.

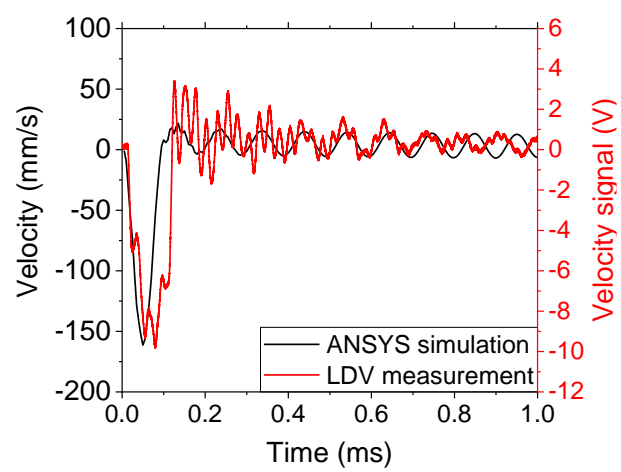


Figure 5.20: Time dependent velocity signal measured by LDV at the rear side of a 0.5 mm thick h-BN disc with a diameter of 2 cm at an accumulated fluence of 1x10<sup>13</sup> ions/cm<sup>2</sup> (red) and FEM simulation (black) using h-BN properties.

Figure 5.21 shows the development of the bending frequency as a function of fluence in the frequency range around 10 kHz (a) and 40 kHz (b). The low frequency signal remains rather stable at about 9.5 kHz up to  $2 \times 10^{12}$  ions/cm<sup>2</sup> and then increases to 10.6 kHz for  $1 \times 10^{13}$  ions/cm<sup>2</sup>. For higher fluences, the signal fluctuates irregularly.

In the high frequency regime, a new double-peak signal appears at a fluence of  $2 \times 10^{12}$  ions/cm<sup>2</sup> with centres at  $38.4 \pm 0.1$  and  $39.4 \pm 0.1$  kHz (Figure 5.19 b). These frequencies remain stable up to a fluence of  $1 \times 10^{13}$  ions/cm<sup>2</sup>. With further fluence increase (Figure 5.21 b)) a fluctuation of high-frequency peaks in the FFT spectra similar to those in the low frequency regime occurs. These frequency effects are ascribed to the formation of cracks ( $>2 \times 10^{12}$  ions/cm<sup>2</sup>) and finally to the complete detachment of the beam-exposed central part of the sample ( $>1 \times 10^{13}$  ions/cm<sup>2</sup>).

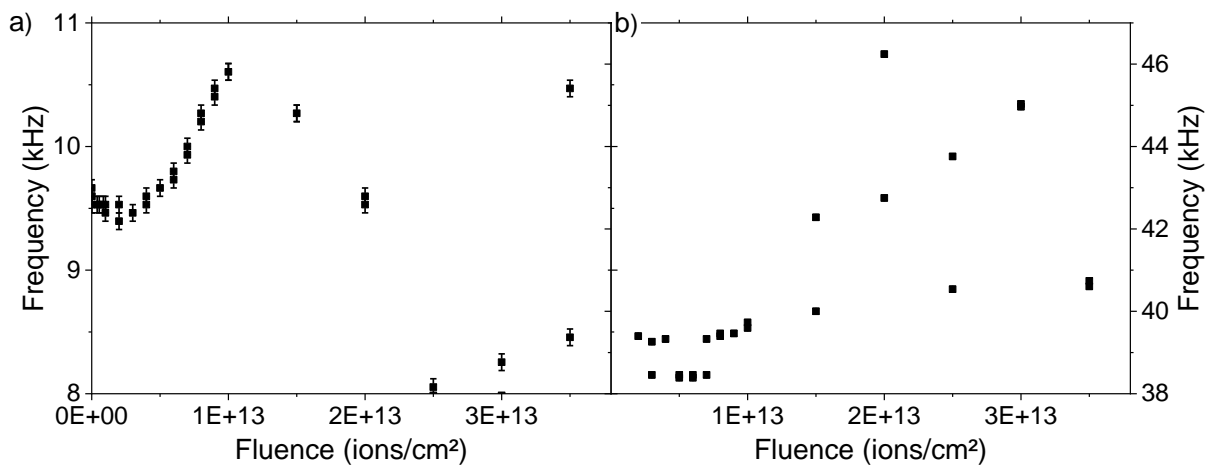


Figure 5.21: Measured frequency of the bending mode assigned to a) the entire sample and b) the detached central part of a 0.5 mm thick h-BN disc with a diameter of 2 cm as a function of accumulated 4.8 MeV/u U ion fluence. The uncertainty of the frequencies given by the limited frequency resolution of the FFT is smaller than the size of the symbols in b).

This assumption is supported by the observation during dismounting of the irradiated sample, where a round piece of 8-9 mm in diameter completely detached from the rest of the sample is identified (Figure 5.22). The fracture piece shows pronounced bending which is probably due to beam-induced swelling. Based on this one sample, quantitative evaluation of this effect is not possible.

By using equation 3.20 for a sample diameter of 8.5 mm, which is the average diameter of the detached central part of the h-BN target, a free bending frequency of 39.0 kHz is calculated, fitting well the measured frequencies. The appearance of two peaks is

ascribed to the non-circular shape of the detached piece. Using the same method as for graphite, indicates that a Young's modulus of approximately 4 times the value of the pristine sample is required to reproduce the experimentally observed frequency changes observed at a fluence of  $1 \times 10^{13}$  ions/cm<sup>2</sup>. For a detached sample piece, this should result in even larger changes of the frequency within the beam spot which is not the case (Figure 5.21 b). This indicates that the increase of the low frequency is primarily caused by cracks in the sample and not by an increase of the Young's modulus.

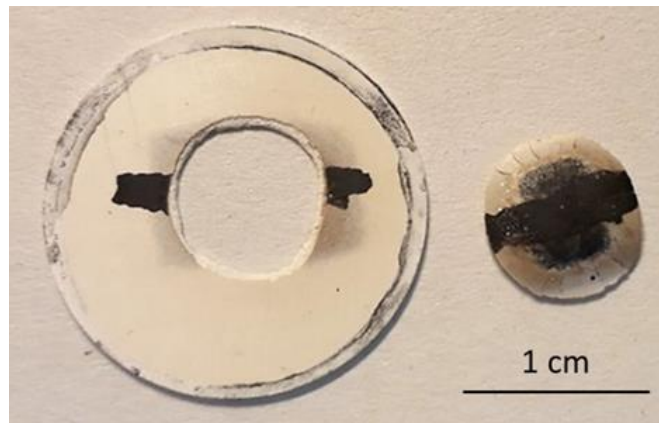


Figure 5.22: 0.5 mm thick h-BN disc with a diameter of 2 cm after irradiation with 4.8 MeV/u U ions to an accumulated fluence of  $5 \times 10^{13}$  ions/cm<sup>2</sup>. The sample fractured around the beam spot area and is visibly bent. The black horizontal line originates from a carbon paint applied for thermal camera monitoring during irradiation.

In contrast to isotropic graphite, visible degradation of irradiated h-BN appears at smaller fluences indicating a lower radiation resistance. While the graphitic samples kept their shape and integrity, h-BN shows a visible deformation which eventually results in cracking and fragmentation of the structure. First failure signs are visible in the velocity and FFT signals at fluences as low as  $2 \times 10^{12}$  ions/cm<sup>2</sup>. The damage effect becomes more pronounced at higher fluences as shown for the signal at a fluence of  $1 \times 10^{13}$  ions/cm<sup>2</sup>. While h-BN was demonstrated to be stable under continuous proton irradiation [131], the larger energy loss and the pulsed structure of the U ion beam results in stress concentration profiles appearing at the interface between irradiated and pristine material leading to crack formation. Due to the brittle nature of h-BN, the irradiated part of the target finally detaches from the sample even though the penetration depth of the ion beam is only about one tenth of the sample thickness.

## 6 Conclusions

The irradiation of various graphitic materials with swift heavy ions above a critical energy loss of approximately 18 keV/nm results in significant property changes. This includes a large decrease of the crystallite size and a phase transformation towards a structure similar to glassy carbon.

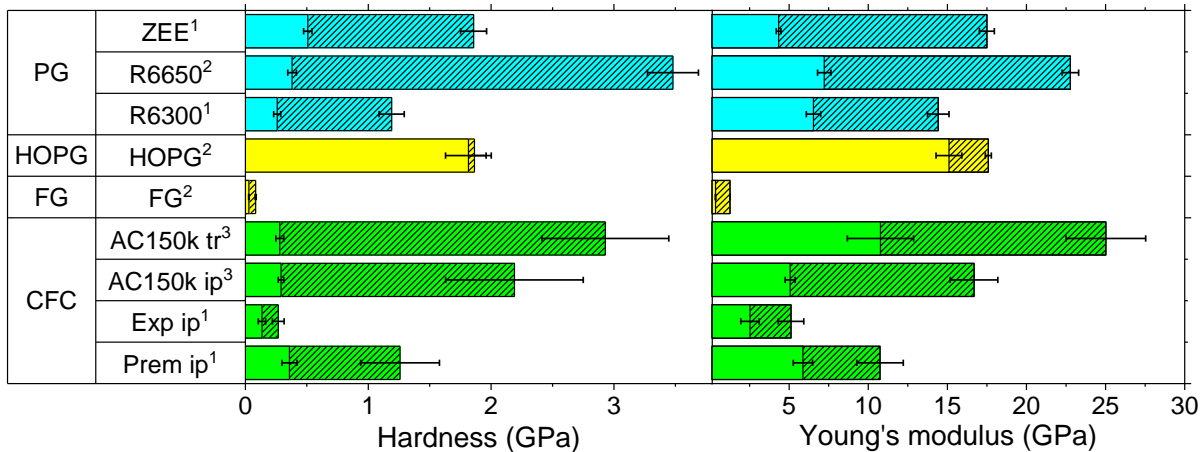


Figure 6.1: Hardness and Young's modulus of pristine (plane coloured bars) and irradiated (plane plus striated coloured bars) graphitic materials. The bars show the properties at the highest investigated Au ion fluences (<sup>1</sup>  $5 \times 10^{13}$  ions/cm<sup>2</sup>, 4.8 MeV/u; <sup>2</sup>  $7 \times 10^{13}$  ions/cm<sup>2</sup>, 4.8 MeV/u; <sup>3</sup>  $2 \times 10^{14}$  ions/cm<sup>2</sup>, 3.6 MeV/u).

Microindentation shows that beam-induced structural modifications significantly change the mechanical properties (Figure 6.1). The Young's modulus of the polycrystalline isotropic graphite (PG) grade SGL R6650 increases by up to 300 % and the hardness rises by more than 1000 % compared to the pristine values at the highest investigated fluences. Radiation-induced effects especially of the hardness are lower for the isotropic graphite grades POCO ZEE and SGL R6300. The values for the carbon fibre reinforced carbon (CFC) grade Tatsuno AC150k increase in a similar order of magnitude, but the changes of the hardness depend on the orientation of the fibres. The radiation effects for samples with fibres oriented normal to the surface (transversal) are more pronounced compared to parallel fibre orientation (in plane). The ion-induced change of the Young's modulus of SGL Premium (Prem) and SGL Experimental Premium (Exp) is lower compared to AC150k or the PG grades. These CFC grades can be a good option for applications where mechanical property changes

---

need to be avoided. Flexible graphite (FG) has low values before and after irradiation and due to its low density and excellent thermal properties it could be the best option for applications as beam dumps. Highly oriented pyrolytic graphite (HOPG) has the lowest changes of the investigated materials. However, its high brittleness and anisotropic properties prevents its use in most applications which require high mechanical strength.

To investigate the response to the pulsed beam conditions of future accelerator facilities, irradiated isotropic graphite and carbon fibre reinforced carbon were tested by nanoimpact measurements providing strain rates at the surface of up to  $\sim 10^4$  1/s, similar to the strain rates expected for pulsed ion beams. As nanoimpact measurements of pristine graphite are not available in the literature, isotropic graphite was systematically investigated by varying impact parameters such as the indenter tip, the acceleration force and the acceleration distance. With increasing strain rate, linear trends of the transferred kinetic energy are obtained indicating no strain-rate dependence of the pristine materials. The dynamic hardness shows a larger indentation size effect than obtained for the quasi-static hardness determined by microindentation. However, for impacts with an incoming energy of more than 500 nJ, corresponding to a depth of 5  $\mu\text{m}$ , pristine isotropic graphite has a stable hardness with similar values as the quasi-static hardness measurements.

The nanoimpact investigation of irradiated samples yield results that are more similar to the Young's modulus than to the quasi-static hardness, both in maximum increase and sensitivity to the ion fluence. Elastic properties are relevant regarding the amount of energy repulsed during the impact. Furthermore, the obtained dynamic hardness could be reduced due to a higher brittleness caused by the irradiation. To test the brittleness of the irradiated material micropillar compression would be desirable.

An indication for a larger brittleness is observed during multiple impulse measurements. The failure probability of the isotropic graphite grade SGL R6650 is initially decreasing with increasing ion fluence due to the hardening of the materials. However, for irradiations above the energy loss threshold using a fluence of  $7 \times 10^{13}$  ions/cm<sup>2</sup>, the behaviour is reversed and the failure probability rises again.

---

To provide safe operation conditions and estimate the life time of beam intercepting devices, the large increase of the Young's modulus and of the brittleness needs to be taken into account when simulating beam conditions and designing components. This is especially true for devices like beam dumps or beam catchers, where the beam is stopped and energy losses in the Bragg peak can be higher than 18 keV/nm for ions with large atomic numbers. However, changes of the mechanical properties also occur for light ions below the energy loss threshold leading to up to 100 % increase. The regime below and above the threshold follow a different dose dependence. Based on these scaling laws, the response to other ions and energy loss values can be extrapolated for future beam simulations. The influence of annealing due to the high temperatures generated during the impact of ion beams remains an open question. While a reduction of the radiation damage at high temperatures is expected, dedicated high temperature indentation experiments should be used for a quantitative evaluation.

To directly investigate the mechanical effects of pulsed beams on targets, discs of graphitic materials as well as metals and hexagonal boron nitride were exposed to U ion pulses with GeV kinetic energy. The dynamic response of the targets was monitored by on-line recording the surface velocity signal at the rear side of the sample using laser Doppler vibrometry. Beam-induced changes of the first order bending frequency of isotropic graphite and carbon fibre reinforced carbon discs allow the determination of the Young's modulus of irradiated material by comparison with FEM simulations. The comparison with microindentation data shows good agreement, suggesting the online method as an interesting alternative to offline measurements using a series of samples that need to be irradiated at different fluences. The observation by continuous wavelet transformation enables the detection of transversal elastic stress waves in isotropic graphite for the investigated pulse intensities of up to  $1 \times 10^{10}$  ions/cm<sup>2</sup> per pulse. In the case of glassy carbon and h-BN, damage formation in the beam spot is evidenced by the formation of new peaks or by a jump of the bending frequency. In contrast, none of these effects could be detected for graphite. Graphite has slow crack growth and self-healing of pre-existing microcracks due to growth in the c-axis direction, leading to higher critical stress values. Moreover, in irradiated graphite stress is accommodated by creep deformation preventing catastrophic failures.

---

This work demonstrates that laser Doppler vibrometry is a suitable tool to monitor failures of beam-exposed devices by early detection of bending frequency changes due to defect formation in materials before catastrophic failures happen. The applicability to devices and other beam conditions needs to be tested both experimentally and by simulations as different geometries and beam intensities have a direct impact on the signal amplitude.

---

## 7 References

---

- [1] H. Geissel, M. Winkler, H. Weick, et al., "Technical Design Report on the Super-FRS" 2008, Available from: <http://repository.gsi.de/record/54552> (3 June 2020).
- [2] N. Tahir, A. Matveichev, V. Kim et al., "Three-dimensional Simulations of a Solid Graphite Target for High Intensity Fast Extracted Uranium Beams for the Super-FRS," *Laser and Particle Beams*, vol. 27, pp. 9–17, 2009.
- [3] N. Tahir, R. Schmidt, M. Brugger et al., "Simulations of Full Impact of the Large Hadron Collider Beam with a Solid Graphite Target," *Laser and Particle Beams*, vol. 27, pp. 475–483, 2009.
- [4] S. Fernandes, F. Pellemoine, M. Tomut et al., "In-situ Electric Resistance Measurements and Annealing Effects of Graphite Exposed to Swift Heavy Ions," *Nuclear Inst. and Methods in Physics Research B*, vol. 314, pp. 125–129, 2013.
- [5] C. Hubert, "Characterization of radiation damage induced by swift heavy ions in graphite," PhD thesis, TU Darmstadt, 2016.
- [6] A. Prosvetov, "Ion-beam induced modifications of structural and thermophysical properties of graphite materials," PhD thesis, TU Darmstadt, 2020.
- [7] F. Pellemoine, M. Avilov, M. Bender et al., "Study on Structural Recovery of Graphite Irradiated with Swift Heavy Ions at High Temperature," *Nuclear Inst. and Methods in Physics Research B*, vol. 365, pp. 522–524, 2015.
- [8] A. Prosvetov, G. Hamaoui, N. Horny et al., "Degradation of Thermal Transport Properties in Fine-grained Isotropic Graphite Exposed to Swift Heavy Ion Beams," *Acta Materialia*, vol. 184, pp. 187–198, 2020.
- [9] J. Habainy, Y. Lee, K.B. Surreddi et al., "Study of Heavy Ion Beam Induced Damage in Tungsten for High Power Target Applications," *Nuclear Inst. and Methods in Physics Research B*, vol. 439, pp. 7–16, 2019.

- 
- [10] K. Kupka, A.A. Leino, W. Ren et al., "Graphitization of Amorphous Carbon by Swift Heavy Ion Impacts: Molecular Dynamics Simulation," *Diam. Relat. Mater.*, vol. 83, pp. 134–140, 2018.
- [11] F. Tuinstra and J.L. Koenig, "Raman Spectrum of Graphite," *The Journal of Chemical Physics*, vol. 53, no.3, pp. 1126–1130, 1970.
- [12] A.C. Ferrari and J. Robertson, "Interpretation of Raman spectra of disordered and amorphous carbon," *Physical Review B*, vol. 61, no.20, pp. 14095–14107, 2000.
- [13] W. Oliver and G. Pharr, "An Improved Technique for Determining Hardness and Elastic Modulus Using Load and Displacement Sensing Indentation Experiments," *J. Mater. Res.*, vol. 7, no.6, pp. 1564–1583, 1992.
- [14] W. Oliver and G. Pharr, "Measurement of Hardness and Elastic Modulus by Instrumented Indentation: Advances in Understanding and Refinements to Methodology," *J. Mater. Res.*, vol. 19, no.1, pp. 3–20, 2004.
- [15] B. Beake, S. Goodes, S. Jones, et al., "NanoTest On-line Help File Version 1.0 and NanoTest Manual Version 3.0" 2004, Available from: <http://www.ipsi.smr.ru/Lab/CKPO/Nanofot/doc/NANOTEST600.pdf> (15.09.20).
- [16] K. Momma and F. Izumi, "VESTA 3 for three-dimensional visualization of crystal, volumetric and morphology data," *J Appl Cryst*, vol. 44, no.6, pp. 1272–1276, 2011.
- [17] M. Inagaki, F. Kang, "Materials science and engineering of carbon," Waltham, MA: Butterworth-Heinemann, 2014.
- [18] SGL Carbon, "SIGRAFINE R6300 data sheet, Available from: <https://www.sglcarbon.com/pdf/SGL-Datenblatt-SIGRAFINE-R6300-DE.pdf> (14 May 2019).
- [19] SGL Carbon, "SIGRAFINE R6650 Data Sheet, Available from: <https://www.sglcarbon.com/pdf/SGL-Datenblatt-SIGRAFINE-R6650-DE.pdf> (3 June 2020).

- 
- [20] POCO, "Speciality materials-industrial applications, Available from: [www.poco.com/Portals/0/Literature/79185v1IndustrialFlyer.pdf](http://www.poco.com/Portals/0/Literature/79185v1IndustrialFlyer.pdf) (14 May 2019).
- [21] L.M. Manocha, "High performance carbon-carbon composites," *Sadhana*, vol. 28, no.1, pp. 349–358, 2003.
- [22] SGL Carbon, "SIGRABOND Premium data sheet, Available from: <https://www.sglcarbon.com/pdf/SGL-Datasheet-SIGRABOND-Premium-EN.pdf> (14.05.19).
- [23] SGL Carbon, "SIGRABOND Experimental data sheet," Personal communication.
- [24] E. Krzyzak, "Status and properties of AC150K composite" 2013, Available from: <https://indico.cern.ch/event/283843/contribution/8/material/slides/0.pptx> (28 April 2017).
- [25] F. Jäger, "Characterization of carbon materials for high power-density beam impact applications," Master thesis, TU Darmstadt, 2018.
- [26] P.J.F. Harris, "Fullerene-like models for microporous carbon," *J Mater Sci*, vol. 48, no.2, pp. 565–577, 2013.
- [27] K. Jurkiewicz, M. Pawlyta, D. Zygadło et al., "Evolution of glassy carbon under heat treatment: correlation structure–mechanical properties," *J Mater Sci*, vol. 53, no.5, pp. 3509–3523, 2018.
- [28] P.J.F. Harris and S.C. Tsang, "High-resolution electron microscopy studies of non-graphitizing carbons," *Philosophical Magazine A*, vol. 76, no.3, pp. 667–677, 1997.
- [29] P.J.F. Harris, "Fullerene-related structure of commercial glassy carbons," *Philosophical Magazine*, vol. 84, no.29, pp. 3159–3167, 2004.
- [30] HTW, "SIGRADUR G Data Sheet, Available from: <http://www.wiyi.com.tw/Download/PDF/Data%20.pdf> (3 June 2020).
- [31] C. Garion, "Mechanical Properties for Reliability Analysis of Structures in Glassy Carbon," *World Journal of Mechanics*, vol. 4, pp. 79–89, 2014.

- 
- [32] I. Structure Probe, "HOPG Advanced Ceramics Brand Grade ZYB, Available from: <https://www.2spi.com/item/430hp-ab/hopg-momentive-performance/> (19 August 2021).
- [33] SGL Carbon, "SIGRAFLEX-Flexible Graphitfolien und Graphitplatten für Hochtemperaturprozesse" 2018, Available from: <https://www.sglcarbon.com/pdf/SGL-Datenblatt-SIGRAFLEX-TH-NH-THP-S-HP-UHP-Folie-DE.pdf> (19 August 2021).
- [34] SGL Carbon, "SIGRAFLEX®Flexible Graphitfolie für industrielle Anwendungen (metrisch)" 2021, Available from: <https://www.sglcarbon.com/pdf/SGL-Datenblatt-SIGRAFLEX-APX2-APX-E-C-Z-Folie-DE.pdf> (19 August 2021).
- [35] Henze Boron Nitride Products, "HeBoSint Data Sheet, Available from: [https://www.henze-bnp.de/PDF/HeBoSint\\_PD\\_D.pdf](https://www.henze-bnp.de/PDF/HeBoSint_PD_D.pdf) (4 May 2017).
- [36] R.B. Appleby, R. Barlow, A. Bertarelli et al., "Collimation System," High-Luminosity Large Hadron Collider (HL-LHC), pp. 109–130, 2017.
- [37] C. L. Torregrosa Martín, "Comprehensive Study for an Optimized Redesign of the CERN's Antiproton Decelerator Target," PhD thesis, Universitat Politècnica de València, 2018.
- [38] R. Garoby, A. Vergara, H. Danared et al., "The European Spallation Source Design," Phys. Scr., vol. 93, no.1, p. 14001, 2017.
- [39] O. S. Brüning, J. Poole, P. Collier, et al., "LHC Design Report," CERN, 2004.
- [40] L. R. Evans (editor), "The Large Hadron Collider" A marvel of technology," 1st ed., Lausanne: EPFL Press, 2009.
- [41] J. Ziegler, M. Ziegler and J. Biersack, "SRIM-the Stopping and Range of Ions in Matter," Nuclear Inst. and Methods in Physics Research B, vol. 268, no.11-12, pp. 1818–1823, 2010.
- [42] M. Lang, F. Djurabekova, N. Medvedev, M. Toulemonde and C. Trautmann, "Fundamental Phenomena and Applications of Swift Heavy Ion Irradiations. In:

---

Konings RJM, Stoller RE (editors). *Comprehensive nuclear materials*. Amsterdam: Elsevier, 2020. p. 485–516.

- [43] J. Lindhard, M. Scharff and H.E. Schiøtt, "Range Concepts and Heavy Ion Ranges (Notes on Atomic Collisions, II)," *Originating Research Org. not identified*, vol. Vol: 33: No. 14, 1963.
- [44] F. Bloch, "Zur Bremsung rasch bewegter Teilchen beim Durchgang durch Materie," *Ann. Phys.*, vol. 408, no.3, pp. 285–320, 1933.
- [45] H. Bethe, "Bremsformel für Elektronen relativistischer Geschwindigkeit," *Z. Physik (Zeitschrift für Physik)*, vol. 76, no.5-6, pp. 293–299, 1932.
- [46] C. Trautmann, "Micro- and Nanoengineering with Ion Tracks. In: Hellborg R (editor). *Ion Beams in Nanoscience and Technology*. 2009th ed. Berlin, Heidelberg: Springer-Verlag Berlin Heidelberg, 2010. p. 369–87.
- [47] M. Toulemonde, E. Paumier and C. Dufour, "Thermal spike model in the electronic stopping power regime," *Radiation Effects and Defects in Solids*, vol. 126, no.1-4, pp. 201–206, 1993.
- [48] M. Toulemonde, W. Assmann, C. Dufour, A. Meftah and C. Trautmann, "Nanometric transformation of the matter by short and intense electronic excitation: Experimental data versus inelastic thermal spike model," *Nuclear Instruments and Methods in Physics Research Section B: Beam Interactions with Materials and Atoms*, vol. 277, pp. 28–39, 2012.
- [49] M. Toulemonde, W. Assmann, C. Dufour, A. Meftah and C. Trautmann, "Experimental phenomena and thermal spike description of ion Tracks in Amorphisable Inorganic Insulators. In: Sigmund P (editor). *Ion beam science: Solved and unsolved problems ; invited lectures presented at a symposium arranged by the Royal Danish Academy of Sciences and Letters, Copenhagen, 1 - 5 May 2006*. Copenhagen: Det Kongelige Danske Videnskabernes Selskab, 2006. p. 263–92.

- 
- [50] J.B. Gibson, A.N. Goland, M. Milgram and G.H. Vineyard, "Dynamics of Radiation Damage," *Phys. Rev.*, vol. 120, no.4, pp. 1229–1253, 1960.
- [51] K. Nordlund, S.J. Zinkle, A.E. Sand et al., "Primary radiation damage: A review of current understanding and models," *Journal of Nuclear Materials*, vol. 512, no.1, pp. 450–479, 2018.
- [52] K. Niwase, "Formation of dislocation dipoles in irradiated graphite," *Materials Science and Engineering: A*, vol. 400-401, pp. 101–104, 2005.
- [53] C. Karthik, J. Kane, D.P. Butt, W.E. Windes and R. Ubic, "In Situ Transmission Electron Microscopy of Electron-beam Induced Damage Process in Nuclear Grade Graphite," *Journal of Nuclear Materials*, vol. 412, pp. 321–326, 2011.
- [54] H.M. Freeman, A.N. Jones, M.B. Ward et al., "On the Nature of Cracks and Voids in Nuclear Graphite," *Carbon*, vol. 103, pp. 45–55, 2016.
- [55] C. Karthik, J. Kane, D.P. Butt, W.E. Windes and R. Ubic, "Neutron Irradiation Induced Microstructural Changes in NBG-18 and IG-110 Nuclear Graphites," *Carbon*, vol. 86, pp. 124–131, 2015.
- [56] T.D. Burchell and W.P. Eatherly, "The Effects of Radiation Damage on the Properties of GraphNOL N3M," *Journal of Nuclear Materials*, vol. 179-181, pp. 205–208, 1991.
- [57] S. Ishiyama, T.D. Burchell, J.P. Strizak and M. Eto, "The effect of high fluence neutron irradiation on the properties of a fine-grained isotropic nuclear graphite," *Journal of Nuclear Materials*, vol. 230, no.1, pp. 1–7, 1996.
- [58] A. Dunlop, G. Jaskierowicz, P.M. Ossi and S. Della-Negra, "Transformation of graphite into nanodiamond following extreme electronic excitations," *Phys. Rev. B*, vol. 76, no.15, 2007.
- [59] J. Liu, R. Neumann, C. Trautmann and C. Müller, "Tracks of swift heavy ions in graphite studied by scanning tunneling microscopy," *Phys. Rev. B*, vol. 64, no.18, p. 4142, 2001.

- 
- [60] C. Hubert, K.O. Voss, M. Bender et al., "Swift Heavy Ion-induced Radiation Damage in Isotropic Graphite Studied by Micro-indentation and In-situ Electrical Resistivity," *Nuclear Inst. and Methods in Physics Research B*, vol. 365, pp. 509–514, 2015.
- [61] I. Manika, J. Maniks, R. Zabels et al., "Nanoindentation and Raman Spectroscopic Study of Graphite Irradiated with Swift <sup>238</sup>U Ions," *Fullerenes, Nanotubes and Carbon Nanostructures*, vol. 20, no.4-7, pp. 548–552, 2012.
- [62] M. Bradford and A. Steer, "A Structurally-based Model of Irradiated Graphite Properties," *Journal of Nuclear Materials*, vol. 381, pp. 137–144, 2008.
- [63] G. Haag, "Properties of ATR-2E Graphite and Property Changes due to Fast Neutron Irradiation," *Berichte des Forschungszentrums Jülich*, no.4183, 2005.
- [64] L.L. Snead, Y. Katoh and K. Ozawa, "Stability of 3-D carbon fiber composite to high neutron fluence," *Journal of Nuclear Materials*, vol. 417, no.1-3, pp. 629–632, 2011.
- [65] S. Sato, A. Kurumada, K. Kawamata and R. Ishida, "Thermal shock resistances and fracture toughnesses of graphites and C/C-composites as plasma-facing first wall components for fusion reactor devices," *Fusion Engineering and Design*, vol. 13, no.2, pp. 159–176, 1990.
- [66] GSI webpage, "Unilac overview, Available from: <https://www.gsi.de/work/beschleunigerbetrieb/beschleuniger/unilac/unilac> (19 August 2021).
- [67] A.C. Ferrari and D.M. Basko, "Raman spectroscopy as a versatile tool for studying the properties of graphene," *Nat Nanotechnol*, vol. 8, no.4, pp. 235–246, 2013.
- [68] A. Merlen, J. Buijnsters and C. Pardanaud, "A Guide to and Review of the Use of Multiwavelength Raman Spectroscopy for Characterizing Defective Aromatic Carbon Solids: from Graphene to Amorphous Carbons," *Coatings*, vol. 7, no.10, p. 153, 2017.

- 
- [69] S. Reich and C. Thomsen, "Raman spectroscopy of graphite," *Philos Trans A Math Phys Eng Sci*, vol. 362, no.1824, pp. 2271–2288, 2004.
- [70] R.J. Nemanich and S.A. Solin, "First- and second-order Raman scattering from finite-size crystals of graphite," *Phys. Rev. B*, vol. 20, no.2, pp. 392–401, 1979.
- [71] A.C. Ferrari and J. Robertson, "Resonant Raman spectroscopy of disordered, amorphous, and diamondlike carbon," *Phys. Rev. B*, vol. 64, no.7, 2001.
- [72] Thomsen and Reich, "Double resonant raman scattering in graphite," *Phys Rev Lett*, vol. 85, no.24, pp. 5214–5217, 2000.
- [73] R.P. Vidano, D.B. Fischbach, L.J. Willis and T.M. Loehr, "Observation of Raman band shifting with excitation wavelength for carbons and graphites," *Solid State Communications*, vol. 39, no.2, pp. 341–344, 1981.
- [74] D.S. Knight and W.B. White, "Characterization of diamond films by Raman spectroscopy," *Journal of Materials Research*, vol. 4, no.2, pp. 385–393, 1989.
- [75] L.G. Cançado, K. Takai, T. Enoki et al., "General equation for the determination of the crystallite size  $L_a$  of nanographite by Raman spectroscopy, 2006.
- [76] L.G. Cançado, A. Jorio, E.H.M. Ferreira et al., "Quantifying defects in graphene via Raman spectroscopy at different excitation energies," *Nano Lett*, vol. 11, no.8, pp. 3190–3196, 2011.
- [77] J. Ribeiro-Soares, M.E. Oliveros, C. Garin et al., "Structural analysis of polycrystalline graphene systems by Raman spectroscopy," *Carbon*, vol. 95, pp. 646–652, 2015.
- [78] M.M. Lucchese, F. Stavale, E.M. Ferreira et al., "Quantifying ion-induced defects and Raman relaxation length in graphene," *Carbon*, vol. 48, no.5, pp. 1592–1597, 2010.
- [79] L.G. Cançado, M. Gomes da Silva, E.H. Martins Ferreira et al., "Disentangling contributions of point and line defects in the Raman spectra of graphene-related materials," *2D Mater.*, vol. 4, no.2, p. 25039, 2017.

- 
- [80] A. Eckmann, A. Felten, A. Mishchenko et al., "Probing the nature of defects in graphene by Raman spectroscopy," *Nano Lett*, vol. 12, no.8, pp. 3925–3930, 2012.
- [81] A. Eckmann, A. Felten, I. Verzhbitskiy, R. Davey and C. Casiraghi, "Raman study on defective graphene: Effect of the excitation energy, type, and amount of defects," *Phys. Rev. B*, vol. 88, no.3, p. 4726, 2013.
- [82] A.C. Ferrari, J.C. Meyer, V. Scardaci et al., "Raman spectrum of graphene and graphene layers," *Phys Rev Lett*, vol. 97, no.18, p. 187401, 2006.
- [83] N. Larouche and B.L. Stansfield, "Classifying nanostructured carbons using graphitic indices derived from Raman spectra," *Carbon*, vol. 48, no.3, pp. 620–629, 2010.
- [84] A. Sadezky, H. Muckenhuber, H. Grothe, R. Niessner and U. Pöschl, "Raman microspectroscopy of soot and related carbonaceous materials: Spectral analysis and structural information," *Carbon*, vol. 43, no.8, pp. 1731–1742, 2005.
- [85] C. Bassez and J. Rouzaud, "Characterization of carbonaceous materials by correlated electron and optical microscopy and Raman microspectroscopy," UR - <https://www.semanticscholar.org/paper/Characterization-of-carbonaceous-materials-by-and-Bassez-Rouzaud/1f772238ff5d1deaf10cc5ebbd9ff16f22fb3fd8>, 1985.
- [86] M. Wojdyr, "Fityk: a general-purpose peak fitting program," *J Appl Cryst*, vol. 43, no.5, pp. 1126–1128, 2010.
- [87] B.D. Beake, S.R. Goodes and J.F. Smith, "Micro-Impact Testing: A New Technique for Investigating Thin Film Toughness, Adhesion, Erosive Wear Resistance, and Dynamic Hardness," *Surface Engineering*, vol. 17, no.3, pp. 187–192, 2001.
- [88] B.D. Beake, S.R. Goodes, J.F. Smith et al., "Investigating the fracture resistance and adhesion of DLC films with micro-impact testing," *Diamond and Related Materials*, vol. 11, no.8, pp. 1606–1609, 2002.

- 
- [89] C. Zehnder, J.-N. Peltzer, J.S.K.-L. Gibson and S. Korte-Kerzel, "High strain rate testing at the nano-scale: A proposed methodology for impact nanoindentation," *Materials & Design*, vol. 151, pp. 17–28, 2018.
- [90] J. M. Wheeler, "Nanoindentation Under Dynamic Conditions," PhD thesis, University of Cambridge, 2009.
- [91] H. Somekawa and C.A. Schuh, "High-strain-rate nanoindentation behavior of fine-grained magnesium alloys," *J. Mater. Res.*, vol. 27, no.9, pp. 1295–1302, 2012.
- [92] J.M. Wheeler and A.G. Gunner, "Analysis of failure modes under nano-impact fatigue of coatings via high-speed sampling," *Surface and Coatings Technology*, vol. 232, pp. 264–268, 2013.
- [93] N.M. Jennett and J. Nunn, "High resolution measurement of dynamic (nano) indentation impact energy: a step towards the determination of indentation fracture resistance," *Philosophical Magazine*, vol. 91, no.7-9, pp. 1200–1220, 2011.
- [94] J.M. Wheeler, J. Dean and T.W. Clyne, "Nano-impact indentation for high strain rate testing: The influence of rebound impacts," *Extreme Mechanics Letters*, vol. 26, pp. 35–39, 2019.
- [95] M. Rueda-Ruiz, B.D. Beake and J.M. Molina-Aldareguia, "New instrumentation and analysis methodology for nano-impact testing," *Materials & Design*, vol. 192, p. 108715, 2020.
- [96] B.D. Beake, S.P. Lau and J.F. Smith, "Evaluating the fracture properties and fatigue wear of tetrahedral amorphous carbon films on silicon by nano-impact testing," *Surface and Coatings Technology*, vol. 177-178, pp. 611–615, 2004.
- [97] A. Bertarelli, "Analytical Study of Axisymmetric Transient Thermal Stresses in Graphite Target Rods for the CNGS Facility," CERN EST-ME Technical Note 2003-005, EDMS383454, 2003.

- 
- [98] A. Bertarelli, E. Berthomé, F. Carra et al., "Dynamic Testing and Characterization of Advanced Materials in a New Experiment at CERN HiRadMat Facility," Proc. IPAC'18, Vancouver, Canada, 2018.
- [99] M. Pasquali, A. Bertarelli, C. Accettura et al., "Dynamic Response of Advanced Materials Impacted by Particle Beams: The MultiMat Experiment," Journal of Dynamic Behavior of Materials, vol. 5, no.3, pp. 266–295, 2019.
- [100] F. Carra, A. Dallochio, A. Bertarelli et al., "Mechanical Engineering and Design of Novel Collimators for HL-LHC," Proc. IPAC 2014, Dresden, Germany, 2014.
- [101] P. Simon, P. Drechsel, P. Katrik et al., "Dynamic Response of Graphitic Targets with Tantalum Cores Impacted by Pulsed 440-GeV Proton Beams," Manuscript submitted for publication, 2020.
- [102] N. Simos, H. Kirk, S. Kahn et al., "Study of Graphite Targets Interacting with the 24 GeV Proton Beam of the BNL Muon Target Experiment," Proceedings of EPAC, Paris, France, pp. 2709–2711, 2012.
- [103] R. Wilfinger, A. Kelic, B. Achenbach et al., "Study of Thermal Stress Waves Induced by Relativistic Heavy-Ion Beams," GSI Scientific Report 2007, p. 75, 2008.
- [104] E.H. Love, "The small free vibrations and deformation of a thin elastic shell," Phil. Trans. R. Soc. Lond. A, vol. 179, pp. 491–546, 1888.
- [105] A. Leissa, "Vibration of Plates," Columbus, Ohio: NASA SP-160, 1969.
- [106] R.C. Colwell and H.C. Hardy, "The frequencies and nodal systems of circular plates," The London, Edinburgh, and Dublin Philosophical Magazine and Journal of Science, vol. 24, no.165, pp. 1041–1055, 1937.
- [107] S.Y. Lin, "Coupled Vibration and Natural Frequency Analysis of Isotropic Cylinders or Disks of Finite Dimensions," Journal of Sound and Vibration, vol. 185, no.2, pp. 193–199, 1995.

- 
- [108] J. Morlet, G. Arens, E. Fourgeau and D. Glard, "Wave propagation and sampling theory—Part I: Complex signal and scattering in multilayered media," *Geophysics*, vol. 47, no.2, pp. 203–221, 1982.
- [109] J. Morlet, G. Arens, E. Fourgeau and D. Giard, "Wave propagation and sampling theory—Part II: Sampling theory and complex waves," *Geophysics*, vol. 47, no.2, pp. 222–236, 1982.
- [110] ANSYS mechanical user's guide—release 19.2," Personal communication ANSYS Inc., 2019.
- [111] O.H. Crawford, "Directional effects on the motion of swift ions in anisotropic media," *Phys. Rev. A*, vol. 42, no.3, pp. 1390–1395, 1990.
- [112] J. Halliday and E. Artacho, "Anisotropy of electronic stopping power in graphite," *Phys. Rev. B*, vol. 100, no.10, 2019.
- [113] A. Dallochio, "Study of Thermo-Mechanical Effects Induced in Solids by High Energy Particle Beams: Analytical and Numerical Methods," PhD thesis, Politecnico di Torino, 2008.
- [114] E. Quaranta, "Investigation of collimator materials for the High Luminosity Large Hadron Collider," PhD thesis, Politecnico di Milano, 2017.
- [115] N. Simos, E. Quaranta, N. Charitonidis et al., "Radiation damage of a two-dimensional carbon fiber composite (CFC)," *Carbon Trends*, vol. 3, p. 100028, 2021.
- [116] J.F. Gibbons, "Ion implantation in semiconductors—Part II: Damage production and annealing," *Proceedings of the IEEE*, vol. 60, no.9, pp. 1062–1096, 1972.
- [117] W.J. Weber, "Models and mechanisms of irradiation-induced amorphization in ceramics," *Nuclear Instruments and Methods in Physics Research Section B: Beam Interactions with Materials and Atoms*, vol. 166-167, pp. 98–106, 2000.

- 
- [118] M. Shell De Guzman, G. Neubauer, P. Flinn and W.D. Nix, "The Role of Indentation Depth on the Measured Hardness of Materials," MRS Online Proceedings Library (OPL), vol. 308, 1993.
- [119] M. Sakai and Y. Nakano, "Instrumented pyramidal and spherical indentation of polycrystalline graphite," Journal of Materials Research, vol. 19, no.1, pp. 228–236, 2004.
- [120] W.D. Nix and H. Gao, "Indentation size effects in crystalline materials: A law for strain gradient plasticity," Journal of the Mechanics and Physics of Solids, vol. 46, no.3, pp. 411–425, 1998.
- [121] K. Durst, B. Backes and M. Göken, "Indentation size effect in metallic materials: Correcting for the size of the plastic zone," Scripta Materialia, vol. 52, no.11, pp. 1093–1097, 2005.
- [122] L. Qin, H. Li, X. Shi et al., "Investigation on dynamic hardness and high strain rate indentation size effects in aluminium (110) using nano-impact," Mechanics of Materials, vol. 133, no.4, pp. 55–62, 2019.
- [123] F. Alisafaei, C.-S. Han and S.H.R. Sanei, "On the time and indentation depth dependence of hardness, dissipation and stiffness in polydimethylsiloxane," Polymer Testing, vol. 32, no.7, pp. 1220–1228, 2013.
- [124] B. N. Lucas, W. C. Oliver, G. M. Pharr, J. L. Loubet, "Time dependent deformation during indentation testing," MRS Online Proceedings Library, pp. 233-238, 2011
- [125] P. Bolz, P. Drechsel, A. Prosvetov et al., "Dynamic Radiation Effects Induced by Short-Pulsed GeV U-Ion Beams in Graphite and h-BN Targets," Shock and Vibration, vol. 2021, pp. 1–11, 2021.
- [126] M. Tomut, B. Achenbach, K.H. Behr et al., "Experimental Investigations on Heavy-Ion Induced Radiation Damage of Graphite for the Super-FRS Target and Beam Catchers," GSI Scientific Report 2007, p. 69, 2008.

- 
- [127] R.E. Stoller, M.B. Tiloczko, G.S. Was et al., "On the Use of SRIM for Computing Radiation Damage Exposure," *Nuclear Inst. and Methods in Physics Research B*, vol. 310, pp. 75–80, 2013.
- [128] A. Bertarelli, "Beam-Induced Damage Mechanisms and their Calculation," *CERN Yellow Reports*, vol. 2, p. 159, 2016.
- [129] A. Bertarelli, V. Boccone, F. Carra et al., "Limits for Beam Induced Damage: Reckless or too Cautious?," *Proc. Chamonix 2011 workshop on LHC Performance*, Chamonix, France, pp. 183–188, 2011.
- [130] J. Xiao, L. Zhang, K. Zhou et al., "Anisotropic friction behaviour of highly oriented pyrolytic graphite," *Carbon*, vol. 65, pp. 53–62, 2013.
- [131] N. Simos, Z. Kotsina, D. Sprouster et al., "Hexagonal boron nitride (h-BN) irradiated with 140 MeV protons," *Nuclear Instruments and Methods in Physics Research Section B: Beam Interactions with Materials and Atoms*, vol. 479, pp. 110–119, 2020.

---

## List of figures

---

Figure 2.1: Structure of graphite with the marked unit cell and characteristic atomic distances, created with VESTA software [16].....	4
Figure 2.2: Scheme of fibre planes in CFC with marked directions of the surface of samples with in-plane and transversal orientation.....	7
Figure 2.3: a) Electronic and nuclear energy loss as a function of the specific energy for uranium ions in a carbon target of a density of 1.84 g/cm <sup>3</sup> as calculated with the SRIM-2013 code [41]. b) Energy loss as a function of penetration depth of 4.8 MeV/u U ions in the same target. ....	12
Figure 3.1: Schematic of the UNILAC linear accelerator of GSI adapted from [66]. .	17
Figure 3.2: Schematic of the M3 branch of the UNILAC accelerator of GSI. The beam is marked by a green arrow and possible positions for sample irradiation are marked by blue squares. ....	18
Figure 3.3: Sample holder with four graphitic samples on four positions (S1-S4) designated for experiments in the oven chamber. The holder can be moved in transversal direction to irradiate all four positions subsequently without opening the chamber. ....	18
Figure 3.4: Energy levels of elastic (Rayleigh) and inelastic (Stokes and anti-Stokes) light scattering. ....	21
Figure 3.5: Schematic representation of the vibration modes responsible for the G and D band.....	22
Figure 3.6: Background corrected Raman spectra (black) of isotropic graphite R6650. a) pristine b) irradiated with 4.8 MeV/u Au ions to a fluence of 3×10 <sup>13</sup> ions/cm <sup>2</sup> c) irradiated with 4.8 MeV/u U ions to a fluence of 7×10 <sup>13</sup> ions/cm <sup>2</sup> . Included are the deconvoluted Gaussian/Lorentzian peak fittings (G band in red, D band in orange, other bands in blue) and their sum in green. ....	23

Figure 3.7: Load as a function of depth of an indentation experiment of isotropic R6650 graphite. Marked are the maximum load $P_{max}$ and the initial unloading slope $S$ .	27
Figure 3.8: Schematic set-up of the nanoindentation platform of the NanoTest Vantage produced by Micro Materials. Adapted from [15].	29
Figure 3.9: Depth and velocity signal of a dynamic hardness measurement on pristine isotropic R6650 graphite. A Berkovich indenter tip is accelerated at 38 s from a distance of $\sim 10 \mu\text{m}$ to the sample surface with a force of 50 mN. Marked are the maximum and the residual penetration depth ( $h_{max}$ and $h_{res}$ ), and the incoming and outgoing velocity ( $v_{in}$ and $v_{out}$ ) of the indenter during the first impact.	31
Figure 3.10: Strain rate as a function of depth of the first nanoimpact on pristine isotropic R6650 graphite impacted with a Berkovich indenter. The initial distance is $10 \mu\text{m}$ and the acceleration force 50 mN. The red line represents a fit to the initial data. The black dotted line is at 50 nm where the strain rate is determined to compare between measurements with different impact parameters.	32
Figure 3.11: Multiple impulse experiment for isotropic R6650 graphite with 38 cycles. A Berkovich indenter tip is accelerated from a distance of $\sim 3 \mu\text{m}$ to the sample surface with a force of 30mN. Failure of the material can be observed after 32 cycles indicated by a non-linear increase of the depth vs. time evolution (red cycle).	34
Figure 3.12: a) Sample holder with two graphite samples mounted above a luminescence screen and b) schematic set-up for online monitoring of elastic waves on the rear side of the irradiated samples by a laser Doppler vibrometer (LDV). The temperature on both sample surfaces is monitored with a thermal camera. The experiments are conducted at the M3 beamline at UNILAC.	36
Figure 3.13: Illustration of determination of wavelet coefficients. (Top) Morlet wavelet function with $k = 5$ , $a = 1$ and $b = 1$ and a sinusoidal signal generated with a) fitting and b) non-fitting frequency. Product of the wavelet function and the signal with c) fitting and d) not-fitting frequency. The product is integrated leading to a positive	

wavelet coefficient for the fitting frequency and a wavelet coefficient of 0 for the non-fitting frequency.....	42
Figure 3.14: Schematic drawing in side and front view of a quarter of a simulated target disc with the plane of the disc oriented in x- and y-direction and the thickness in z-direction. All units are in mm. Note that the z-direction is not drawn to scale for better view. The quadratic beam spot is marked in red.....	43
Figure 3.15: Typical mesh used in the Finite element method solver Ansys for a sample with 2 cm diameter and 0.5 mm thickness with a radial element size of 0.5 mm and an axial size of 0.05 mm. The beam spot where the energy is deposited is marked in red and is ~1/10th of the sample thickness. ....	44
Figure 4.1: Raman spectra (top) of pristine glassy carbon grades Sigradur G and K and (bottom) of isotropic R6650 graphite irradiated with different fluences of 4.8 MeV/u Au ions (left) and 4.8 MeV/u Xe ions (right). In all spectra the intensities are normalized to the G band.....	46
Figure 4.2: Intensity of a) D band, b) D3 band and d) 2D band normalized to the G band and c) Full width half maximum of the G band for isotropic R6650 graphite as a function of the ion fluence. Yellow and dark and light grey bands indicate the respective values of pristine R6650 and glassy carbon Sigradur K and G.....	47
Figure 4.3: (Top) Semi-log presentation of depth dependence of electronic and nuclear energy loss of 4.8 MeV/u Au ions in carbon with a density of 2.25 g/cm <sup>3</sup> calculated using SRIM 2013 code [41]. (Bottom) Ratio of the intensity of the D band to the G band of HOPG irradiated with 4.8 MeV/u Au ions to a fluence of 1×10 <sup>12</sup> ions/cm <sup>2</sup> .....	49
Figure 4.4: Hardness and Young's modulus of pristine graphitic materials obtained by microindentation measurements to a depth of 10 μm. ....	50
Figure 4.5: Depth signal of an indentation measurement for isotropic R6650 graphite, both pristine and irradiated with 4.8 MeV/u Au ions to a fluence of 7×10 <sup>13</sup> ions/cm <sup>2</sup> . ....	51

Figure 4.6: Relative change of hardness (left) and Young's modulus (right) of isotropic R6650 graphite as a function of ion fluence (top) and dose (bottom). Yellow and dark and light grey bands indicate respective the values of pristine R6650 and glassy carbon Sigradur K and G. ....	53
Figure 4.7: Relative change of a) hardness and b) Young's modulus of isotropic R6650 graphite as a function of surface energy loss calculated with SRIM 2013 code [41] at a fluence of $1 \times 10^{13}$ ions/cm <sup>2</sup> . The dark grey band indicates the values of pristine SGL R6650. ....	54
Figure 4.8: Relative change of a) hardness and b) Young's modulus for the isotropic graphite grades R6650, R6300 and ZEE as a function the 4.8 MeV/u Au ion fluence. The dark grey band indicates the values of the pristine graphite grades (the width of the band corresponds to the largest error of the three grades). ....	55
Figure 4.9: Relative change of a) hardness and b) Young's modulus of the in-plane orientation of the carbon fibre reinforced carbon grade AC150k as a function of ion fluence. Yellow, dark and light grey bands indicate the values of unirradiated AC150k and glassy carbon Sigradur K and G, respectively.....	56
Figure 4.10: Relative change of a) hardness and b) Young's modulus of the transversal orientation of the carbon fibre reinforced carbon grade AC150k as a function of the ion fluence. Yellow, dark and light grey bands indicate the values of unirradiated AC150k and Sigradur K and G, respectively.....	57
Figure 4.11: Relative change of a) hardness and b) Young's modulus of the carbon fibre reinforced carbon grade AC150k as a function of the surface energy loss. The dark grey band indicates the values of pristine AC150k (the width of the band corresponds to the largest error of the two orientations).....	57
Figure 4.12: Targeted indentation of a fibre and the matrix of the CFC grade AC150k irradiated with 4.8 MeV/u U ions to a fluence of $1 \times 10^{12}$ ions/cm <sup>2</sup> . The figure is composed of two optical microscope images required to focus on the matrix and the fibre (within the white frame) positioned deeper within a pore. Hardness (above	

---

the line) and Young's modulus (beyond the line) values in GPa attributed to the fibres are marked in red, values attributed to the matrix are marked in black. ... 58

Figure 4.13: Relative change of a) hardness and b) Young's modulus fibres and matrix of the carbon fibre reinforced carbon grade AC150k as a function the ion fluence. The dark grey band indicates the values of the pristine matrix and fibres with the larger respective error. .... 59

Figure 4.14: Relative change of a) hardness and b) Young's modulus of the in-plane orientation of various carbon fibre reinforced carbon grades (Premium, Experimental Premium and AC150k) as a function of the ion fluence. SGL Premium and Experimental Premium are irradiated with 4.8 MeV/u Au ions and AC150k with 3.6 MeV/u Au ions. The dark grey band indicates the values of the pristine CFC grades (the width of the band corresponds to the largest error of the three grades). .... 60

Figure 4.15: Relative change of a) hardness and b) Young's modulus of flexible graphite and highly oriented pyrolytic graphite as a function of ion fluence. The dark grey band indicates the values of pristine FG and HOPG (the width of the band corresponds to the largest error of the two materials). .... 61

Figure 4.16: Depth dependence of a) hardness and b) Young's modulus of HOPG irradiated with 4.8 MeV/u Au ions to a fluence of  $1 \times 10^{12}$  ions/cm<sup>2</sup>. The uncertainty of the depth is estimated to be 10 %. .... 62

Figure 4.17: Relative change of a) hardness and b) Young's modulus of graphitic materials as a function of fluence of 4.8 MeV/u Au ions for PG (SGL R6650), FG and HOPG and 3.6 MeV/u Au ion fluence for transversal (tr) and in-plane (ip) orientation CFC (Tatsuno Ac150k). The dark grey band indicates the values of the pristine materials (the width of the band corresponds to the largest error of the investigated materials). .... 63

Figure 4.18: Relative change of a) hardness and b) Young's modulus of isotropic graphite with increasing 4.8 MeV/u U and Au ion fluence. Solid lines represent the



respective Poisson's fits (Equation 4.1) with  $\sigma$  and  $H_{max}$  (a)) and  $E_{max}$  (b)) as fit parameter. ....64

Figure 4.19: Damage cross section as a function of the energy loss. Results of hardness (red squares) and Young's modulus (green triangles) are compared to previous experimental data for polycrystalline isotropic graphite (PG) deduced from photothermal radiometry (PTR) [6] and for surface tracks in highly oriented pyrolytic graphite (HOPG) investigated by scanning tunnelling microscopy (STM) [59]. The dotted lines represent thermal spike calculations [48]. .....65

Figure 4.20: Strain rate at a depth of 50 nm as a function of kinetic energy on a square root scale of a Berkovich (B) and a cube corner (CC) tip impacting the isotropic graphite grades ZEE, R6650 and R6300. ....66

Figure 4.21: Difference between incoming and outgoing kinetic energy of the first impact as a function of incoming kinetic energy for isotropic graphite grades ZEE, R6650 and R6300 impacted with a Berkovich (B) tip. The solid lines represent linear fits. ....67

Figure 4.22: Difference between incoming and outgoing kinetic energy of the first impact as a function of incoming kinetic energy for isotropic R6650 graphite impacted with a cube corner (CC) and Berkovich (B) tip. The solid lines represent linear fits. ....67

Figure 4.23: Damping constant as a function of incoming kinetic energy for isotropic R6650 graphite impacted with a Berkovich tip with different acceleration forces ranging from 25 to 100 mN in 25mN steps and distances ranging from 2.5 to 20.0  $\mu\text{m}$  in 2.5  $\mu\text{m}$  steps. The same data set is sorted by a) acceleration force and b) initial distance between indenter tip and sample surface. Data of only 4 different initial distances are shown in b) for better view. ....68

Figure 4.24: Damping factor as a function of incoming kinetic energy for isotropic R6650 graphite impacted with a Berkovich tip with different acceleration forces and distances. The shaded area represents the 95 % confidence interval of a linear fit to the entire data set. ....69

Figure 4.25: Damping factor as a function of incoming kinetic energy for isotropic graphite grades ZEE, R6650 and R6300 impacted with a Berkovich tip with different acceleration forces and distances. The shaded areas represent the 95 % confidence intervals of linear fits to the entire data sets of the three graphite grades. ....	70
Figure 4.26: Dynamic hardness as a function of incoming kinetic energy for isotropic graphite grades ZEE, R6650 and R6300 impacted with a Berkovich tip with different acceleration forces and distances. Exponential decay curves are fitted to the corresponding data points as a guide for the eye.....	71
Figure 4.27: Dynamic and static hardness as a function of maximum depth for isotropic R6650 graphite impacted with a Berkovich indenter. ....	72
Figure 4.28: Dynamic hardness and damping factor of pristine graphitic materials obtained by nanoimpact measurement. A Berkovich indenter is accelerated with a force of 50 mN from a distance of 10 $\mu\text{m}$ . ....	73
Figure 4.29: Depth signal of a dynamic hardness measurement for isotropic R6650 graphite, both pristine and irradiated with 4.8 MeV/u Au ions to a fluence of $7 \times 10^{13}$ ions/cm <sup>2</sup> . A Berkovich indenter is accelerated with a force of 50 mN from a distance of 10 $\mu\text{m}$ . ....	74
Figure 4.30: Relative change of a) dynamic hardness and b) damping factor for isotropic R6650 graphite as a function of the fluence for various ion species. A Berkovich indenter is accelerated with a force of 50 mN from a distance of 10 $\mu\text{m}$ . Yellow and dark and light grey bands indicate the respective values of pristine R6650 and glassy carbon Sigradur K and G. ....	75
Figure 4.31: Relative change of a) dynamic hardness and b) damping factor for isotropic graphite grades ZEE, R6650 and R6300 as a function 4.8 MeV/u Au ion fluence. A Berkovich indenter is accelerated with a force of 50 mN from a distance of 10 $\mu\text{m}$ . The dark grey band indicates the values of the pristine isotropic graphite grades with the largest respective error. ....	76

Figure 4.32: Relative change of a) dynamic hardness and b) damping factor of carbon fibre reinforced carbon grades Premium and Experimental Premium as a function the 4.8 MeV/u Au ion fluence and AC150k as a function the 3.6 MeV/u Au ion fluence. A Berkovich indenter is accelerated with a force of 50 mN from a distance of 10  $\mu\text{m}$ . The dark grey band indicates the values of the pristine CFC grades with the largest respective error. ....77

Figure 4.33: Depth as a function of time of multiple impulse measurements of a) isotropic graphite grades ZEE, R6650 and R6300 and b) CFC grades SGL Premium, SGL Premium Experimental in in-plane orientation and AC150k with both orientations. The curves show the average of 20 positions, impacted 40 times with a frequency of 0.25 Hz by a cube corner indenter with an acceleration force of 30 mN from a distance of 3  $\mu\text{m}$ . The 95 % confidence interval of the averaged curves is smaller than  $\pm 0.5 \mu\text{m}$  for the PG grades and  $\pm 1.4 \mu\text{m}$  for the CFC grades (not shown for better view).....78

Figure 4.34: Failure probability depending on the impulse number of a) isotropic graphite grades ZEE, R6650 and R6300 and b) CFC grades SGL Premium, SGL Premium Experimental for in-plane orientation and AC150k for both orientations. ....79

Figure 4.35: Depth as a function of time of multiple impulse measurements for isotropic R6650 graphite irradiated with a) 4.8 MeV/u U, b) 4.8 MeV/u Au, c) 11.1 MeV/u Au and d) 4.8 MeV/u Sm ions to different fluences in ions/cm<sup>2</sup>. The curves show the average of 20 positions, impacted 37 times with a frequency of 0.25 Hz by a cube corner indenter with an acceleration force of 30 mN from a distance of 3  $\mu\text{m}$ . The 95 % confidence interval of the averaged curves is smaller than  $\pm 0.5 \mu\text{m}$  for all samples (not shown for better view). ....80

Figure 4.36: Averaged depth as a function of time of multiple impulse measurements for isotropic R6650 graphite irradiated with different ions to a fluence of  $1 \times 10^{13}$  ions/cm<sup>2</sup> ( $1.1 \times 10^{13}$  ions/cm<sup>2</sup> for 11.1 MeV/u Au irradiation). Samples are impacted 75 times with a frequency of 0.25 Hz by a cube corner indenter with an acceleration force of 30 mN from a distance of 3  $\mu\text{m}$ . The 95 % confidence interval

---

of the averaged curves is smaller than  $\pm 0.5 \mu\text{m}$  for all samples (not shown for better view)..... 81

Figure 4.37: Failure probability for isotropic graphite SGL R6650 irradiated with a) 4.8 MeV/u U, b) 4.8 MeV/u Au, c) 11.1 MeV/u Au and d) 4.8 MeV/u Sm ions to different fluences in ions/cm<sup>2</sup>. A Berkovich indenter is accelerated with a force of 30 mN from a distance of 3  $\mu\text{m}$ . This impact is repeated 75 times at 20 different positions of each sample. Failures are detected as demonstrated in Figure 3.11. .... 82

Figure 5.1: ANSYS simulated time dependent temperature evolution of a 0.5 mm thick isotropic graphite disc for 1 ms after the impact of a 100  $\mu\text{s}$  long U ion pulse. Coordinates are in millimetres and the sample orientation is shown in the inset. All points are at  $x = 0 \text{ mm}$ . More details can be seen in Figure 3.14. a) pristine material b) calculation for graphite of reduced thermal conductivity in the beam spot (4 W/m·K [8] instead of 95 W/m·K) corresponding to graphite irradiated with 4.8 MeV/u U ions to a fluence of  $3 \times 10^{13}$  ions/cm<sup>2</sup>. .... 84

Figure 5.2: a) Time dependent velocity signal measured by LDV and b) corresponding FFT spectra at the rear side of a 0.11 mm thick tungsten disc with a diameter of 2 cm for the irradiation with 4.8 MeV/u U ions at different fluences. The inset in a) shows a zoom-in to the initial 5 ms of the signal. .... 85

Figure 5.3: Measured bending frequency of a 0.11 mm thick tungsten disc with a diameter of 2 cm as a function of accumulated 4.8 MeV/u U ion fluence..... 86

Figure 5.4: a) Time dependent velocity signal measured by LDV and b) corresponding FFT spectra at the rear side of a 0.2 mm thick copper disc with a diameter of 2 cm for the irradiation with 4.8 MeV/u U ions at different fluences. .... 87

Figure 5.5: Measured bending frequency of a 0.2 mm thick copper disc with a diameter of 2 cm as a function of accumulated 4.8 MeV/u U ion fluence..... 87

Figure 5.6: a) Time dependent velocity signal measured by LDV and b) corresponding FFT spectra at the rear side of a 0.5 mm thick isotropic R6650 graphite disc for the irradiation with 4.8 MeV/u U ions at different fluences. Corresponding ANSYS

simulations: c) time dependent velocity and d) FFT spectra for the impact of a 100  $\mu\text{s}$  U ions pulse (power density 3 MW/cm<sup>3</sup>). Depicted are simulations of a pristine sample (black) and samples with values of Young modulus 2 (red) and 3 (green) times higher than the pristine value as well as thermal conductivity degradation from 95 W/m·K (pristine graphite) to 11 W/m·K ( $E/E_0 = 2$ ) and 4 W/m·K ( $E/E_0 = 3$ ), respectively [8], in the heated volume.....89

Figure 5.7: a) Measured bending frequency of isotropic SGL R6650 graphite as a function of accumulated 4.8 MeV/u U ion fluence. Shaded areas represent the frequencies obtained by ANSYS simulations with pristine properties as well as with 2 and 3 times the pristine Young’s modulus in the beam spot. The uncertainty of the frequencies of 0.02 kHz is obtained by the frequency resolution of the FFT. b) Relative increase of the Young’s modulus as a function of the U ion fluence measured by microindentation and deduced from simulations of frequency shifts of LDV velocity signals. The shaded blue area represents the ratio of the Young’s modulus between the glassy carbon grade HTW Sigradur K and SGL R6650 taken from the data sheets. ....90

Figure 5.8: a) Contour plot of the absolute wavelet coefficient (in a.u.) determined with a Morlet wavelet with a wave number of  $k = 20$  as a function of time and frequency and maximum wavelet coefficient from the entire depicted time span depending on the frequency. Shown is the frequency range around the expected value for transversal stress waves (2.73 MHz). b) time dependent wavelet coefficient at 2.70 MHz. Both graphs show the impact of the first 4.8 MeV/u U ion pulse on pristine isotropic graphite. ....91

Figure 5.9: Scheme of the fibre plane orientation of in-plane and transversal orientation of the investigated 2D CFCs with marked axial and radial directions. ....92

Figure 5.10: a) Time dependent velocity signal measured by LDV and b) corresponding FFT spectra at the rear side of a 0.53 mm thick SGL Premium disc in-plane orientation with a diameter of 2 cm for the irradiation with 4.8 MeV/u U ions at lowest and highest investigated fluence.....93

Figure 5.11: a) Time dependent velocity signal measured by LDV and b) corresponding FFT spectra at the rear side of a 0.21 mm thick SGL Premium disc in in-plane orientation with a diameter of 1 cm for the irradiation with 4.8 MeV/u U ions of the pristine sample and at high fluence. .... 94

Figure 5.12: a) Measured bending frequency of a 0.21 mm thick SGL Premium disc in in-plane orientation with a diameter of 1 cm as a function of accumulated 4.8 MeV/u U ion fluence. The blue horizontal lines indicate ANSYS simulations with pristine properties as well as with 1.2 and 1.4 times the pristine Young's modulus in the beam spot. The frequency uncertainty of 0.02 kHz is due to the frequency resolution of the FFT. b) Relative increase of the Young's modulus as a function of the ion fluence measured by microindentation (black data) and deduced from simulations of frequency shifts of LDV velocity signals (red solid line with uncertainties indicated by dashed line). .... 95

Figure 5.13: a) Time dependent velocity signal measured by LDV and b) corresponding FFT spectra at the rear side of a 0.57 mm thick SGL Premium disc in transversal orientation with a diameter of 1 cm for the irradiation with 4.8 MeV/u U ions of the pristine sample and at high fluence. .... 96

Figure 5.14: Time dependent velocity signal measured by LDV and b) corresponding FFT spectra at the rear side of a 0.15 mm thick isotropic SGL Sigraflex disc with a diameter of 2 cm for the irradiation with 4.8 MeV/u U ions of the pristine sample and at different fluences. .... 97

Figure 5.15: Measured bending frequency of a 0.15 mm thick isotropic SGL Sigraflex disc with a diameter of 2 cm as a function of accumulated 4.8 MeV/u U ion fluence. .... 98

Figure 5.16: a) Time dependent velocity signal measured by LDV and b) corresponding FFT spectra at the rear side of a 0.27 mm thick Sigradur G disc with a diameter of 1 cm for the irradiation with 4.8 MeV/u U ions at different fluences. The velocity signals of the pristine sample and irradiated to a fluence of  $4 \times 10^{13}$  ions/cm<sup>2</sup> are not shown for better view. .... 99

Figure 5.17: Measured bending frequency of a 0.27 mm thick Sigradur G disc with a diameter of 1 cm as a function of accumulated 4.8 MeV/u U ion fluence. ....	99
Figure 5.18: Side (left) and top (right) view of the Sigradur G sample after irradiation with 4.8 MeV/u U ions to an accumulated fluence of $4 \times 10^{13}$ ions/cm <sup>2</sup> . Radiation damage leads to fragmentation of the irradiated layer which finally detaches from the underlying non-irradiated substrate.....	100
Figure 5.19: a) Time dependent velocity signal measured by LDV and b) corresponding FFT spectra measured at the rear side of a 0.5 mm thick h-BN disc with a diameter of 2 cm under irradiation with 4.8 MeV/u U ions at different fluences. ....	101
Figure 5.20: Time dependent velocity signal measured by LDV at the rear side of a 0.5 mm thick h-BN disc with a diameter of 2 cm at an accumulated fluence of $1 \times 10^{13}$ ions/cm <sup>2</sup> (red) and ANSYS simulation (black) using h-BN properties....	101
Figure 5.21: Measured frequency of the bending mode assigned to a) the entire sample and b) the detached central part of a 0.5 mm thick h-BN disc with a diameter of 2 cm as a function of accumulated 4.8 MeV/u U ion fluence. The uncertainty of the frequencies given by the limited frequency resolution of the FFT is smaller than the size of the symbols in b). ....	102
Figure 5.22: 0.5 mm thick h-BN disc with a diameter of 2 cm after irradiation with 4.8 MeV/u U ions to an accumulated fluence of $5 \times 10^{13}$ ions/cm <sup>2</sup> . The sample fractured around the beam spot area and is visibly bent. The black horizontal line originates from a carbon paint applied for thermal camera monitoring during irradiation. ....	103
Figure 6.1: Hardness and Young's modulus of pristine (plane coloured bars) and irradiated (plane plus striated coloured bars) graphitic materials. The bars show the properties at the highest investigated Au ion fluences ( <sup>1</sup> $5 \times 10^{13}$ ions/cm <sup>2</sup> , 4.8 MeV/u; <sup>2</sup> $7 \times 10^{13}$ ions/cm <sup>2</sup> , 4.8 MeV/u; <sup>3</sup> $2 \times 10^{14}$ ions/cm <sup>2</sup> , 3.6 MeV/u).....	104

---

## List of tables

---

Table 2.1: Properties of the investigated isotropic polycrystalline graphite grades SGL R6300 and SGL R6650 and POCO ZEE according to the producers' data sheets. .....	6
Table 2.2: Properties of the investigated carbon fibre reinforced carbon grades SGL Premium, SGL Experimental Premium and Tatsuno AC150k according to the producers' data sheets. Due to the two-dimensional structure of the fibre planes, the properties are given for the directions parallel and normal to the fibre planes. .....	7
Table 2.3: Material properties of the glassy carbon grades Sigradur K and G according to the producers' data sheets. ....	8
Table 2.4: Material properties of the HOPG grade ZYB produced by Momentive and NT-MDT and the flexible graphite grade SIGRAFLEX produced by SGL.....	9
Table 2.5: Material properties of tungsten, copper and h-BN .....	10
Table 3.1: Irradiation parameters of the samples designated for post irradiation analysis. ....	19
Table 3.2: Irradiation parameters of samples designated for in situ experiments. All samples are exposed to 4.8 MeV/u U ions with a pulse length of 100 ms.....	20
Table 3.3: List of bands included in the deconvolution of the Raman spectra using a laser of wavelength 473 nm. The Raman shift column show the ranges used for the deconvolution of the graphite samples. For cases of high disorder, where certain bands needed to be fixed the band position is noted in brackets. ....	25
Table 4.1: Hardness and Young's modulus for the matrix and fibres of the CFC grade AC150k .....	59

---

## List of abbreviations

---

B	Berkovich
CC	Cube corner
CFC	Carbon fibre reinforced carbon
CERN	European organization for nuclear research (Conseil européen pour la recherche nucléaire)
CTE	Coefficient of thermal expansion
Exp	SGL Premium Experimental
FAIR	Facility for antiproton and ion research
FEM	Finite element method
FFT	Fast Fourier transform
FG	Flexible graphite
FWHM	Full width half maximum
GC	Glassy carbon
GSI	Gesellschaft für Schwerionenforschung
HL-LHC	High luminosity large hadron collider
HOPG	Highly oriented pyrolytic graphite
ip	in-plane
LDV	Laser Doppler vibrometer
MEVVA	Metal vapour vacuum arc
PG	Polycrystalline graphite
PIG	Penning ionization gauge
Prem	SGL Premium
PTR	Photothermal radiometry

---

SEM	Secondary electron microscope
SRIM	Stopping and range of ions in matter
STM	Scanning tunnelling microscope
tr	transversal
UNILAC	Universal linear accelerator

---

# Acknowledgements

---

The completion of this thesis would not have been possible without the support and assistance of many people. I would like to express my sincere gratitude to all of you:

- my PhD supervisor Prof. Christina Trautmann for providing me the position, her scientific advice and her instant help whenever it was required.
- my supervisor Dr. Marilena Tomut for suggesting me the topic of this project, her scientific advice and support during the experiments.
- Dr. Alexey Prosvetov, Pascal Simon and Philipp Drechsel for the shared beam time shifts and many helpful discussions about irradiation effects in graphite and Ansys simulations.
- Daniel Schmitt, Pascal Knöchel, Stellina Jonot, Michael Walter and Jan-Hendrik Rockstedt who I had the honour to supervise and whose projects advanced this work a lot.
- Dr. Daniel Severin, Dr. Markus Bender, Dr. Ina Schubert, Dr. Frieder Koch and Dr. Bruno Merk for their support during beam times.
- Dr. Kay-Obbe Voss for having solutions for everything.
- Arne Siegmund and Elko Schubert for help during the design and construction of holders and set-ups.
- the other members of the Materials Research group for help whenever needed and the great atmosphere both at work and at other activities.
- the team of the mechanical workshop and the team of the target laboratory for the machining of the samples and the holders.
- the HGS-HIRe graduate school for financial support and their workshops and soft skill courses, providing vital knowledge beyond the topic of this thesis and the connection to students from other research departments.
- the European Union's Horizon 2020 Research and Innovation program under Grant Agreement No 730871 for providing funding for this project.
- my parents Barbara and Reinhold for financial and mental support during all my studies.

- 
- my family, friends and team members who are not all already mentioned for all the help, the distraction and the fond memories in the last years.

Thanks to all of you!